EFFECTS OF CHARGING ON TWO-DIMENSIONAL HONEYCOMB NANOSTRUCTURES

A DISSERTATION SUBMITTED TO
THE DEPARTMENT OF MATERIALS SCIENCE AND
NANOTECHNOLOGY
AND THE GRADUATE SCHOOL OF ENGINEERING AND SCIENCE
OF BILKENT UNIVERSITY
IN PARTIAL FULFILLMENT OF THE REQUIREMENTS
FOR THE DEGREE OF
DOCTOR OF PHILOSOPHY

By
Mehmet Topsakal
July, 2012

I certify that I have read this thesis and that in my opinion it is fully adequate, in scope and in quality, as a dissertation for the degree of doctor of philosophy.

Prof. Dr. Salim Çıracı (Advisor)

I certify that I have read this thesis and that in my opinion it is fully adequate, in scope and in quality, as a dissertation for the degree of doctor of philosophy.

Prof. Dr. Atilla Erçelebi

I certify that I have read this thesis and that in my opinion it is fully adequate, in scope and in quality, as a dissertation for the degree of doctor of philosophy.

Prof. Dr. Macit Özenbaş

I certify that I have read this thesis and that in my opinion it is fully adequate, in scope and in quality, as a dissertation for the degree of doctor of philosophy.

Assoc. Prof. Dr. Mehmet Özgür Oktel

I certify that I have read this thesis and that in my opinion it is fully adequate, in scope and in quality, as a dissertation for the degree of doctor of philosophy.

Assoc. Prof. Dr. Mehmet Bayındır

Approved for the Graduate School of Engineering and Science:

Prof. Dr. Levent Onural
Director of the Graduate School

ABSTRACT

EFFECTS OF CHARGING ON TWO-DIMENSIONAL HONEYCOMB NANOSTRUCTURES

Mehmet Topsakal
Ph.D. in Materials Science and Nanotechnology
Supervisor: Prof. Dr. Salim Çıracı
July, 2012

In this thesis we employ state-of-the-art first-principles calculations based on density functional theory (DFT) to investigate the effects of static charging on two-dimensional (2D) honeycomb nanostructures. Free standing, single-layer graphene and other similar single-layer honeycomb structures such as boron nitride (BN), molybenum disulfide (MoS_2), graphane (CH) and fluorographene (CF) have been recently synthesized with their unusual structural, electronic and magnetic properties. Through understanding of the effects of charging on these nanostructures is essential from our points of view in order to better understand their fundamental physics and developing useful applications.

We show that the bond lengths and hence 2D lattice constants increase as a result of electron removal from the single layer. Consequently, phonons soften and the frequencies of Raman active modes are lowered. Three-layer, wide band gap BN and MoS_2 sheets are metalized while these slabs are wide band semiconductors, and excess positive charge is accumulated mainly at the outermost atomic layers. Excess charges accumulated on the surfaces of slabs induce repulsive force between outermost layers. With increasing positive charging the spacing between these layers increases, which eventually ends up with exfoliation when exceeded the weak van der Waals (vdW) attractions between layers. This result may be exploited to develop a method for intact exfoliation of graphene, BN and MoS_2 multilayers. In addition we also show that the binding energy and local magnetic moments of specific adatoms can be tuned by charging. We have addressed the deficiencies that can occur as an artifact of using plane-wave basis sets in periodic boundary conditions and proposed advantages of using atomic-orbital based methods to overcome these deficiencies. Using the methods and computation elucidated in this thesis, the effects of charging on periodic as well as finite systems and the related properties can now be treated with reasonable

accuracy.

The adsorption of oxygen atoms on graphene have been investigated extensively before dealing with the charging of graphene oxide (GOX). The energetics and the patterns of oxygen coverage trends are shown to be directly related with the amount of bond charge at the bridge sites of graphene structure. We finally showed that the diffusion barriers for an oxygen atom to migrate on graphene surface is significantly modified with charging. While the present results comply with the trends observed in the experimental studies under charging, we believe that there are other factors affecting the reversible oxidation-reduction processes.

Keywords: Graphene, CF, CH, BN, MoS_2, GOX, charging, exfoliation.

ÖZET

ELEKTRİKSEL YÜKLENMENİN İKİ BOYUTLU BAL PETEĞİ ÖRGÜSÜNE SAHİP NANOYAPILAR ÜZERİNE ETKİSİ

Mehmet Topsakal
Malzeme Bilimi ve Nanoteknoloji, Ph.D.
Tez Yöneticisi: Prof. Dr. Salim Çıracı
Temmuz, 2012

Bu tezde ilk prensiplere dayanarak bal peteği örgüsüne sahip iki boyutlu nano yapıların üzerine elektriksel yüklenmenin etkilerini günümüz gelişmiş metodlarını kullanarak inceledik. Grafen, molibden disülfür (MoS_2), bor nitrür (BN), grafan (CH), ve folorografen (CF) yakın zamanda sentezlenebildi ve çok önemli yapısal, elektriksel ve manyetik özelliklere sahiptirler. Bu bağlamda bize göre bu malzemelerin elektriksel yük altında fiziksel özelliklerinin değişiminin incelenmesi ileriki olası uygulamalar ve bu malzemelerin daha iyi anlaşılabilmesi için önem arz etmektedir.

Yapıdan elektron çekilmesiyle bağ uzunluklarının ve dolayısıyla örgü vektörlerinin büyüdüğünü gösterdik. Bu sebepten fononlar yumuşadı ve Raman-aktif fonon modlarının frekansları düştü. Normalde oldukça yüksek yasak enerji aralığına sahip olan BN ve MoS_2 gibi malzemeler iletken haline geldiler. Pozitif yüklenme neticesinde artı yüklerin bu malzemelerin üç katmanlı yapılarında en dış katmanlarında toplandığı görüldü. Daha sonrasında pozitif yüklenme miktarını arttırılmasıyla birbirlerine zayıf van der Waals bağlarıyla bağlanmış olan katmanların ayrıldığı görüldü. Bu neticeler elektriksel yüklenme yardımıyla çok katmanlı grafit, BN ve MoS_2 yapılarından tekli katmanların elde edilebilmesini öngörmektedir. Ek olarak bazı atomların elektriksel yüklenme neticesinde grafen üzerine bağlanma enerjilerinin ve manyetik momentlerinin değiştirilebileceğini gösterdik. Düzlem dalga metodunun sınır koşulları içinde kullanılmasıyla ortaya çıkan yapay yetersizliklerin atomik orbital tabanlı başka yöntemler kullanılarak aşılabileceğini gösterdik.

Oksitlenmiş grafen üzerine elektriksel yükün etkilerini araştırmaya başlamadan önce oksijen atomlarının grafen üzerine bağlanmasını detaylı birşekilde inceledik.

Grafen bağları üzerindeki elektriksel yük miktarının oksijen atomlarının grafen üzerine bağlanmasını kontrol eden en önemli unsur olduğunu ortaya çıkardık. Daha sonrasında ise oksijen atomlarının grafen üzerindeki difüzyon bariyerlerinin elektriksel yüklenme ile belirgin şekilde değiştiğini gösterdik. Elde ettiğimiz bu sonuçlar deneysel verilerdeki pozitif yüklenmenin grafenin oksitlenmesine yol açtığını negatif yüklenmenin ise oksitlenmiş grafenin normal grafene dönüşmesine yol açtığı şeklindeki sonuçlarını kısmen desteklemektedir ve başka etkenlerin de bu oluşumlarda rol oynayabileceğini öngörmektedir.

Anahtar sözcükler: Grafen, CF, CH, BN, MoS_2, GOX, yüklenme, ayrılma.

Acknowledgement

I would like to thank my supervisor Prof. Salim Ciraci for giving me the opportunity to work under his supervision with his great inspirations and motivations. I am grateful for the external examinees Prof. Mehmet Bayındır, Prof. Atilla Erçelebi, Prof. Mehmet Özgür Oktel and Prof. Dr. Macit Özenbaş for taking time to review this thesis. I would like to thank my collaborators and friends: Prof. Aykutlu Dana, Dr. Seymur Cahangirov, Dr. Hasan Şahin, Dr. Can Ataca, Dr. Ethem Aktürk, Dr. Hakan Gürel, Dr. Engin Durgun, Dr. Haldun Sevinçli Veli Ongun Ozcelik and all my friends in UNAM who have made my graduate life delightful. Last, but not least, I thank to my family.

Contents

List of Figures

List of Tables

Chapter 1

Introduction

The advancement of science strongly depends on the interplay between theoretical and experimental studies. In some cases, theoretical physics sticks to mathematical rigors while giving little importance to observations and experiments. On the other hand, experimental physics sometimes cannot go beyond reporting laboratory results lacking the theoretical explanation. When theory meets experiment, remarkable scientific achievements are made possible. A well-known example is photoelectric effect, previously an experimental result lacking a theoretical formulation but then explained by Einstein who was awarded by Nobel Prize.

Computational physics is the study and implementation of numerical methods to solve physical problems for which a quantitative theory already exists. It is often regarded as a subdiscipline of theoretical physics but some consider it as an intermediate discipline between theoretical and experimental physics. Computational simulation is an integral part of modern science and the ability to exploit effectively the power offered by computers is therefore essential for scientists. It has taken its place as a method for doing science and has bridged the theory to experiment. Computational and theoretical chemistry may provide fundamental insights into the structural properties, reactivities and dynamics of molecules and solids. As a result, theoretical calculations have become essential in various fields of chemical research and development.

The motivation of this thesis is stimulated by experimental work done by Ekiz and his co-workers[1] from Prof. Dana's research group in our home institution claiming that the electrical charge has strong effects on the thermodynamics equilibrium of graphene/graphene-oxide system. They show that in ambient atmosphere, the positive charge causes oxidation of graphene, and negative charge enhances the reduction of graphene oxide to graphene. Their results suggest that the electrical bias and charging effects are important in energetic analysis and allow designing of novel graphene-based nanostructures. We present our research in the area of computational physics based on state-of-the-art quantum mechanical simulations in order to better understand these experimental findings.

Recent advances in materials growth and control techniques have made the synthesis of the isolated, two-dimensional (2D) honeycomb crystal of graphene possible [2, 3, 4, 5] in 2004 which was believed to be unstable for a long time[6]. Owing to its unusual electronic energy band structure leading to the charge carriers resembling massless Dirac Fermions, graphene introduced new concepts and initiated active research [7, 8]. To the best of our knowledge, the effects of static charging on graphene structure haven't been studied previously and we first start with investigation of the effects of charging on bare graphene structure. Since the graphene structure is recently discovered, through understanding of the effects of charging on graphene is essential from our points of view in order to better understand its fundamental physics and developing useful applications. Boron nitride (BN) analogue of graphene were also realized experimentally having desired insulating characteristics[9]. Subsequently other graphene like 2D nanostructures have been realized experimentally. Graphane (CH) is hydrogenated form of 2D graphene where each carbon atom bonds with a hydrogen atom[10] and fluorographene (CF) is fluorinated analogue of graphane[11]. Molybenum disulfide, MoS_2[12], is another two-dimensional honeycomb structure but not containing any first and second row elements of periodic table. We call these graphene-like structures as *"graphene's cousins"* and investigate the effects of charging on them in addition to graphene. The exfoliation of 3-layered graphene, BN and MoS_2 upon positive charging have also been investigated.

Before dealing with the effects of charging on the oxidation of graphene, we

performed an extensive analysis of the oxygen adatom adsorption for neutral case. Despite the oxidized graphite is a known material since 150 years and great deal of experimental and theoretical research carried out recently, a precise knowledge regarding the interaction of oxygen with graphene and resulting processes are not available yet. From our point of view, there exists still a controversies between theory and experiment. For example, the distribution of hydroxy and epoxy groups on GOX surface is still unclear; their clustering or uniform coverage trends are unknown. At least, a rigorous explanation for the reason of the differences in the interpretations of experimental data is required.

We finally investigate the effects of charging on the oxidation properties of graphene. The variation of oxidation dynamics with positive and negative charging is studied. Although there are several studies involving charged surface calculations available in literature, the deficiencies of using plane-wave calculations in the treatment of negatively charged layers are not emphasized in those works. We clarified those deficiencies and presented alternative ways of dealing with charged calculations in addition to plane-wave calculations. We carried out binding energy and oxygen-oxygen interaction calculations in order to understand the releasing of oxygen atoms from graphene upon negative charging as claimed by experimental study.

The organization of thesis is as follows: Chapter 2 briefly describes the theoretical background and approximations of the computational methods. Chapter 3 is related with the effects of charging on graphene and graphene-like nanostructures not including graphene-oxide. Chapter 4 is related with the oxidation of graphene while in Chapter 5 we present our results for the effects of charging on the oxidation properties of graphene. Chapter 5 is conclusions summarizing the results of our studies.

Chapter 2

Methodological background

In this chapter we will briefly discuss the theoretical framework, computational methodologies and approximations of density functional theory (DFT) which have been used in this thesis. It is not intended to give complete introduction to DFT calculations but rather to cover some of basic definitions, which are relevant to interpretation of the simulation results. For more detailed and extensive information the interested reader referred to Payne *et al.* [13] and references therein.

2.1 Schrödinger Equation and Density Functional Theory (DFT)

The Schrödinger equation (SE) is an equation that describes how the quantum state of a physical system changes with time. It was formulated in late 1925, and published in 1926, by the Austrian physicist Erwin Schrödinger. The wave function is the solution to the wave equation which is known as the Schrödinger equation:

$$\left[\frac{\hbar^2}{2m}\nabla^2(\mathbf{r}) + V(\mathbf{r})\right]\psi(\mathbf{r},t) = i\hbar\frac{\partial\psi(\mathbf{r},t)}{\partial t} \tag{2.1}$$

Where m is the particle's mass, V is its potential energy, ∇^2 is tha Laplacian and ψ is position-space wavefunction. In the standard interpretation of quantum mechanics, the wave function is the most complete description that can be given to a physical system. While SE is believed to hold true for any system, solution of this equation is not feasible in many cases and approximations are used.

The time-independent Schrdinger equation is the equation describing stationary states and it is easier to solve. By dropping the time dependency, SE gets an eigenvalue equation:

$$\hat{H}\Psi_i(\mathbf{r},\mathbf{R}) = E_i\Psi_i(\mathbf{r},\mathbf{R}) \tag{2.2}$$

$\hat{H}$ is the Hamiltonian operator and E_i is the energy eigenvalue corresponding to many body time-independent wave function, $\Psi_i(\mathbf{r},\mathbf{R})$. With the aid of Born-Oppenheimer approximation, in which the electrons are assumed to move faster than the nuclei as a result of significant mass difference between electron and proton ($\sim$1800 times), the nuclei can be treated as stationary. With these conditions, the wave function can be factorized as $\Psi_{total} = \psi_{electronic} \times \psi_{nuclear}$. Assuming these approximations, we are left with the problem of solving the many-body electronic Schrödinger equation for fixed nuclear positions. The resulting Hamiltonian operator for Eqn. 2.2 can be written as:

$$\hat{H} = \hat{T}_e + \hat{V}_{n-e} + \hat{V}_{e-e} + \hat{V}_{n-n} \tag{2.3}$$

The first term is the kinetic energy operator for electrons,

$$\hat{T}_e = -\sum_{i=1}^{N} \frac{\hbar^2}{2m}\nabla_i^2 \tag{2.4}$$

The second term is the energy operator for ion-electron interactions,

$$\hat{V}_{n-e} = -e^2 \sum_{I=1}^{P}\sum_{i=1}^{N} \frac{Z_I}{|\mathbf{R}_I - \mathbf{r}_i|} \tag{2.5}$$

in which the charge of I^{th} ion is represented by Z_I and $\mathbf{r}_i$ and $\mathbf{R}_I$ are the positions of the i^{th} electron and I^{th} nuclei ion. The third term is a potential energy operator for the electron-electron interactions:

$$\hat{V}_{e-e} = \frac{e^2}{2} \sum_{i=1}^{N} \sum_{j \neq i}^{N} \frac{1}{|r_i - r_j|} \tag{2.6}$$

The last term corresponds to ion-ion interactions which can be dropped in solving the electronic wave function since it is simply an additive term.

$$\hat{V}_{n-n} = \frac{e^2}{2} \sum_{I=1}^{P} \sum_{J \neq I}^{P} \frac{Z_I Z_J}{|\mathbf{R}_I - \mathbf{R}_J|} \tag{2.7}$$

where $\mathbf{R} = \{\mathbf{R}_I\}$, $I = 1, ..., P$, is a set of P nuclear coordinates and $\mathbf{r} = \{\mathbf{r}_I\}$, $i = 1, ...,$ N, is a set of N electronic coordinates. The total energy of the system, E_{total} , can be obtained by solving the Eqn. 2.2 for the electronic ground state energy, E_i, and the ground state many-body wave function $\Psi_i(\mathbf{r},\mathbf{R})$ and adding the ion-ion interaction energy term: $E_{total} = E + V_{n-n}$. Even in time-independent regime, SE is still very hard to solve and for this reason the effort is directed towards finding more efficient approaches and approximations. Density functional theory (DFT), which has been very popular for calculations in condensed matter physics, is developed for this aim.

DFT has its roots in the Thomas-Fermi (T-F) Approximation [14, 15] which model the electron density as the central variable rather than the wave function. Later a firm theoretical footing by the Hohenberg-Kohn theorems in 1964 [16, 17] was done. The first of these demonstrates the existence of a one-to-one mapping between the ground state electron density and the ground state wave function of a many-particle system. Further, the second Hohenberg-Kohn theorem proves that the ground state density minimizes the total electronic energy of the system. DFT is an alternative approach to the theory of electronic structure, in which the electron density distribution $\rho(\mathbf{r})$ rather than many-electron wave function plays a central role. In the spirit of Thomas-Fermi theory, it is suggested that a knowledge of the ground state density of $\rho(\mathbf{r})$ for any electronic system uniquely

determines the system.

The Hohenberg-Kohn [16] formulation of DFT can be explained by two theorems:

Theorem 1: For any system of interacting particles in an external potential $V_{ext}(\vec{r})$, the density is uniquely determined except for a trivial additive constant (in other words, the external potential is unique functional of charge density).

Since $\rho(\mathbf{r})$ determines V($\mathbf{r}$), then it also determines the ground state wave function and gives us the full Hamiltonian for the electronic system.

Theorem 2: A universal functional for the energy E can be dened in terms of the density. The exact ground state is the global minimum value of this functional.

In 1965, W. Kohn and L. Sham [17] proposed the idea of replacing the kinetic energy of the interacting electrons with that of an equivalent non-interacting system. With this assumption density can be written as:

$$\rho(\mathbf{r}) = \sum_{s=1}^{2} \sum_{i=1}^{N_s} |\varphi_{i,s}(\mathbf{r})|^2 \tag{2.8}$$

With the kinetic energy term:

$$T[\rho] = \sum_{s=1}^{2} \sum_{i=1}^{N_s} \langle \varphi_{i,s}| - \frac{\nabla^2}{2} |\varphi_{i,s}\rangle \tag{2.9}$$

The single-particle orbitals $\varphi_{i,s}$'s are the N_S lowest order eigenfunctions of Hamiltonian that is

$$\{-\frac{\nabla^2}{2} + v(\mathbf{r})\}\varphi_{i,s}(\mathbf{r}) = \epsilon_{i,s}\varphi_{i,s}(\mathbf{r}) \tag{2.10}$$

Using new form of $T[\rho]$, the universal density functional can be written in the following form:

$$F[\rho] = T[\rho] + \frac{1}{2}\int\int \frac{\rho(\mathbf{r})\rho(\mathbf{r}')}{|\mathbf{r}-\mathbf{r}'|} d\mathbf{r}d\mathbf{r}' + E_{XC}[\rho] \tag{2.11}$$

where this equation defines the exchange and correlation energy as a functional of the density. Using this functional in the total energy functional, $\mathrm{E}[\rho] = \mathrm{F}[\rho] + \int \rho(\mathbf{r})v(\mathbf{r})d\mathbf{r}$ we finally obtain the total energy functional which is known as Kohn-Sham functional: [17]

$$E_{KS}[\rho] = T[\rho] + \int \rho(\mathbf{r})v(\mathbf{r})d\mathbf{r} + \frac{1}{2}\int\int \frac{\rho(\mathbf{r})\rho(\mathbf{r}')}{|\mathbf{r}-\mathbf{r}'|} d\mathbf{r}d\mathbf{r}' + E_{XC}[\rho] \tag{2.12}$$

In this way the density functional is expressed in terms of the KS orbitals, which minimize the kinetic energy under the fixed density constraint. In principle, these orbitals are a mathematical object constructed in order to render the problem more tractable and do not have any sense by themselves, but only in terms of the electronic density. The solution of KS equations can be obtained by an iterative way, in the same way of Hartree and Hartree-Fock equations. In practice, however, it is customary to consider KS orbitals as single-particle physical eigenstates.

In summary, we briefly described the theory that is able to solve the complicated many-body problem by mapping exactly the many-body Schroedinger equation into a set of coupled single-particle equations. Given an external potential, the energy and any desired ground state properties (e.g., stress, phonons, etc.) can be obtained. The density of the non-interacting reference system is equal to that of the true interacting system. Up to now the theory is exact since have not introduced any approximation into the electronic problem. All the ignorance about the many-body problem has been displaced to the E_{XC} $[\rho]$ term, while the remaining terms in the energy are known.

In the next sections we discuss the approximations employed for solving KS equations.

2.2 Exchange-Correlation Functionals

The main approximation enters in the choice of an exchange-correlation functional, E_{XC} $[\rho]$, since no exact form is known for this functional. The oldest, the simplest and widely used is the local density approximation (LDA) suggested by Kohn and Sham. In the LDA approximation the exchange-correlation energy of an electronic system is constructed by assuming that the exchange-correlation energy per electron at a point $\mathbf{r}$ in the electron gas, $\varepsilon_{XC}(\mathbf{r})$, is equal to the exchange-correlation energy per atom in a homogeneous electron gas that the same density as the electron gas at point $\mathbf{r}$. Thus

$$E_{XC}^{LDA}[\rho] = \int \rho(\mathbf{r})\varepsilon_{XC}^{LDA}[\rho]d\mathbf{r} \tag{2.13}$$

The local-density approximation assumes that the exchange-correlation energy is purely local and ignores correlations to the exchange-correlation energy at a point $\mathbf{r}$ due to nearby inhomogeneities in the electron density. Considering the inexact nature of approximation, the calculations performed with LDA is quite successful especially for metals and semiconductors.

As a next step, some of the non-locality can be included by making the ε_{XC} depend also on the gradient(s) of the electron density. Several studies, but especially by Perdew [18], have worked on next step to the LDA with inclusion of effects proportional to the gradient of the charge density. The improvements along these ways are called Generalized Gradient Approximation (GGA). In some systems GGA give better results but worse in others, Generally, the GGA seems to be an improvement over the conventional LDA. The exchange-correlation energy in GGA can be expressed in the following form:

$$E_{XC}[\rho] = \int \rho(\mathbf{r})\epsilon_{XC}[\rho(\mathbf{r})]d\mathbf{r} + \int F_{XC}[\rho(\mathbf{r}, \nabla\rho(\mathbf{r}))]d\mathbf{r} \tag{2.14}$$

where the function F_{XC} is asked to satisfy the formal conditions for the exchange-correlation hole.

2.3 Periodic boundary conditions and plane-wave basis sets

There are some difficulties arising from mapping of observables of the many-body problem into equivalent observables in an effective single-particle problem. One of them is the wave function which must be calculated for each of infinite number of electrons in the the system. The other one is that the basis set required to expand each wave function is infinite since the wave function extends over the entire solid. Both problems can be solved by performing calculations on periodic systems and applying Bloch's theorem to the wave functions.

Bloch theorem states that in a periodic solid each electronic wave function can be written as the product of a periodic function and a plane wave envelope function:

$$\Psi_i(\mathbf{r}) = u_i(\mathbf{r})e^{i\mathbf{kr}} \tag{2.15}$$

where u_k has the period of crystal lattice with $u_k(\mathbf{r}) = u_k(\mathbf{r}+\mathbf{T})$. This part can be expanded using a basis set consisting of reciprocal lattice vectors of the crystal.

$$u_i(\mathbf{r}) = \sum_G a_{k,G} e^{i(\mathbf{G})\mathbf{r}} \tag{2.16}$$

Therefore each electronic wave function can be written as a sum of plane waves

$$\Psi_i(\mathbf{r}) = \sum_G a_{i,k+G} e^{i(\mathbf{k}+\mathbf{G})\mathbf{r}} \tag{2.17}$$

In principle, an infinite number of plane-waves are required to expand the wave function at each **k**-point in above sum. However, only the small kinetic energy terms are important. For this reason, an energy cut-off (E_{cutoff}) can be imposed on plane waves such that $|\mathbf{k} + \mathbf{G}|^2 < E_{cutoff}$. Furthermore, increase or decrease of E_{cutoff} allow the control of accuracy in plane-wave calculations.

2.4 Pseudopotential approximation

Although Bloch's theorem states that every electronic wave function can be expressed using a discrete set of plane waves, it is sometimes very poorly suited to expand wave functions because a very large number of plane waves are needed to expand the tightly bounded core electrons. An extremely large plane-wave basis set may be required to perform all-electron calculation leading to a vast amount of computational time to calculate electronic wave functions. Pseudopotential approximation allows the expansion of electronic wave functions using a much smaller plane-waves.

It is well known that most of the physical properties of solids mainly depends on valance electrons rather than the core electrons. The pseudopotential approximation exploits this by removing core electrons and replacing them and strong ionic potential by a weaker pseudopotential that acts on a set of pseudo wave functions rather than the actual valance wave functions.

Chapter 3

Charging of 2D honeycomb structures

We investigate the effects of static charging on structural, electronic and magnetic properties of suspended, single layer graphene, graphane, fluorographene, BN and MoS_2. All these honeycomb nanostructures have two dimensional (2D) hexagonal lattice. We demonstrate that the properties of these nanostructures can be modified either by direct electron injection into it or electron removal from it; namely by charging the system externally. The limitations of periodic boundary conditions in the treatment of negatively charged layers are clarified. Upon positive charging the band gaps between the conduction and valence bands increase, but the single layer nanostructures become metallic owing to the Fermi level dipping below the maximum of valence band. Moreover, their bond lengths increase leading to phonon softening. As a result, the frequencies of Raman active modes are lowered. High level of positive charging leads to structural instabilities in single layer nanostructures, since their specific phonon modes attain imaginary frequencies. Similarly, excess positive charge is accumulated at the outermost layers of metallized BN and MoS_2 sheets comprising a few layers. Once the charging exceeds a threshold value the outermost layers are exfoliated. This result may be exploited to develop a method for intact exfoliation of graphene and these graphene-like structures. Charge relocation and repulsive force generation are in

compliance with classical theories. In addition to exfoliation, the energy level structure, density of states, binding energies and desorption of specific adatoms can be monitored by charging. We found that pseudopotential plane-wave calculations of charged surfaces using periodically repeating layers are sensitive to the vacuum spacing between adjacent cells and have limited applicability. On the other hand, using atomic-orbital based methods was shown to have some advantages.

In the following sections we briefly describe some of structural and electronic properties of graphene, BN, MoS_2, CH and CF. Then we present our results on the effects of charging of these structures.

3.0.1 Graphene and its structure

Synthesis of a single atomic plane of graphite, i.e. *graphene*, with covalently bonded honeycomb lattice has been a breakthrough for several reasons[2, 3, 4, 5, 19]. Firstly, electrons behaving as if massless Dirac fermions have made the observation of several relativistic effects possible. Secondly, stable graphene has disproved previous theories, which were concluded that two-dimensional structures cannot be stable. Graphene with its unique mechanical, structural, electronic and thermal properties has been identified as a promising candidate for novel applications in various fields[8], Not only 2D graphene, but also its quasi 1D forms, such as armchair and zigzag nanoribbons have shown novel electronic and magnetic properties[20, 21, 22], which can lead to important applications in nanotechnology. Up to now, many of its unusual properties are well investigated and clever methods of graphene production are proposed[23, 24, 25, 26, 27], Further studies are directed towards the controlling of graphene's electronic and magnetic properties in order to open the new ways of better understanding of its fundamental physics and developing useful applications.

The hexagoanal lattice structure and reciprocal lattice of graphene are shown in Fig. 3.1. The lattice vectors can be written as:

$$\vec{a}_1 = \frac{a}{2}(\sqrt{3}, 3, 0) \qquad \vec{a}_2 = \frac{a}{2}(-\sqrt{3}, 3, 0) \tag{3.1}$$

where a $\approx$ 1.42 Å is the nearest carbon-carbon distance. The reciprocal lattice vectors are given by:

$$\vec{b}_1 = \frac{2\pi}{3a}(\sqrt{3}, 1, 0) \qquad \vec{b}_2 = \frac{2\pi}{3a}(-\sqrt{3}, 1, 0) \tag{3.2}$$

The two points at the corners of graphene's Brillouin zone (BZ) is of special importance. Their positions are given by:

$$K = \left(\frac{2\pi}{3\sqrt{3}a}, \frac{2\pi}{3a}, 0\right) \qquad K' = \left(-\frac{2\pi}{3\sqrt{3}a}, \frac{2\pi}{3a}, 0\right) \tag{3.3}$$

These special points are called Dirac points and are of particular importance for the electronic properties. Graphene is a semimetal having conduction and valance bands crossing linearly at K-point at the Fermi level (E_F) as shown in Fig. 3.1 (c). The resulting electron-hole symmetry reveals itself in an ambipolar electric field effect, whereby under bias voltage the charge carriers can be tuned continuously between electrons and holes in significant concentrations. Due to its planar 2D structure and reactant p_z orbitals, graphene is naturally responsive for the addition of adsorbates. Graphene oxide (GOX) is a pronounced example[28]. Excess electrons and holes can be also achieved through doping with foreign atoms[29, 30, 31]. For example, adsorbed alkali atoms tend to donate their valence electrons to π^*-bands of graphene. The excess electrons results in the metalization of graphene[32]. Hole doping is achieved by the adsorption of bismuth or antimony[33]. However, the system remains electrically neutral through either way of doping. Recently, carrier concentration and spatial distribution of charge are also changed for very short time intervals by photoexcitation of electrons from the filled states leading to the photoexfoliation of graphite[34, 35, 36].

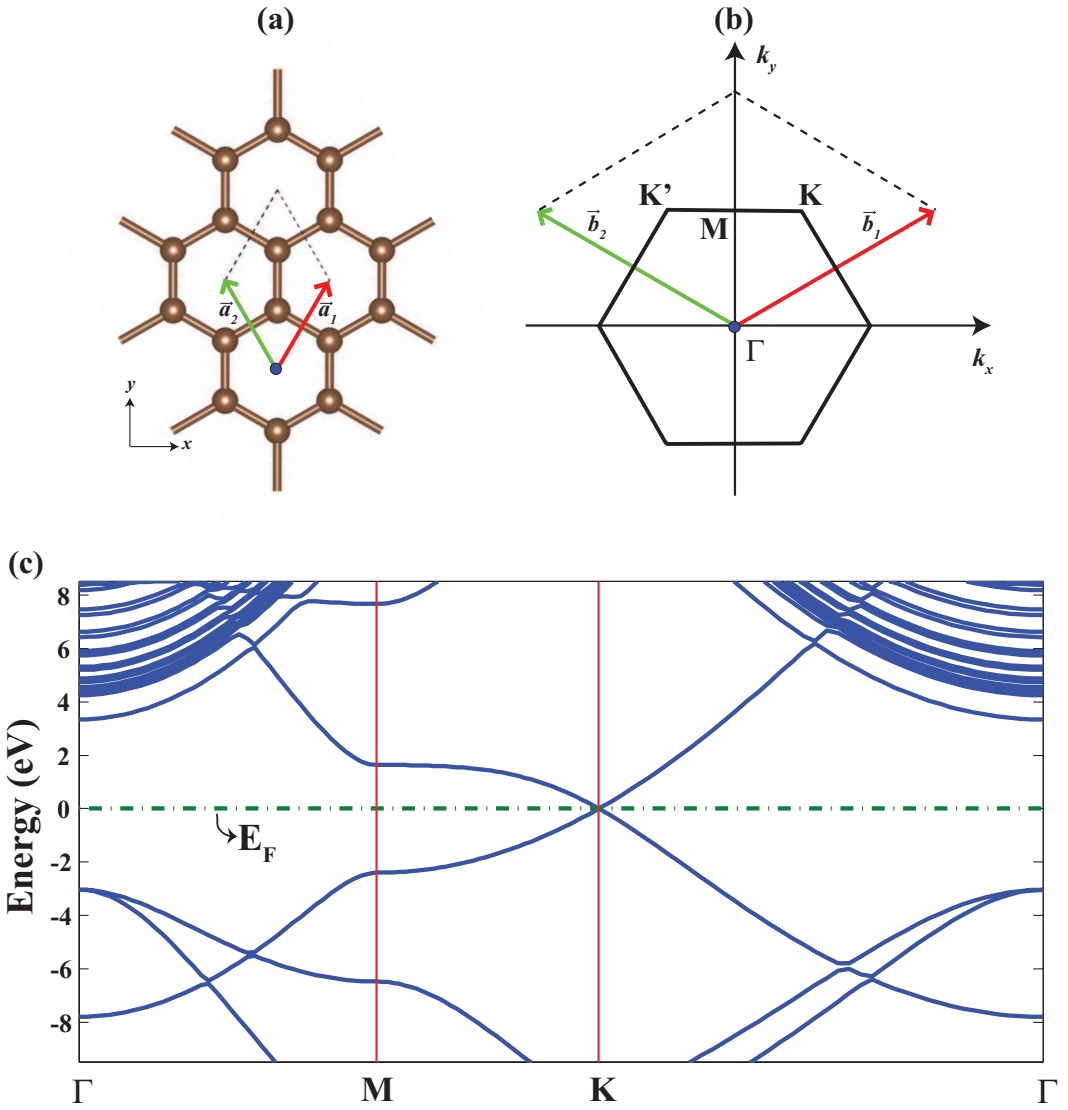

Figure 3.1: (a) Primitive unit cell of the honeycomb structure of graphene. (b) reciprocal lattice vectors and corresponding Brillouin zone (BZ) having special k-points Γ, M and K. (c) Calculated electronic band structure of graphene.

3.0.2 Graphene's cousins : BN, MoS_2, CH and CF

Boron nitride (BN) in ionic honeycomb lattice which is the Group III-V analogue of graphene have also been produced having desired insulator characteristics[9]. Nanosheets[37, 38], nanocones[39], nanotubes[40], nanohorns[41], nanorods[42] and nanowires[43] of BN have already been synthesized and these systems might hold promise for novel technological applications. Among all these different structures, BN nanoribbons, where the charge carriers are confined in two dimension and free to move in third direction, are particularly important due to their well defined geometry and possible ease of manipulation.

BN nanoribbons posses different electronic and magnetic properties depending on their size and edge termination. Recently, the variation of band gaps of BN nanoribbons with their widths and Stark effect due to applied electric field have been studied[44, 45]. The magnetic properties of zigzag BN nanoribbons have been investigated[46]. Half-metallic properties have been revealed from these studies which might be important for spintronic applications.

The atomic structure, atomic charge, charge transfer from B to N and the electronic structure of 2D BN are presented in Fig. 3.2. Contour plots of total charge indicates high density around N atoms. The difference charge density is calculated by subtracting charge densities of free B and N atoms from the charge density of 2D BN, i.e. $\Delta\rho = \rho_{BN} - \rho_B - \rho_N$. High density contour plots around N atoms protruding towards the B-N bonds indicate charge transfer from B to N atoms. This way the B-N bonds achieve an ionic character[47]. The amount of transfer of charge is calculated by Löwdin analysis to be ΔQ=0.429 electrons.

2D BN is a semiconductor[47]. Calculated electronic energy bands are similar to those calculated for h-BN crystal. The π- and π^*- bands of graphene which cross at the K- and K$'$-points of the BZ open a gap in 2D BN as a bonding and antibonding combination of N-p_z and B-p_z orbitals. The contribution of N-p_z is pronounced for the filled band at the edge of valence band. The calculated band gap is indirect and E_{gap} =4.64 eV[47].

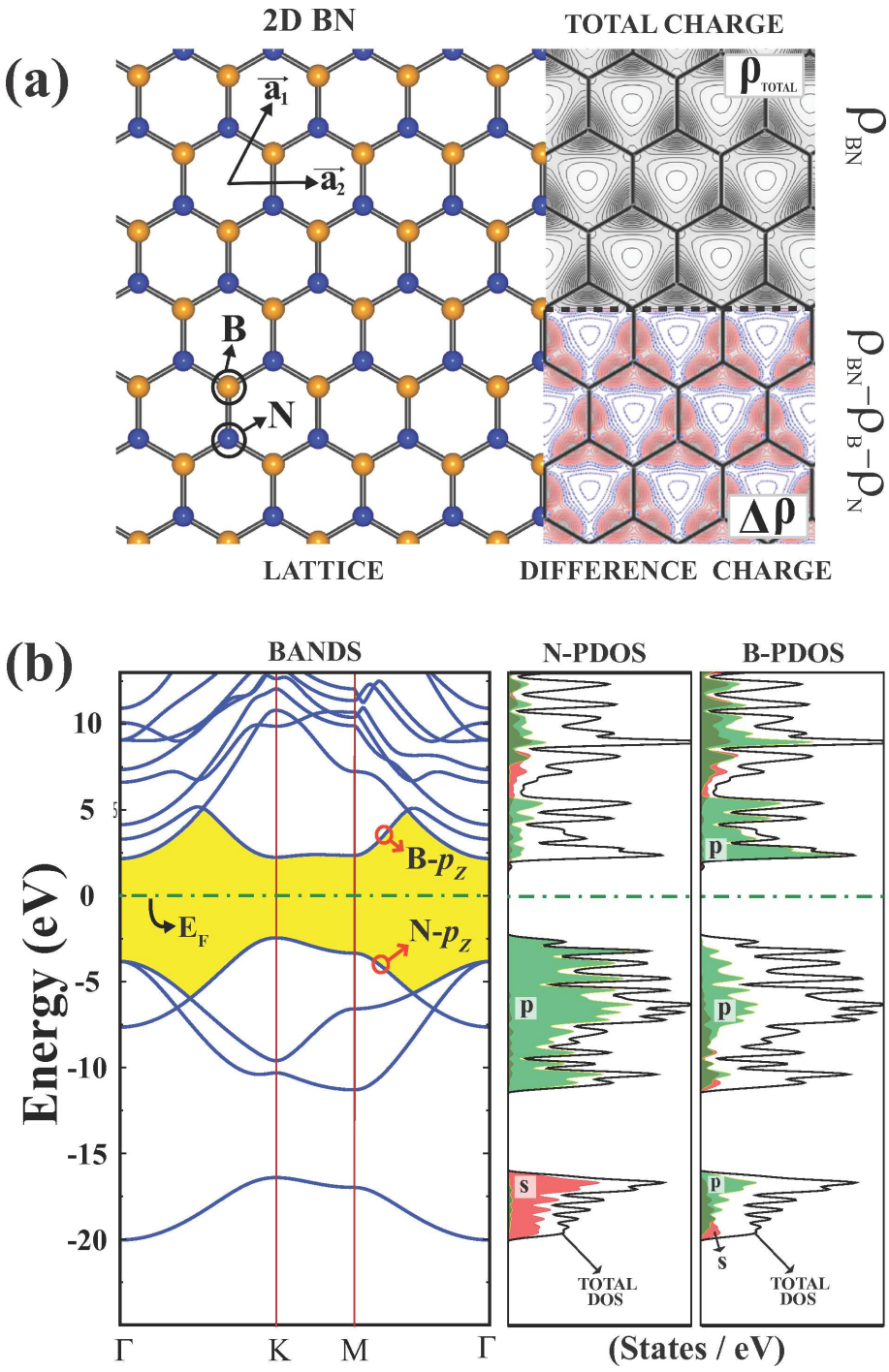

Figure 3.2: (a) Primitive unit cell of the honeycomb structure of 2D BN together with Bravais lattice vectors. Calculated total charge density ρ_{BN} and difference charge density $\Delta\rho$, are also shown in the same panel. (b) Calculated electronic structure of 2D BN honeycomb crystal together with total, TDOS and partial density of states, PDOS on B and N atoms. The orbital character of the states are also indicated.

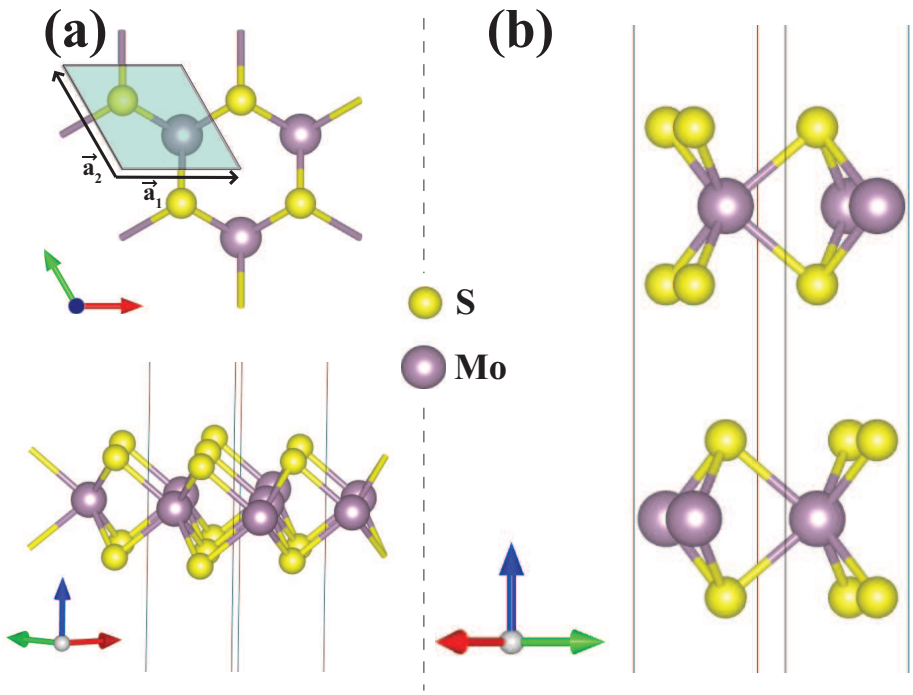

Figure 3.3: (a) Atomic structure of 1H-MoS_2 in hexagonal lattice from top and side view. The unit cell is shaded and lattice constants are indicated. (b) Atomic structure for three dimensional bulk MoS_2. Purple (large) and yellow (small) balls denotes Molybenum and Sulfur atoms.

Molybenum disulfide, MoS_2, is made up of hexagons with Mo and S_2 atoms situated at alternating corners. Each S atom has three nearest Mo atom, and each Mo atoms has six nearest S atoms. For the case of three dimensional bulk MoS_2 (specified as 1H-MoS_2), the layers in the unit cell are displaced relative to each other , so that Mo atoms of one layer are situated on top of S atoms in the two adjacent layers. In this respect, the arrangements of layers are different from that of graphite, where three carbon atoms of one layer are located above the hollow sites (center of the hexagon) of the adjacent layers. The atomic configurations and relevant structural parameters of two-layer MoS_2 are illustrated in Fig. 3.3 Recently, two-dimensional suspended single-layer MoS_2 sheets have been produced[9, 48]. Single-layer MoS_2 nanocrystals having ~ 30 Å width were also synthesized on Au(111) surface[49].

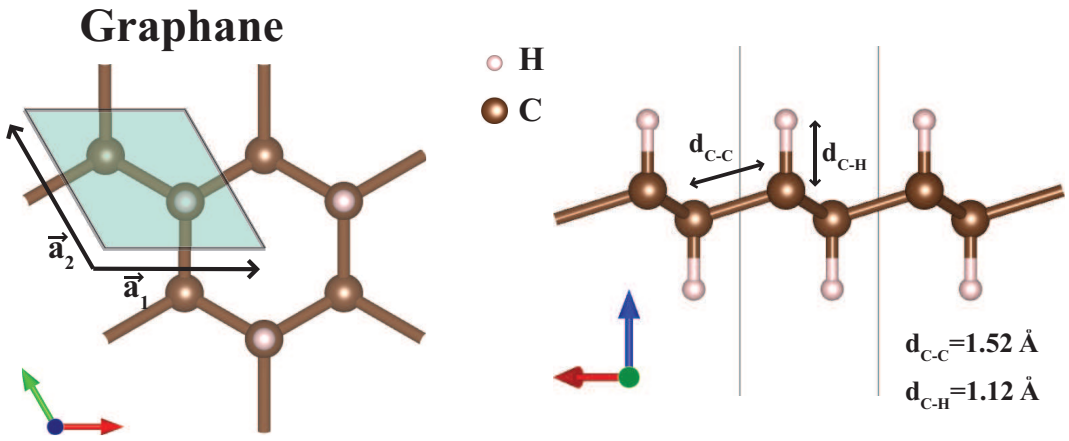

Figure 3.4: Schematic representation of the atomic structure of graphane. The unit cell is shaded and lattice constants are indicated.

The in-plane lattice constant, $|\vec{a}_1| = |\vec{a}_2|$, is 3.22 Å both for 1H- and 2H-MoS_2 calculated with GGA method including vdW interactions[50]. The other lattice constant, $|c|$, is 12.411 Å for 2H-MoS_2 but increases to 15.540 with the inclusion of vdW interactions[50]. The electronic structure of hexagonal MoS_2 is semiconductor. 3D bulk MoS_2 has a indirect band gap of 0.85 eV while 1H-MoS_2 has a direct band gap of 1.58 eV calculated by GGA method.[51] Furthermore, these band gap values increases to 2.50 and 1.44 eV with GW_0 calculations[51]. We recently revealed that weak vdW interaction between layers is critical to hold the layers together and to calculate the interlayer spacing within 0.8% of the experimental value[50]. Therefore, the inclusion of the vdW interaction between the layers of MoS_2 is found to be essential for ab initio calculations of energetics and optimized structures, cohesion, and phonon dispersions.

Graphane (CH), is another member of honeycomb structures was theoretically predicted[52] and recently synthesized by exposing graphene to hydrogen plasma discharge[10]. Here each carbon atom being bonded to one hydrogen atom is pulled out from the graphene plane and hence whole structure is buckled. Instead of being a semimetal like graphene, graphane is a wide band gap semiconductor. Upon hydrogenation of graphene, the lattice constant increases to 2.54 Å and d increases to 1.54 Å[10]. Moreover, C-H bonds are 1.11 Å and the amount

of buckling between the alternating carbon atoms in a hexagon is 0.46 Å[53]. Atomic configuration of graphane structures is shown in Fig. 3.4. The calculated band gap by GGA method is 3.54 eV for graphane[53]. However, the band gap increases to 5.66 eV after G_0W_0 corrections[53].

We showed that the in-plane stiffness value and Poisson ratio of graphane are 243 J/m^2 and 0.07 respectively[53]. Compared to graphene and other 2D materials, these values indicate that it has a quite high in-plane stiffness and very low, perhaps the lowest Poisson's ratio among known monolayer honeycomb structures. We also showed that the band gap of graphane can be modified significantly by applied strain in the elastic range. It is suggested that elastic deformation can be used for further functionalization of graphane and hence for monitoring its chemical and electronic properties[53].

Much recently, Nair and his co-workers[11] synthesized fluorinated graphene (CF) and reported the measured Raman spectrum, band gap, Young's modulus and breaking strength. Each carbon atom of graphene can bind only one F atom, and through coverage (or decoration) of one or two sides of graphene, one can achieve diverse structures. Fluorographene (CF), where F atoms are bound to each C atom of graphene alternatingly from top and bottom sides, is energetically the most favorable structure. Upon full uorination, the planar honeycomb structure of C atoms becomes buckled (puckered) and the C-C bond length increases by $\sim 10\%$. At the end, while planar sp^2 bonding of graphene is dehybridized, the buckled conguration is maintained by sp_3 -like rehybridization. Our calculated lattice constant for CF is 2.55 Å and the in-plane stiffness is 250 (J/m^2)[87]. Atomic configuration of CF is shown in Fig. 3.5.

Similar to CH, fully fluorinated graphene, CF, is a wide band gap insulator. While LDA calculations yield a band gap of 2.96 eV GW_0 calculations increase the band gap as high as 7.49 eV[54].

Single layer graphene, graphane CH, fluorographene CF, BN and MoS_2 have displayed unusual chemical and physical properties for future nanotechnology applications. Furthermore, the properties of these nanomaterials can be modified by creating excess electrical charge. Linear crossing of bands of graphene at the

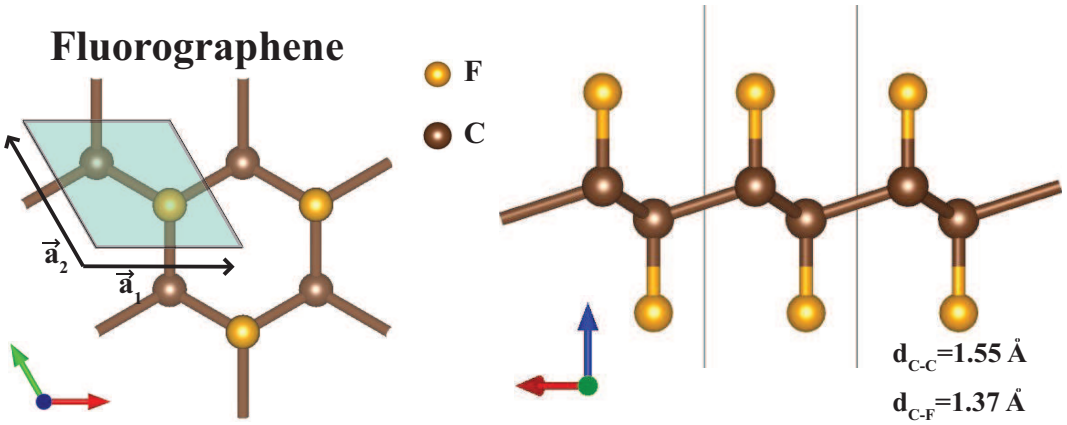

Figure 3.5: Schematic representation of the atomic structure of fluorographene. The unit cell is shaded and lattice constants are indicated.

Fermi level gives rise to electron-hole symmetry, whereby under bias voltage the charge carriers can be tuned continuously between electrons and holes in significant concentrations. This way, the conductivity of graphene can be monitored. Similar situation leading to excess electrons or holes can also be achieved through doping with foreign atoms. Layered materials can be exfoliated under excessive charging, which is created by photoexcitation for very short time. It is proposed that the femtosecond laser pulses rapidly generate hot electron gas, which spills out leaving behind a positively charged graphite slab. Eventually, charged outermost layers of graphite are exfoliated.

3.1 Computational Methodology

Three different first-principles simulation packages; VASP[55, 56], SIESTA[57, 58] and DFTB+[59, 60] are used in this thesis study.

VASP calculations are carried out within spin-polarized and spin-unpolarized density functional theory (DFT) using projector-augmented wave potentials[61]. For the calculations in Sec. 3.2 and 3.7 the exchange correlation potential

is approximated by local-density approximation (LDA). For the rest of calculations the generalized gradient approximation (GGA) is used[62]. We also performed GGA+vdW (generalized gradient approximation including van der Waals corrections[63]) for a better account of van der Waals (vdW) interlayer interactions between graphene, BN and MoS_2 slabs. A plane-wave basis set with kinetic energy cutoff of 500 eV is used. All atomic positions and lattice constants are optimized by using the conjugate gradient method, where the total energy and atomic forces are minimized. The convergence for energy is chosen as 10^{-5} eV between two steps, and the maximum force allowed on each atom is less than 0.01 eV/Å. The Brillouin zone (BZ) is sampled by (15x15x5) special **k**-points for primitive unit cell and scaled according to the size of supercells.

The calculations with SIESTA where the eigenstates of the Kohn-Sham hamiltonian are expressed as linear combinations of numerical atomic orbitals are performed. The exchange-correlation functional of the generalized gradient approximation is represented by the PBE approximation[64]. A 200 Ryd mesh cut-off is chosen and the self-consistent calculations are performed with a mixing rate of 0.1. Core electrons are replaced by norm-conserving, nonlocal Truoiller-Martins pseudopotentials. The convergence criterion for the density matrix is taken as 10^{-4}.

The Density Functional based Tight binding method (DFTB+) is based on a second-order expansion of the Kohn-Sham total energy in Density-Functional Theory (DFT) with respect to charge density fluctuations. In this approach, the reference electron density is obtained self-consistently from weakly confined neutral atoms and the confinement potential is optimized to predict the effective potential and charge density for molecules and solids. A minimal basis set is established tight-binding matrix elements are explicitly calculated within DFT framework. The DFTB+ program is orders of magnitude faster than standart DFT methods, but requires parameter files to be installed for all pair-wise combinations of atoms in a molecule or solid. In this work, the SlaterKoster (S-K) type parameter set[65] was implemented. All of our DFTB+ calculations only include s- and p-orbital interactions.

Adatom and graphene system breaks inversion symmetry and a net electric-dipole moment is generated perpendicular to the graphene surface. Dipole corrections[66] are applied in order to remove spurious dipole interactions between periodic images for the neutral calculations.

We add or remove electrons from the unit cell in order to simulate electron and hole doping. This is widely used method[67, 68, 69, 70] to simulate the effect applying a gate voltage to graphene-adatom system by changing the number of electrons. Normally, periodic boundary conditions realized by repeating charged supercells has a divergent electric potential energy and has drawbacks and limitations, which have been the subject matter of several studies in the past. To achieve the convergence of electronic potential, additional neutralizing background charge is applied[71, 66].

The amount of charging, ρ, is specified as either positive charging, i.e. electron depletion ($\rho > 0$), or negative charging, i.e. excess electrons, in units of $\pm$ electron (e) per number of atoms or per unit cell. Average surface charge density is specified as $\bar{\sigma} = Q/A$, i.e the charge per unit area, A, being the area of the unit cell.

It will be informative briefly discussing some works about charged calculations available in literature. Poloni and his co-workers[72] study the interplay between charge doping and intermolecular distance in the polymerization of C_{60} fullerene chains of using SIESTA. They show that the polymerization depends on both the center-to-center distance of fullerenes and the negative doping of the system. In particular, they observed that up to a doping of four electrons per two molecules, the energy barrier which is related to the formation energy of covalent bonds between fullerenes progressively decreases. Plane-wave calculations with PWscf package by Attaccalite and his co-workers[73] propose a new way of tuning the electron-phonon-coupling (EPC) in graphene by changing the deformation potential with electron/hole doping. The doping is simulated by changing the number of electrons in unit cell. They show that the EPC for highest optical branch at the K point in BZ acquires a strong dependency on the doping level due to electron-electron correlation. In another study, density functional tight

binding simulations (DFTB+) were used to explore the charging of graphene nanoflakes[74]. They try to determine the effective failure limit of graphene with respect to induced anionic charge produced by electron-beam or electric current. They predict that graphene flakes are resistant to high level of charging posing no problem to the operation of graphene-based electronic devices. But the localized regions were shown to be transformable from sp^2-bonded into sp^3-bonded material before the failure limit. Apart from doping, Ao and his co-workers[75] demonstrate that the applied electric field can significantly facilitate the binding of hydrogen molecules on N-doped graphene through dissociative adsorption and diffusion on graphene surface. By removing the electric field, the stored hydrogens on graphene can be released efficiently under ambient conditions when the hydrogen concentration is higher than 0.5 wt% which indicates that N-doped graphene can be used as hydrogen storage material with a storage capacity of 6.73 wt%. The electric field calculations were performed using DMOL3 code.

Assuming that varying the number of electrons in a adatom-graphene system can be used to simulate the effects of gate voltage, Chan and his co-workers[67] demonstrate the ionization of a Li and Co adatoms by doping. The ionization is accompanied by a sharp change in the electrostatic potential of the adatom. This results were consistent with recent STS experiments for Co on graphene[68]. In another study carried out using VASP code, Suarez and his co-workers[70] analyze the diffusion of oxygen adatoms on graphene and its dependence on the carrier density controlled by a gate voltage. The energy barrier which is related with the diffusivity of oxygen on graphene was predicted to be strongly dependent on the carrier density.

3.2 Charging of graphene

We first start with charging of graphene structure. Two-dimensional single layer of graphene layers separated with a vacuum space s between them are repeated periodically along the perpendicular z-direction as shown in Fig. 3.6 (a). The unit cell is made up of primitive unit cell containing 2 carbon (C) atoms. a=b is the

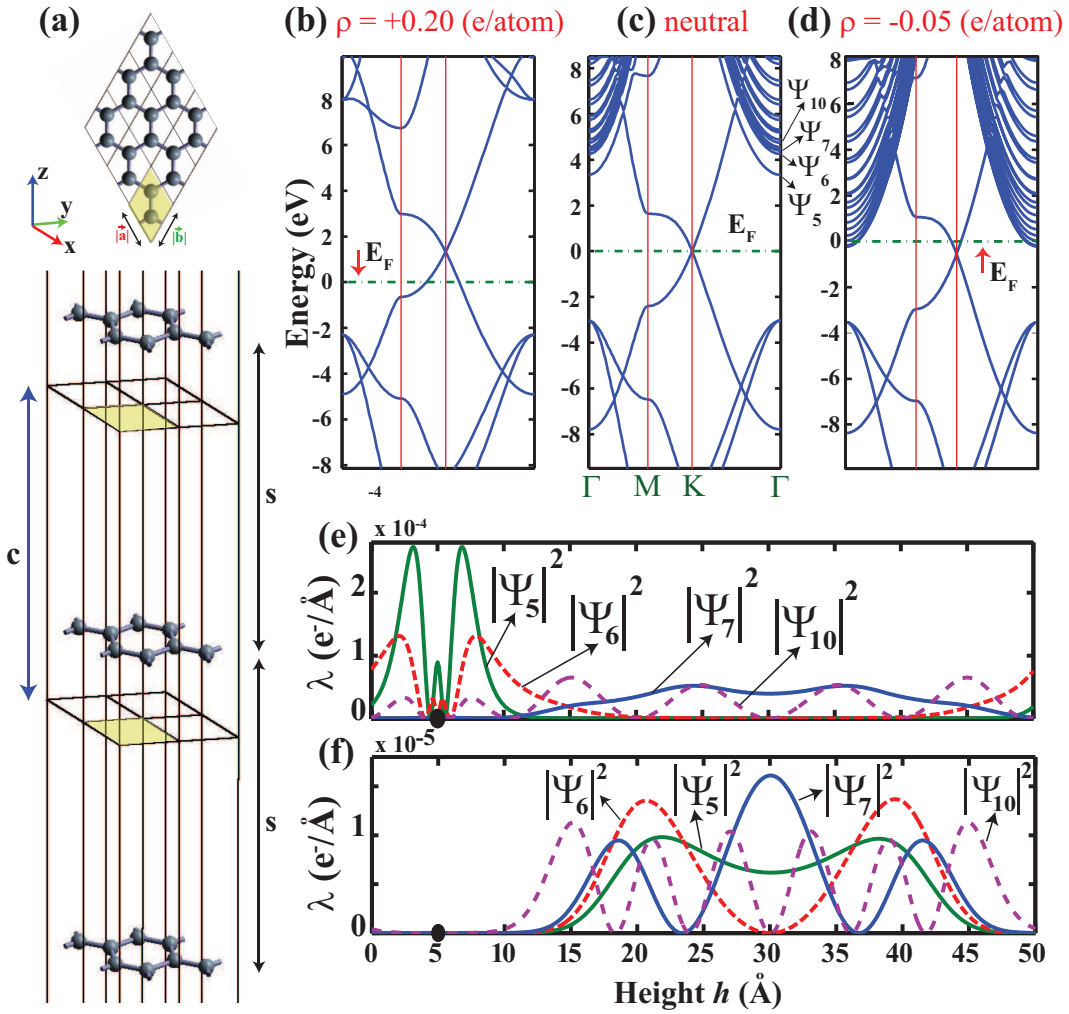

Figure 3.6: (a) Description of lattice used to treat 2D single layer graphene. a=b, c are the lattice constants, s is the vacuum spacing between adjacent layers. Primitive unit cell is shaded. (b) Energy band structure of positively charged graphene by ρ=+0.20 e/atom. (c) Neutral. (d) Negatively charged graphene by ρ=-0.05 e/atom, where excess electrons start to occupy the surface states. Zero of energy is set to Fermi level. (e) Planarly averaged charge density (λ) of states, Ψ_{5-10}, of neutral graphene. (f) Same as (e) after charging with ρ=-0.05 e/atom.

lattice constant of supercell in x-y plane and c=s is the distance along z-direction separating periodic graphene planes. The carbon pseudopotential used in this study contains 4 valance electrons. Therefore, there are 8 electrons in a primitive unit cell shown in Fig. 3.6 (a). The calculations are performed for s = 50 Å . When 0.4 electron is removed from the unit cell, this corresponds to ρ=+0.20 e/atom or $\bar{\sigma}$= 0.077 (e/A^2). Similarly addition of 0.1 electron corresponds to ρ=-0.05 e/atom or $\bar{\sigma}$= -0.019 (e/A^2).

The work function of neutral graphene is calculated to be 4.27 eV. Lowest two parabolic bands Ψ_5 and Ψ_6 in Fig. 3.6(c) have effective masses m*=1.05 and 1.02 m$_e$ (free electron mass) in the xy-plane parallel to the atomic plane of graphene. Hence they are nearly free electron like (NFE) in 2D , but they are bound above the graphene plane. These "surface" states[76] can be expressed as $\Psi_S \sim e^{i\mathbf{k}_\parallel \cdot \mathbf{r}_\parallel}\Phi(z)$, where $\mathbf{r}_\parallel$ and $\mathbf{k}_\parallel$ are in the xy-plane. Parabolic bands at higher energies becomes NFE in 3D. When the electrons are removed, the Fermi level is lowered from the Dirac point and positively charged graphene attains metallic behavior as in Fig. 3.6(b). At the end, the work function increases. However, under negative charging, whereby electrons are injected to the graphene, Fermi level raises above the Dirac point and eventually becomes pinned by NFE parabolic bands as in Fig. 3.6(d).

The planarly averaged charge density profiles of some of conduction states of neutral graphene is presented in Fig. 3.6 (e) labeled as $\Psi_5, \Psi_6, \Psi_7, \Psi_{10}$. These parabolic NFE bands start to get occupied around ρ=-0.015 e/atom (or surface excess charge density $\bar{\sigma}$=-0.0926 C/m^2). Upon charging the bound charge of Ψ_S states are further removed from graphene as shown in Fig. 3.6(f). While the Fermi level of negatively charged graphene rises and then is quickly pinned by the parabolic, nearly free electron like bands, it moves down readily by removal of electrons from graphene.

3.3 Charging of 2D monolayer MoS_2

The negative and positive charging of suspended monolayer MoS_2 is treated using supercell method similar to graphene in previous section. In Fig. 3.7 (a) we describe MoS_2 single layers, which are periodically repeated along the z-direction and separated by a vacuum spacing s between the adjacent outermost sulfur planes. In Fig. 3.7 (b) and (c) the self-consistent electronic potential energy, $V_{el}(\mathbf{r})$ is averaged in the planes perpendicular to the z-axis to obtain planarly averaged 1D potential energy $\bar{V}_{el}(z)$ for different values of s.

In the vacuum region, the electronic potential energy $\bar{V}_{el}(z)$ strongly depends on the vacuum spacing s. For an infinitely large single plane having excess charge $Q > 0$ per cell, the potential energy in the vacuum region is linear, if it is not periodically repeating. Thus, as $z \to \infty$, $\bar{V}_{el}(z \to \infty) \to +\infty$ as schematically shown in Fig. 3.7 (b). However, for a periodically repeating single layers (within the periodic boundary conditions) the potential energy is symmetric with respect to the center of vacuum spacing and it passes through a maximum at $s/2$. The maximum value of the potential increases with increasing s in Fig. 3.7(b).

In contrast, for a negatively ($Q < 0$ per cell) charged and infinite MoS_2 single layer, a reverse situation occurs as shown in Fig. 3.7 (c). Namely $\bar{V}_{el}(z \to \infty) \to -\infty$ linearly, if MoS_2 single layer is not periodically repeating. Notably, the energy of a finite size, single layer nanostructure (i.e. a flake) does not diverge, but has finite value for large z both for $Q > 0$ and $Q < 0$ cases. On the other hand, for periodically repeating single layers within the periodic boundary conditions, potential energies are symmetric with respect to the center of vacuum spacing and they passes through a minimum at $s/2$. This way a potential well is formed in the vacuum region between two adjacent layers. Normally, the depth of this well increases with increasing negative charging and s. At a critical value of negative charge, the self-consistent potential energy $V(\mathbf{r})$ including electronic and exchange-correlation potential energies dip below the Fermi level (even if $\bar{V}_{el}(z) > E_F$) and eventually electrons start to occupy the states localized in the quantum well. Such a situation is described in Fig. 3.8 (d)-(f). Of course, this situation suffers from the method of using plane-wave basis set and the repeating

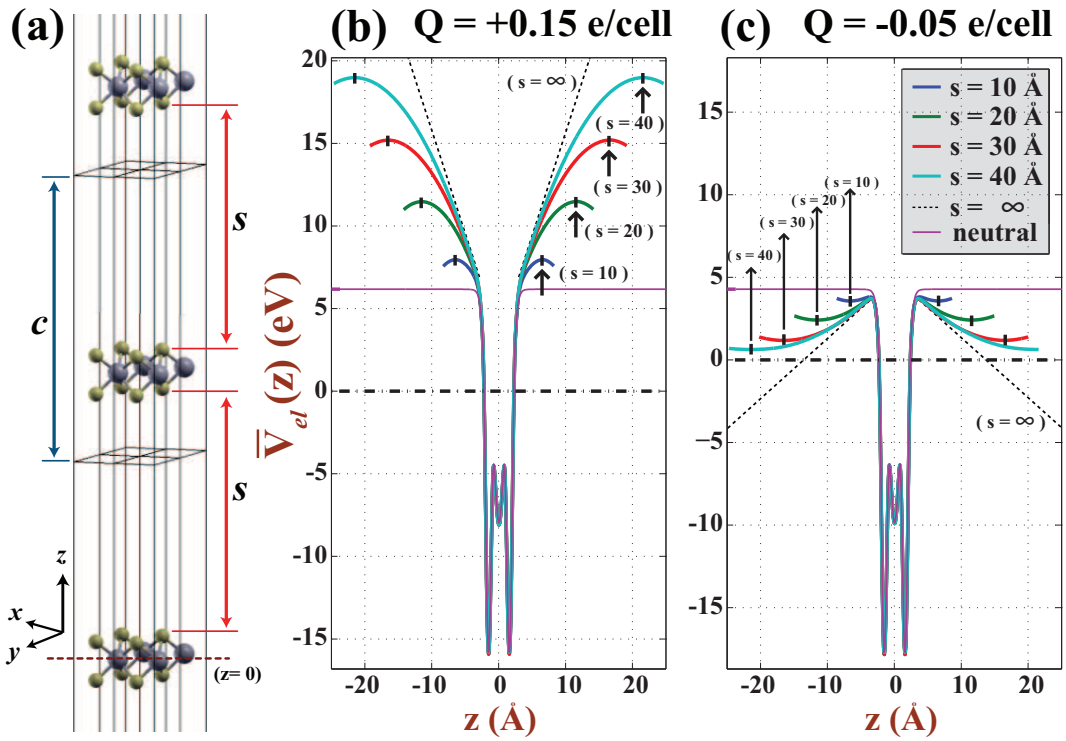

Figure 3.7: (a) Description of supercell geometry used to treat 2D single layer MoS_2. c and s are supercell lattice constant and vacuum spacing between adjacent layers. The z-axis is perpendicular to the layers. (b) Self-consistent potential energy of positively charged ($Q > 0$ per cell), periodically repeating MoS_2 single layers, which is planarly averaged along z-direction. $\bar{V}_{el}(z)$ is calculated using different vacuum spacings s as specified by inset. The planarly averaged potential energy of a single and infinite MoS_2 layer is schematically shown by linear dashed lines in the vacuum region. The zero of energy is set at the Fermi level indicated by dash-dotted lines. (c) $\bar{V}_{el}(z)$ of negatively charged ($Q < 0$ per cell) and periodically repeating MoS_2 single layers. Averaged potential energy of infinite MoS_2 single layer is shown by linear and dashed line in the vacuum region.

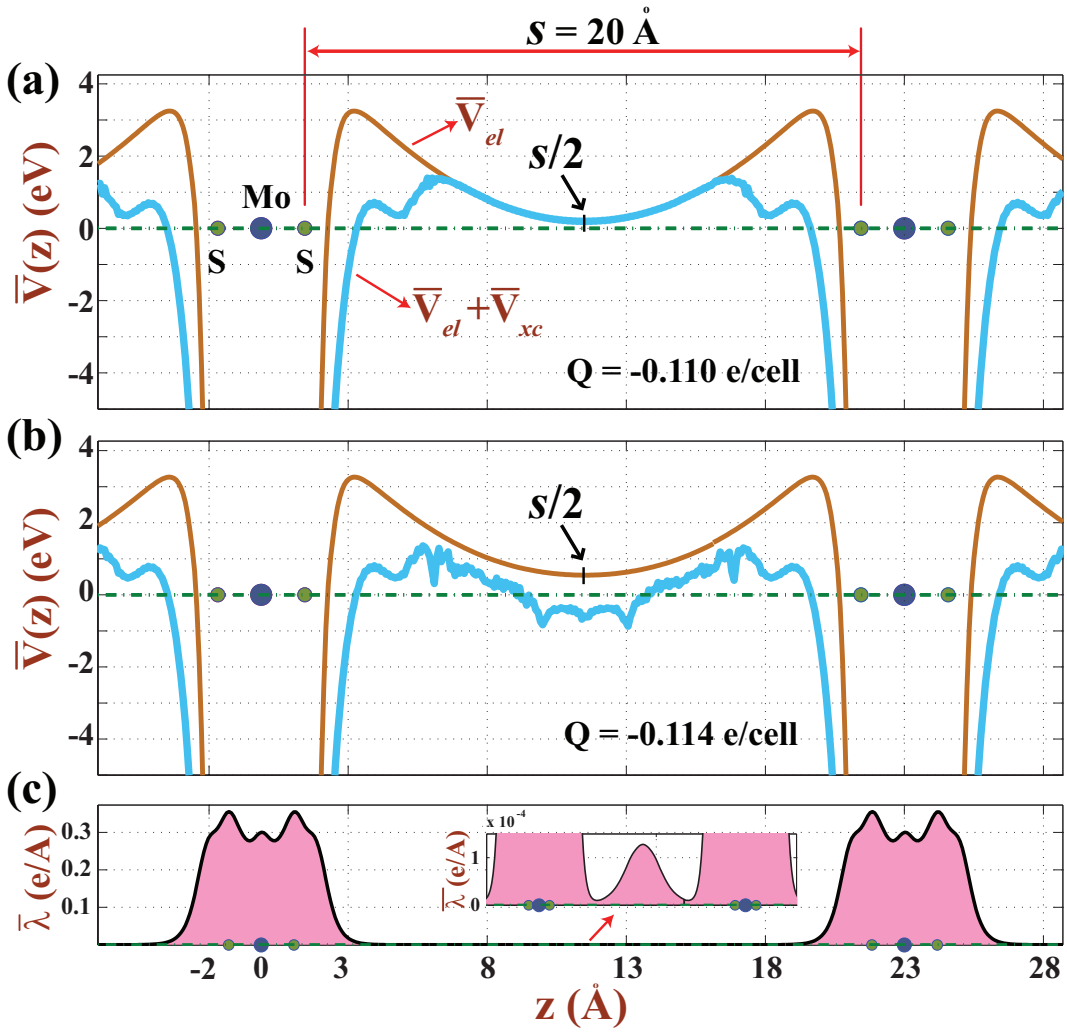

Figure 3.8: (a) Variation of $\bar{V}_{el}(z)$ and total potential energy including electronic and exchange-correlation potential, $\bar{V}_{el}(z) + \bar{V}_{xc}(z)$, between two negatively charged MoS_2 layers corresponding to Q=-0.110 e/unit cell before the spilling of electrons into vacuum. The spacing between MoS_2 layers is $s = 20$ Å. (b) Same as (d) but Q=-0.114 e/unit cell, where the total potential energy dips below E_F and hence excess electrons start to fill the states localized in the potential well between two MoS_2 layers. (c) Corresponding planarly averaged charge density $\bar{\lambda}$. Accumulation of the charge at the center of s is resolved in a fine scale. Arrows indicate the extremum points of $\bar{V}_{el}(z)$ in the vacuum region for $Q > 0$ and $Q < 0$ cases.

layers separated by the vacuum space s. Despite that, the method may provide reasonable description of the negatively charged layers until the minimum of the well dips below the Fermi level. According to this picture, the escaping of electrons out of the material is delayed in relatively short s. On the other hand, the interaction between layers prevents one from using too short s. Earlier, this limitation of the method is usually overlooked. The critical value of negative charge depends on s value. It should be noted that for s=20 Å, electrons start to escape from the graphene layer for Q=-4.03x10^{13} e/cm^2, even though larger doping of 4x10^{14} e/cm^2 has been attained for garphene on SiO_2 substrate[77].

3.4 Numerical solution of Schrödinger equation (SE) for 1D potential

In the case of positive charging, even if $\bar{V}_{el}(z)$ is not linear and does not increase to $+\infty$, the periodic boundary conditions using sufficiently large s can provide a realistic description of charged systems, since the wave functions in the vacuum region rapidly decay under high and wide potential barrier. Therefore, the calculated wave functions and electronic energies are not affected even if $\bar{V}_{el}(z)$ is smaller than the electronic potential corresponding to infinite vacuum spacing. We demonstrate our point of view by solving directly the Schrödinger equation to obtain the wave functions and energy eigenvalues for the planarly averaged 1D potentials of single layer and 3-layer graphene corresponding to s=12.5, 25, 50 Å in Fig. 3.9. One sees that the large difference, $\Delta\bar{V}_{el}(z) = \bar{V}_{el,s=50\mathring{A}}(z) - \bar{V}_{el,s=12.5\mathring{A}}(z)$ do not affect the occupied states at their tail region in the vacuum spacing; the energy difference is only 5 meV (which cannot be resolved from the figure) between smallest and largest vacuum spacing s, which is smaller than the accuracy limit of DFT calculations. As one expects, the dependence on the vacuum spacing increases for excited states, which have relatively larger extension and hence they are affected from $\Delta\bar{V}_{el}(z)$.

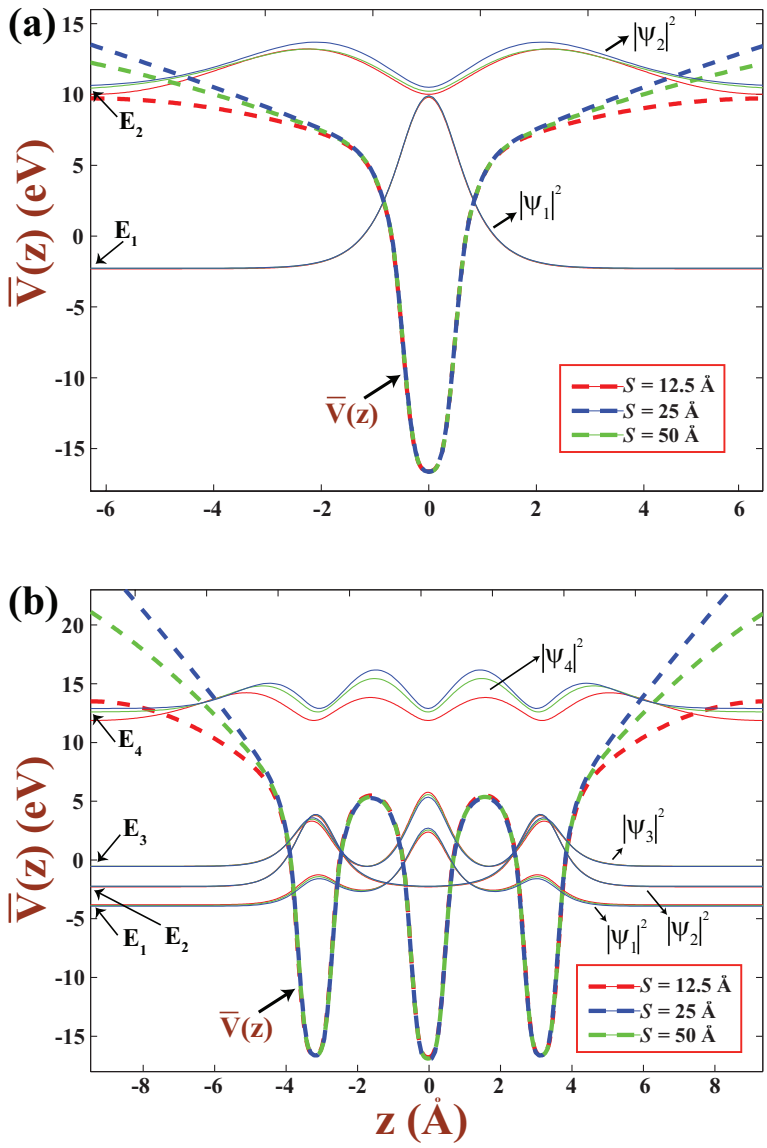

Figure 3.9: (a) Energy eigenvalues of the occupied electronic states, E_i and corresponding $|\Psi_i(z)|^2$ are obtained by the numerical solution of the Schrodinger equation of a planarly averaged, 1D electronic potential energy of single layer graphene for s=12.5 Å , 25 Å and 50 Å shown by dashed lines. (b) Same as (a) for 3-layer graphene. Zeros of $|\Psi_i(z)|^2$ at large z are aligned with the corresponding energy eigenvalues.

3.5 Effects of charging on electronic structure and bond lengths

By taking the above limitations of the method in negative charging into account, we now examine the effect of charging of single layers of graphene, CF, CH, BN and MoS_2 on their electronic structure and bond lengths. In Fig. 3.10 the changes in band structure with charging are significant within DFT. For example, the band gap (i.e. the energy gap between the top of the valence band and the minimum of the conduction band) of neutral single layer BN increases from 4.61 eV to 5.12 and to 5.54 eV as Q increases from Q=0 to +0.2 e/cell and to +0.4 e/cell, respectively. The increase of the band gap occurs due to the fact that the electronic potential energy becomes deeper with increasing electron depletion. For $Q > 0$, the Fermi level dips in the valance band and creates holes.

In contrast, parabolic free electron like bands, which occur above the vacuum level in the neutral case, start to descend as a result of negative charging ($Q < 0$) and eventually they touch the Fermi level. Upon increasing Q these parabolic bands start to be occupied and hence part of Q is transferred to the quantum well in the vacuum region. This way the rate of accumulation of excess charge in the conduction band of single layer nanostructure recedes. Even if these parabolic bands appear as touching the Fermi level in the same band structure in (k_x, k_y)-plane they are physically separated from the states of single layer honeycomb structure under study. As it was mentioned before, this situation is an artifact of periodic boundary conditions and can be viewed as the vanishing of the work function. We note that in the case of negatively charged, finite size single-layer, the excess electrons are hindered from spilling out to the vacuum by a wide tunneling barrier, even if $\bar{V}_{el}(z)$ is lowered below the Fermi level in vacuum for large z.

Incidentally, for both $Q > 0$ and $Q < 0$, the spin-polarized calculations carried out for single layers of graphene, CH, CF, BN and MoS_2 did not yield any magnetic state as a result of charging.

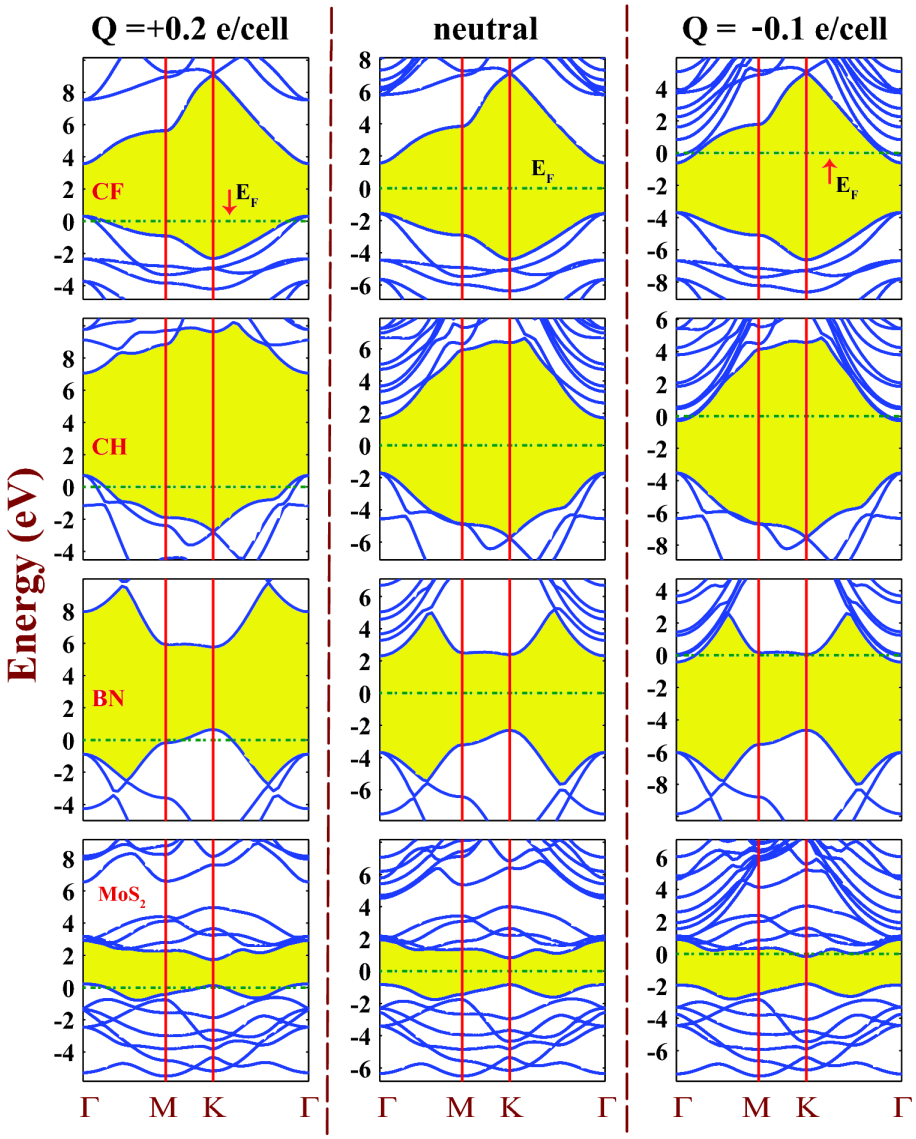

Figure 3.10: Energy band structures of 2D single layer of fluorographene CF, graphane CH, BN and MoS_2 calculated for $Q = +0.2$ e/cell, $Q = 0$ (neutral) and $Q = -0.10$ e/cell. Zero of energy is set at the Fermi level indicated by dash-dotted lines. The band gap is shaded. Note that band gap increases under positive charging. Parabolic bands descending and touching the Fermi level for $Q < 0$ are free electron like bands. Band calculations are carried out for s=20 Å.

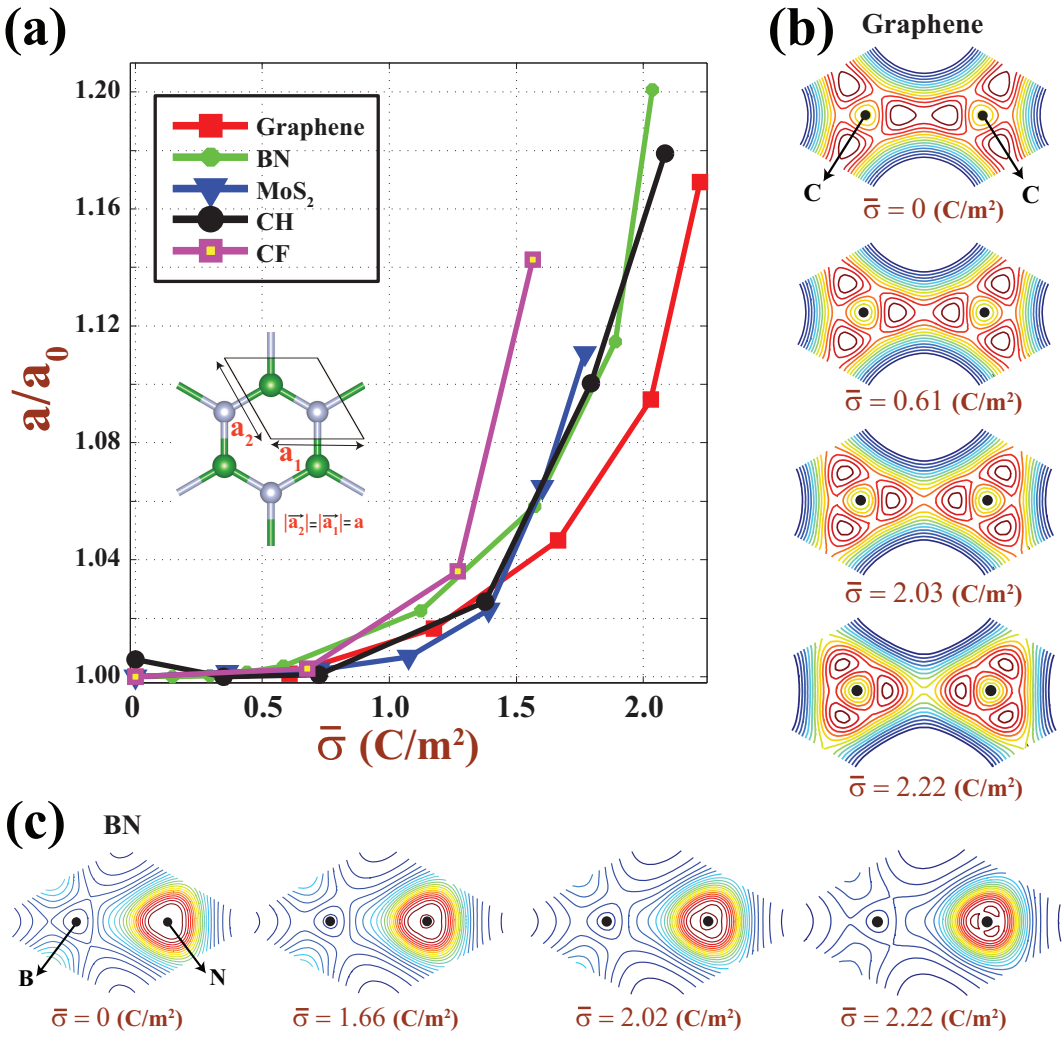

Figure 3.11: (a) Variation of the ratio of lattice constants a of positively charged single layer graphene, BN, CH, CF and MoS_2 to their neutral values a_o with the average surface charge density, $\bar{\sigma}$. The unit cell and the lattice vectors are described by inset. (b) The charge density contour plots in a plane passing through a C-C bond. (c) Same as B-N bond.

Another crucial effect of charging appears in the variation of the bond lengths with Q. As shown in Fig. 3.11 (a) the bond length or lattice constants of single layer graphene, BN, CH, CF and MoS_2 increase with increasing positive charge density $\bar{\sigma}$. The elongation of the bond length is slow for small $\bar{\sigma}$, but increases quickly when $\bar{\sigma}$ 1 C/m^2. The bonds get longer when the electrons are removed from the system and hence bonds become weaker. The contour plots of total charge density in a plane passing through C-C and B-N bonds of graphene and BN honeycomb structures in Fig. 3.11 (b) and (c), show that the charge density between atoms becomes weaker with increasing electron depletion. Weakening of bonds can have crucial consequences as phonon softening and is observable through Raman spectrum. In fact, the Raman active mode of graphene calculated by using density functional perturbation theory is at 1524 cm^{-1} and shifts down to 1510 cm^{-1} for Q=+0.2 e/cell, and to 1311 cm^{-1} for Q=0.4 e/cell. To confirm whether the elongation of bonds dominates the Raman shift of graphene, we calculated the Raman active modes of neutral graphene having the same lattice constant of graphene when charged by Q=+0.4 e/cell. In this case the Raman active mode shifted to 1274 cm^{-1}, which is close to the Raman active mode calculated for graphene charged with Q=+0.4 e/cell. We also note that the excessive charging of single layer materials considered in this paper lead to instability. This is revealed from phonon dispersion calculations. For example, neutral graphene which has normally stable planar structure and positive frequencies of acoustical branches in BZ, starts to attain imaginary frequencies of long wavelength acoustical modes at excessive charging. Weakening of graphene layer is expected to be reflected to its elastic properties, in particular to its stiffness[78].

3.6 Exfoliation of layered graphene, BN and MoS_2

The investigation of the exfoliation of graphite slab consisting of 3 layers of graphene as a result of charging is presented in Fig. 3.12. When negatively charged, the excess electrons are mainly accumulated on both surfaces, but with

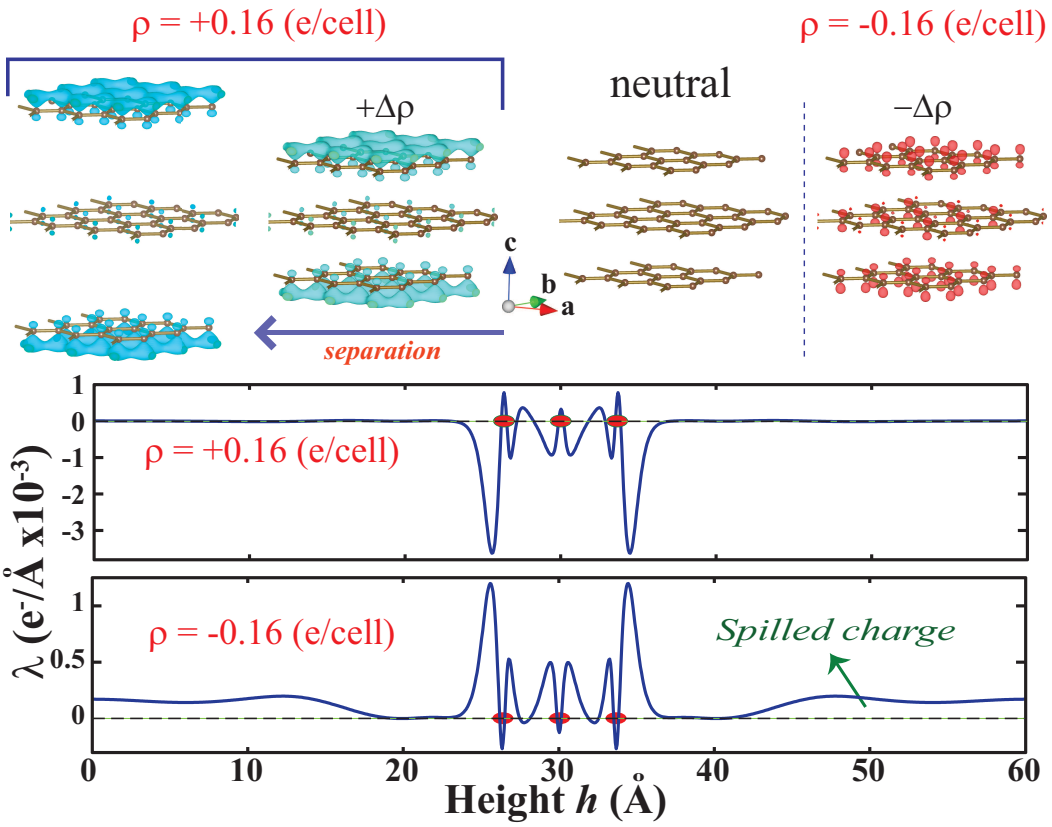

Figure 3.12: Exfoliation of graphene layers from both surfaces of a 3-layer graphite slab (in AB-stacking) caused by electron removal. Isosurfaces of difference charge density, $\Delta\rho$, show the electron depletion. The excess charge on the negatively charged slab is not sufficient for exfoliation. The distributions of planar averaged charge density (λ) perpendicular to the graphene plane are shown below both for positive and negative charging.

smaller amount at the middle layer. The effect of charging on structure is minute, since the bonds are intact and the excess electrons rapidly spill out towards the vacuum. However, the situation is dramatically different for the case of positive charging. The charge isosurfaces in Fig. 3.12 shows that positive charge, occurs mainly on both surfaces (i.e. first and third graphene layers), whereas the middle graphene has relatively small positive charge. This is an expected result for a metallic system. The interlayer interaction in the neutral 3-layer slab is attractive and is calculated to be 17 (36) meV/atom calculated by LDA (GGA+vdW), which becomes even weaker upon depopulation of π-orbitals. GGA+vdW calculations predict that a threshold charge, Q=0.16 e/cell gives rise to exfoliation of two outermost layers. LDA calculations yield relatively lower threshold charge of Q=0.14 e/cell. We also performed a systematic analysis of exfoliation for thicker slabs consisting of 5-10 layers of graphene. We found that the threshold charge increases with increasing slab thickness. However, our analysis based on the planar averaged charge densities suggest that the exfoliation of outermost layers occurs when approximately the same amount of positive charge is accumulated on the outermost layers. For example, the exfoliation of 3-layer and 6-layer graphene flakes take place when their outermost layers have positive charge of 0.065 and 0.066 e/cell, respectively. On the other hand, increasing of threshold charge by going from 3-layer to 6-layer occurs due to the charge spill to the inner layers. This situation can be explained by a simple electrostatic model, where the outermost layers of slabs is modeled by uniformly charged planes, which yield repulsive interaction independent of their separation distance, i.e. $F \propto q^2/(A\cdot \epsilon_0)$, where q is excess positive charge per unit cell with the area A. Nonetheless, these values of charging are quite high, and can be attained in small flakes locally by the tip of Scanning Tunnelling Microscope.

We next investigate the exfoliation of single layer BN and MoS_2 from their layered bulk crystal through charging. We model 3-layer slab (sheet) of BN and MoS_2 as part of their layered bulk crystal. We considered only 3-layer slabs in order to cut the computation time, since the model works also for thicker slabs consisting of 6-10 layers graphene. Energy minimizations of neutral sheets relative to stacking geometry are achieved. Stacking of 3-layer BN and MoS_2 slabs comply

Table 3.1: Dependence of the threshold charges on the vacuum spacing s (Å) between 3-layer slabs. Threshold charge, Q_e (e/cell) where exfoliation sets in and corresponding threshold average surface charge density $\bar{\sigma}_e = Q_e/A$ (C/m^2) are calculated for positive charged 3-layer Graphene, BN and MoS_2 sheets for s=50 Å and s=20 Å. The numbers of valence electrons per unit cell of the slab are also given in the second column.

System	# of e	Q_e (e/cell)	$\bar{\sigma}$ (C/m^2)
3-layer Graphene (s=50)	24	+0.160	+0.49
3-layer Graphene (s=20)	24	+0.205	+0.62
3-layer BN (s=50)	24	+0.225	+0.66
3-layer BN (s=20)	24	+0.320	+0.94
3-layer MoS_2 (s=50)	54	+0.322	+0.57
3-layer MoS_2 (s=20)	54	+0.480	+0.86

with the stacking of layers in 3D layered BN[47] and MoS_2 crystals[50]. In these slabs, the layers are hold together mainly by attractive vdW interactions of a few hundreds meV and any repulsive interaction overcoming it leads to exfoliation. When electrons are injected to or removed from the slab, the Fermi level shifts up or down and cross the conduction or valance band of the insulator and attribute to it a metallic character. At the end, the excess charge by itself accumulates on the surfaces of the metallic slab inducing a repulsive Coulomb interaction between the outermost layers of the slab. Here we consider positive charging only, since in the case of negative charging the excess charges quickly spill into the vacuum before the exfoliation sets in.

The amount of charge in the unit cell, which is necessary for the onset of exfoliation, is defined as the threshold charge Q_e. Threshold charges are calculated for 3-layer slabs of graphene, BN and MoS_2 for s=20 Å and s=50 Å. Results presented in Tab.3.1 indicate that the amount of threshold charge decreases with increasing s. This confirms our arguments in Sec. III that in positive charging large vacuum space, s, is favored. The mechanism underlying this finding is summarized in Fig. 3.13 where we show the linear charge density, $\bar{\lambda}(z)$ calculated for different s values of a 3-layer BN. For small s, the excess charge accumulates mainly at surfaces of the slab, also with some significant fraction inside the slab. However, as s increases some part of Q is transferred from inside to the outer surface giving rise to the increase of the charge accumulation at the surface. At

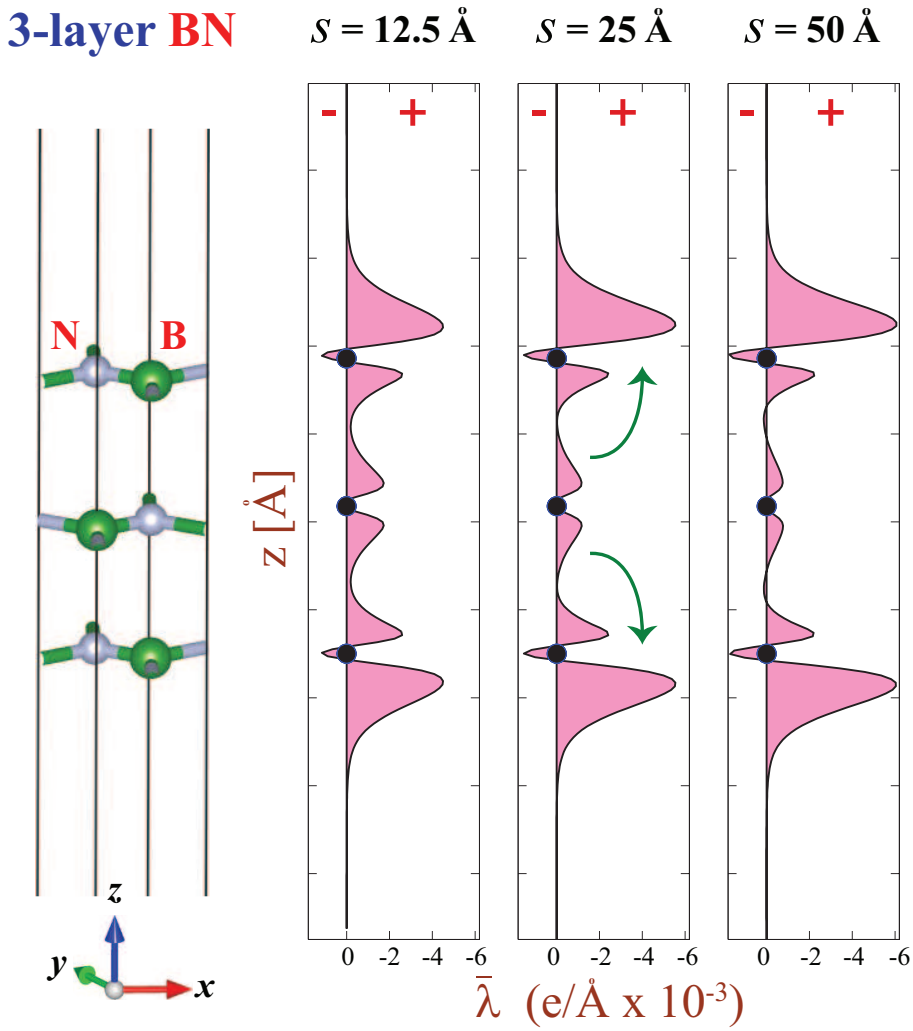

Figure 3.13: Variation of planarly averaged positive excess charge $\bar{\lambda}(z)$ along z-axis perpendicular to the BN-layers calculated for different s. As s increases more excess charge is transferred from center region to the surface planes.

the end, for the same level of charging the induced Coulomb repulsion increases with increasing s. Accordingly, the same slab requires relatively smaller amount of threshold charge Q_e to be exfoliated, if s is taken large.

In Fig. 3.14 we present the variation of the cohesive energy of the 3-layer BN slab relative to three free BN layers for neutral $Q = 0$ and positive charged $Q > 0$ cases as a function of the distance L between the outermost BN atomic planes of 3-layer BN slab. The cohesive energy for a given L is obtained from the following expression: $E_C = E_T$ [3-Layer BN] - $3E_T$ [single layer BN]. The total energy of the single layer BN, E_T [single layer] is calculated in a smaller supercell to keep the density of the background charge the same. The cohesive energy of the neutral slab in equilibrium is $\sim$ 302 meV/cell. If the spacings of layers (i.e. L) starts to increase, an attractive force $F_\perp = -\partial E_T/\partial L$ acts to restore the equilibrium spacing. $F_\perp(L)$ first increases with increasing L, passes through a maximum and then decays to zero. In Fig. 3.14 we also show how the minimum of cohesive energy decreases and moves to relatively large spacings with increasing Q. Concomitantly, the maximum of the attractive force for a given Q, $F_{\perp,max}$ decreases with increasing Q and eventually becomes zero. This give rise to the exfoliation. We note that despite the limitations set by the neutralizing uniform charge on the total energy, the cohesive energies calculated for different charge levels reveal useful qualitative information on the effects of charging.

The threshold values of static charge, Q_e, to be implemented in the slabs to achieve exfoliation are quite high. Such high static charging of layers can be achieved locally through the tip of Scanning Tunnelling Microscope or electrolytic gate[77]. The dissipation of locally created excess charge in materials may involve a decay time τ_D. Relatively longer τ_D can induce a local instability and the desorption of atoms from nanoparticles. Experimentally ultra-fast graphene ablation was directly observed by means of electron crystallography[79]. Carriers excited by ultra-short laser pulse transfer energy to strongly coupled optical phonons. Graphite undergoes a contraction, which is subsequently followed by an expansion leading eventually to laser-driven ablation[79]. Much recently, the understanding of photoexfoliation have been proposed, where exposure to femtosecond laser pulses has led to athermal exfoliation of intact graphenes.[80]

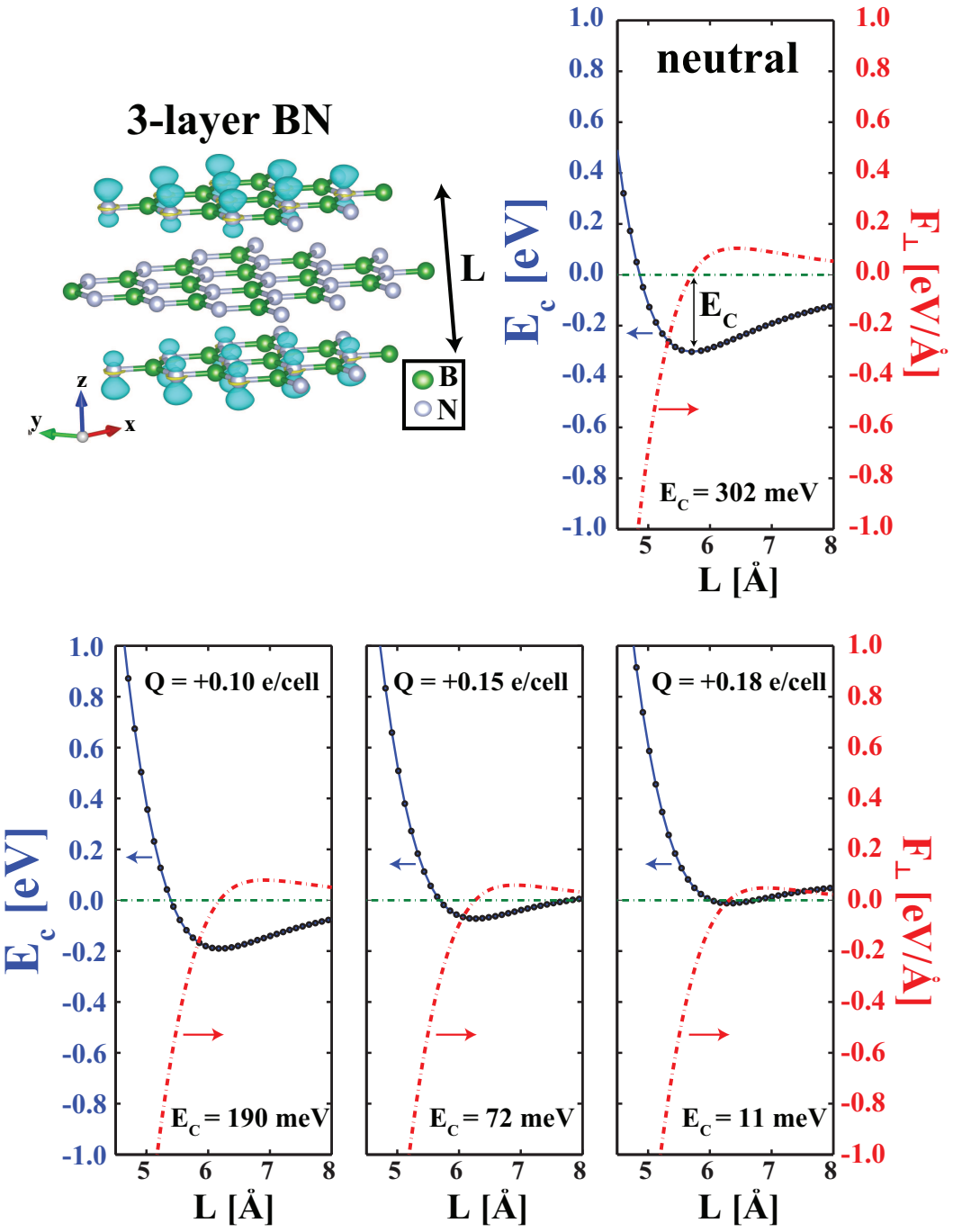

Figure 3.14: Variation of cohesive energy and perpendicular force $F_\perp$ in 3-layer BN slab as a function of the distance L between the surfaces. Energies and forces are calculated for different levels of excess positive charge Q (e/unit cell). Zero of energy corresponds to the energy as $L \to \infty$.

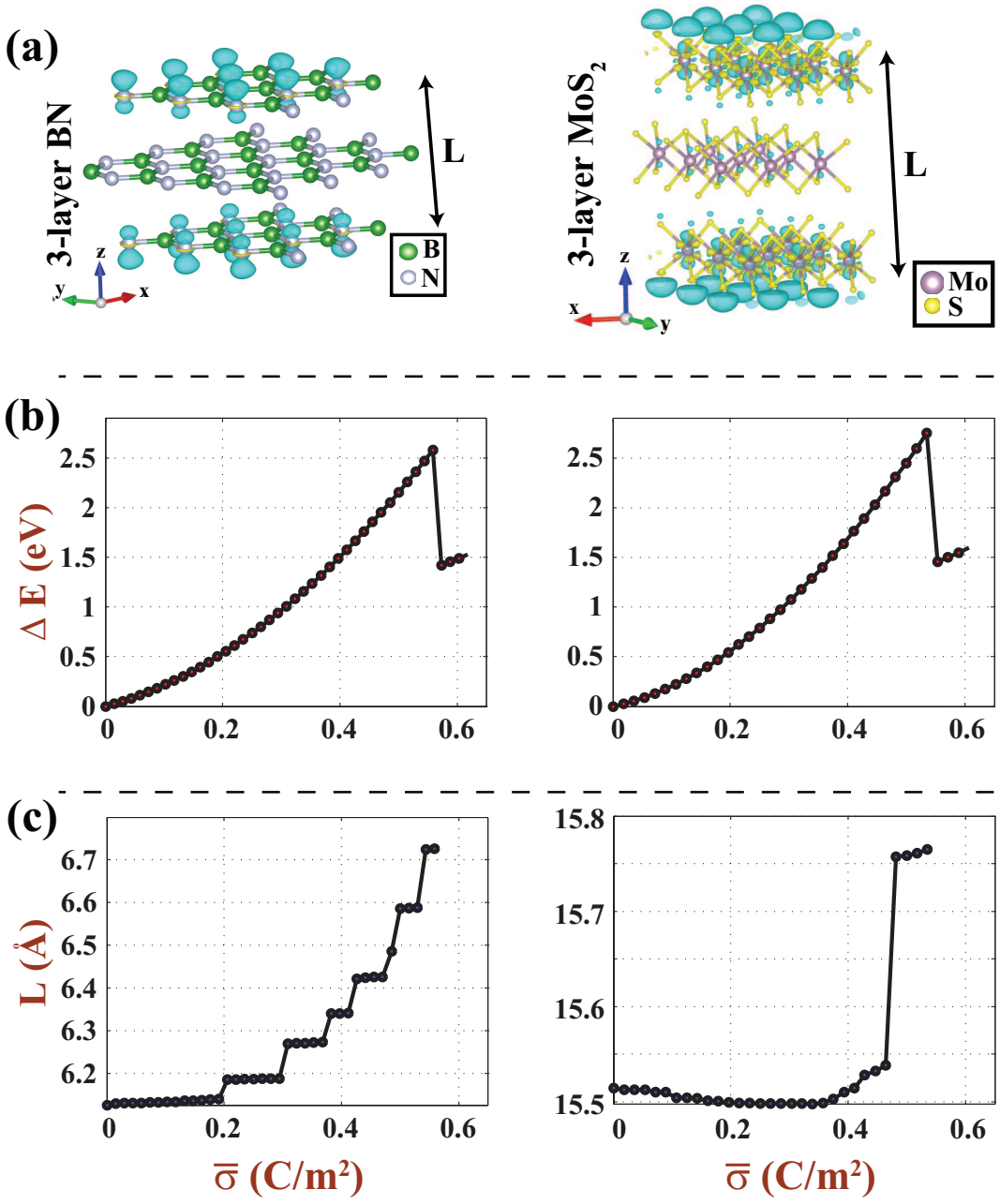

Figure 3.15: Exfoliation of outermost layers from layered BN and MoS_2 slabs by positively charging of slabs. (a) Turquoise isosurfaces of excess positive charge density. (b) Change in total energy with excess surface charge density. (c) Variation of L of slabs with charging.

Based on time dependent DFT calculations (TD-DFT), it is proposed that the femtosecond laser pulse rapidly generates hot electron gas at $\sim$ 20.000 K, while graphene layers are vibrationally cold. The hot electrons spill out, leaving behind a positively charged graphite slab. The charge deficiency accumulated at the top and bottom surfaces lead to athermal excitation[80]. The exfoliation in static charging described in Fig. 3.15 is in compliance with the understanding of photoexcitation revealed from previous TD-DFT calculations[80], since the driving force which leads to the separation of graphenes from graphite is mainly related with electrostatic effects in both methods.

In Fig. 3.15 (a) we show isosurfaces of excess positive charge densities of 3-layer BN and MoS_2 slabs. These slabs become metallic upon extracting electrons (i.e. upon positive charging) and excess charges reside at both surfaces of slabs. As shown in Fig. 3.15 (b), the total energy raises with increasing charging or average charge density, $\bar{\sigma}$. In compliance with Fig. 3.14, the separation between surface layers, L, increases. The sharp drop of ΔE at Q_e or $\bar{\sigma}_e$ indicate the onset of exfoliation due to the repulsive Coulomb force pulling them to exfoliate. In Fig. 3.15 (c) L increases with increasing charging as discussed in Fig. 3.14. The increments of L exhibits a stepwise behavior for BN. This is also artifact of the method, where forces are calculated within preset threshold values.

The variation of L of MoS_2 slab with $Q > 0$ display a different behavior due to charge transfer from Mo to S atoms. The exfoliation due to the static charging can be explained by a simple electrostatic model, where the outermost layers of slabs is modeled by uniformly charged planes, which yields repulsive interaction independent of their separation distance, i.e. $F \propto Q^2/(A \cdot \epsilon_0)$, where ϵ_0 is static dielectric constant. Calculated forces differ from the classical force due to screening effects of excess charge residing inside the slabs.

3.7 Charging of 1D graphene flakes

The effects of charging becomes emphasized when the size of graphene flake is small. In this respect, the flake behave like a quantum dot and hence energy level structure is affected strongly. The flake we consider has a rectangular shape and hence it consists of armchair, as well as zigzag edges as shown in Fig. 3.16. It is therefore antiferromagnetic ground state when neutral. Isosurfaces of difference charge density, $\Delta\rho$, of the same flake for three different charge state are shown in Fig. 3.16(a). $\Delta\rho$ is calculated by subtracting the total charge density of the neutral flake from that of charged ones. For a better comparison, charge density of the neutral flake is calculated using the atomic structure of the charged ones. It is seen that the edge states due to zigzag edges are most affected from charging. In Fig. 3.16 (a), while charge is depleted mainly from edge states, excess electrons are accumulated predominantly at the zigzag edges. As shown in Fig. 3.16 (b), while the antiferromagnetic state of the flake is unaltered, charging causes emptying and filling of HOMO and LUMO states, changing of level spacings and their energies relative to vacuum level. Additionally, magnetic moments of zigzag edge atoms are strongly affected depending on the sign of charging in Fig. 3.16 (b). In particular, the binding energies and magnetic moments of specific adatoms depends on its position and charging of the flake. In Fig. 3.16 (c) we consider Li and Ti,which normally adsorbed to graphene by donating charge. Generally, the binding energies increases (decreases) with positive (negative) charging. We also found that the effects of monopole and dipole corrections on the effects of charging on the binding energies is minute. For example, the binding energy of Li, when 2 electrons are removed, increases from 2.756 to 2.764 upon corrections. However, the effect of charging becomes more pronounced when the adatom is placed close to the edge of positively charged flake since the additional charges are mostly confined at the edges. Similarly, the magnetic moment at the adatom site varies depending the adsorption site and charging state of the flake.

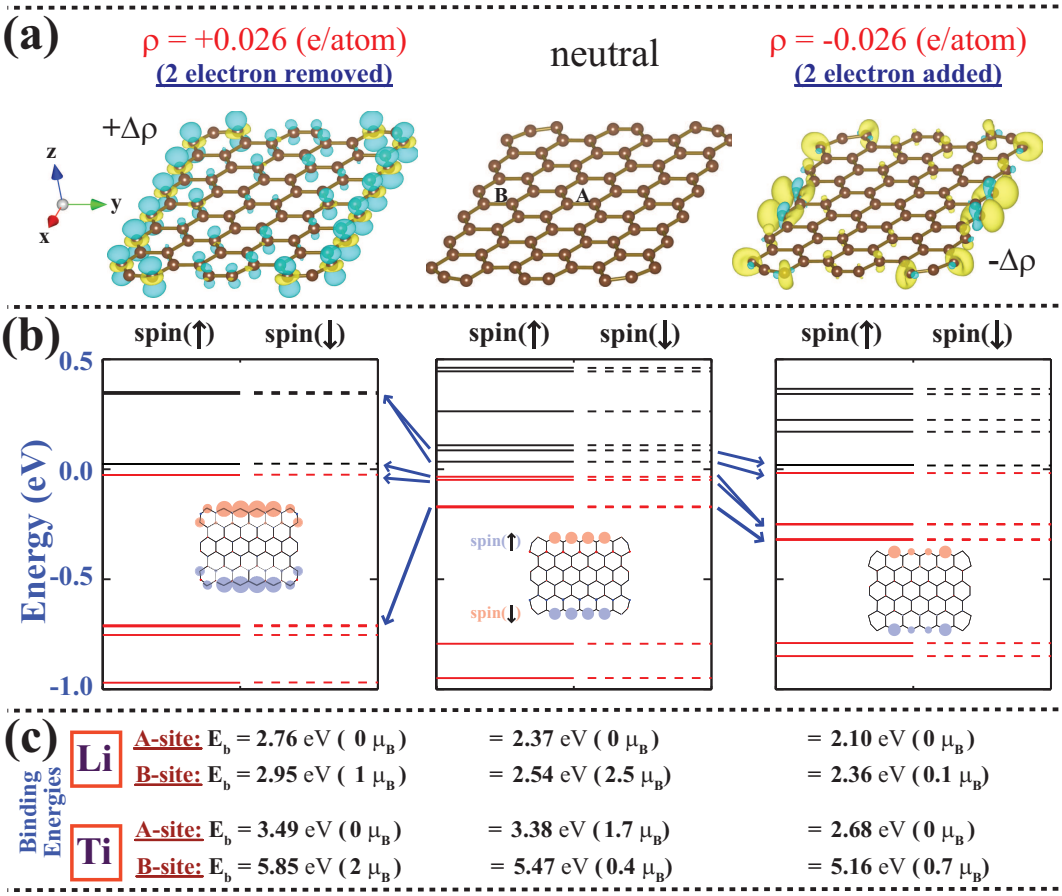

Figure 3.16: Effect of charging on graphene flake consisting of 78 carbon atoms. (a) Isosurfaces of difference charge density $\Delta\rho$ of positively charged, neutral and negatively charged slabs. (b) Corresponding spin-polarized energy level structure. Solid and continuous levels show spin up and spin down states. Red and black levels indicate filled and empty states, respectively. Distribution of magnetic moments at the zigzag edges are shown by insets. Zero of energy is set to Fermi level.(c) Variation of binding energy and net magnetic moment of specific adatoms adsorbed in two different positions, namely A-site and B-site indicated in (a).

3.8 Atomic-orbital vs plane-wave calculations

In this section we make a comparison of atomic-orbital based codes (SIESTA and DFTB+) and plane-wave code (VASP) for neutral and charged calculations. The one electron wave function $\psi(\boldsymbol{r})$ is expressed as a linear combination of atomic orbitals $\phi(\boldsymbol{r})$. These orbitals can be products of a spherical harmonic and radial function. For an atom I, situated at a position R_I,

$$\phi_{Ilmn}(\mathbf{r}) = R_{Iln}(|\vec{r}_I|)\, Y_{lm}(\hat{r}_I) \tag{3.4}$$

where $r_I = r$ - R_I. In plane-wave calculations, the wave function is expressed as:

$$\Psi_i(\mathbf{r}) = \sum_G a_{i,k+G} e^{i(\mathbf{k}+\mathbf{G})\mathbf{r}} \tag{3.5}$$

The advantages of plane-waves are that there are very efficient algorithms for performing Fourier transformations allowing calculations in the most efficient space - reciprocal or direct space. The convergence of physical properties are controlled by a single parameter, the energy cutoff. They provide the same accuracy at all points in space regardless of atomic positions. However their disadvantage is that they require hundreds of wave functions per atom to achieve a good accuracy and it is essential to use periodic supercells if plane-waves are used. The advantages of atomic orbitals are that they are very efficient since the number of basis functions needed are usually small compared to plane-waves. This reduces CPU time and memory requirements. In addition the physical interpretations are straightforward (population analysis, projected density of states...) However they re lack of systematic way of convergence and it requires human and computational efforts searching for a good basis set before doing a realistic calculations.

In Fig. 3.17 we present the band structure calculations for neutral graphene performed with plane-wave (VASP) and atomic orbitals (SIESTA and DFTB+). The lattice constants and number of k-points are the same for each calculation.

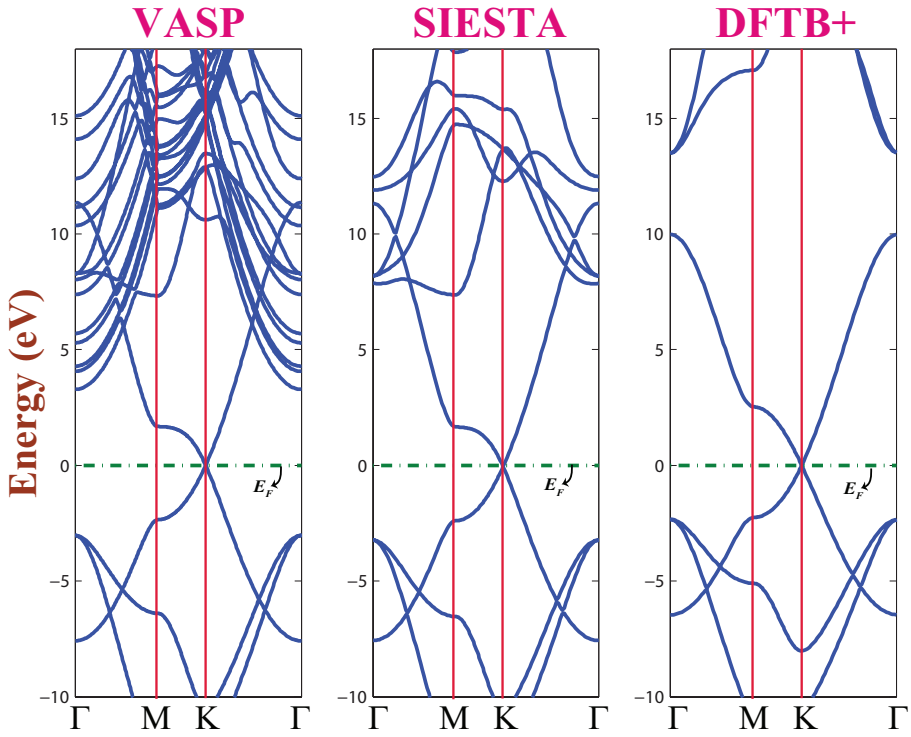

Figure 3.17: The comparison of the energy band structures of neutral graphene calculated with VASP, SIESTA and DFTB. The Fermi level is set to zero energy. The unit cell parameters are same for each calculation.

However the computational times are two orders of magnitude smaller for atomic orbital calculations compared to plane-wave calculation. As seen from the figure, the valance bands are almost identical for VASP-SIESTA and very similar to DFTB+ results. Each method successfully predict the Dirac-fermion behavior of graphene at K-point where conduction and valance bands cross linearly. However, the situation is remarkably different for conduction states. There are free-electron like states starting around 4.5 eV for VASP band structure calculations which are missing for SIESTA and DFTB+ results. This can be interpreted as the absence of free-electron-like basis functions in the eqn. 3.4 which are required to describe those bands observed in VASP calculations.

The charged calculations of graphene structure performed with plane-wave (VASP) and atomic orbitals (SIESTA and DFTB+) is presented in Fig. 3.18 when 0.2 electron is added to the unit cell containing 2 carbon atoms and hence the total amount of electron is 8.2 e. The height of unit cell is c=s=20 Å . In Fig. 3.18 (a) we present the band structure calculations calculated with VASP, SIESTA and DFTB+. As discussed in previous sections the free-electron-like bands gets occupied upon charging for VASP calculations. The Fermi level is approximately 0.435 eV above the Dirac point and the system gets metallic. Addition of extra electrons do not increase the Fermi level and additional electrons are occupied by vacuum bands. However, for the case of SIESTA and DFTB+ calculations, the Fermi level is approximately 1 eV above the Dirac point. Since the SIESTA and DFTB+ conduction bands do not include free-electron-like states, the additional charge can be only occupied with atomic orbitals and this leads to increase of Fermi level to energies higher than in VASP calculations.

We further analyze the effects of charging by planarly averaging the total potential as presented in Fig. 3.18 (b). The VASP profile has wells where the Fermi is above the potential line. These wells correspond to the regions where the electronic states can be confined. If we further plot the planarly averaged total charge density along the height of unit cell as in Fig. 3.18 (c) we observe the accumulation of electronic charges in these wells. As shown in the inset figure, the charge density makes its peak on the plane where carbon atoms are situated. The

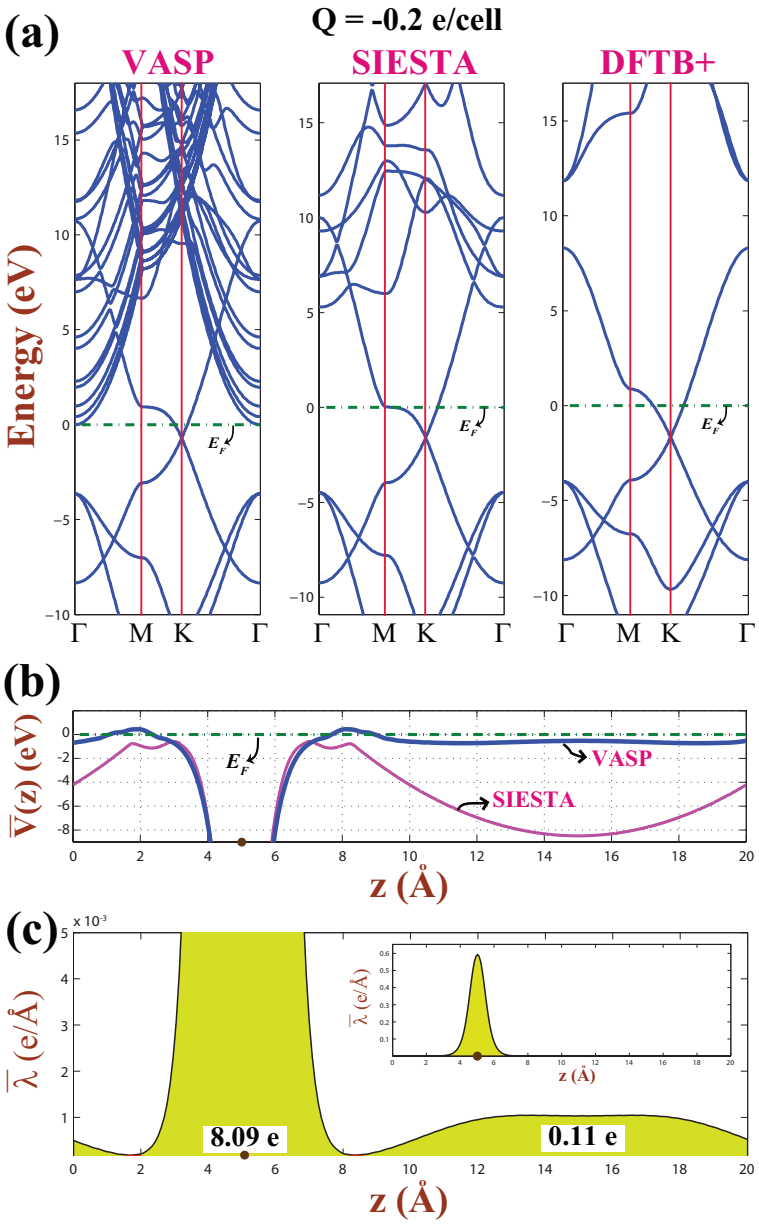

Figure 3.18: (a) Band structures of charged graphene when 0.2 electron is added to the unit cell calculated with VASP, SIESTA and DFTB+. The Fermi level is set to zero energy. The unit cell parameters are same for each calculation. (b) Planarly averaged total potential energy, V(z), calculated with plane-wave basis VASP and atomic-orbital basis SIESTA. The carbon atoms are at z = 5 Å and length of unit cell along z-direction is 20 Å . (c) Planarly averaged total charge density calculated with VASP.

negative charge is 0.20 electron. By integrating the charge density along the z-direction, it is calculated that the 8.09 electrons accumulates on graphene surface and 0.09 of this charge is additional charge while the rest of extra charge (0.11 e) is accumulated in the vacuum region. This indicates that almost half of the extra electrons are spilled out to vacuum region. This is an artifact of the plane-wave calculations for negatively charged slabs that we discussed in previous sections. The total potential calculated with SIESTA is also presented in Fig. 3.18 (b). Although the potential profile is below the Fermi level for the regions in vacuum, the SIESTA calculations do not result in electron accumulation in the vacuum in contrast to VASP calculations. All extra electronic charge is on graphene plane.

Chapter 4

Oxidation of graphene

In this chapter we present an extensive analysis of the oxygen adatom adsorption by using first principles calculations based on Density Functional Theory (DFT). In order to understand the reversible oxidation-deoxidation processes[81, 1] we consider only the adsorption and oxidation of graphene surfaces in spite of the fact that hydroxyl groups are also coadsorbed. Earlier studies followed approaches, which determines the optimized geometries corresponding to the minimum of total energy. Here, we show that the oxidation mechanism is mainly governed by the charge density profile of graphene, which is modified by each adsorbed oxygen in the course of oxidation. At the end, oxidized regions of graphene form domains instead of a uniform coverage. The oxygen adsorption on both sides of graphene was shown to be energetically more favorable than the adsorptin to only one side. The repulsive interaction between two oxygen adatoms at the close proximity is repulsive and hinders oxygen desorption through O_2 formation. We finally showed that the distribution of oxygen atoms on graphene affects the electronic properties. Even if the massless Dirac-fermion behavior of graphene can be recovered for patterns conserving specific symmetries, the band gap normally increases with increasing non-uniform oxygen coverage and attains the value as high as 3 eV. These results are critical for the device applications based on reversible oxidation-deoxidation of graphene surfaces[81, 1].

Planar graphene surface can interact with atoms and molecules through its

dangling p_z orbitals. Graphene oxide (GOX) is an example[28, 1] to show how the properties of graphene can be changed dramatically upon the adsorption of oxygen atoms. It is obtained through oxidative exfoliation of graphite, which can be visualized as an individual sheet of graphene decorated with epoxy (C-O-C) and hydroxyl (C-OH) groups on both sides and edges. Incidentally, GOX is also an attractive material for graphene production due to low-cost, simple and high yield reduction methods. Unfortunately, despite the oxidized graphite is a known material since last 150 years[82] and great deal of experimental and theoretical research carried out recently[83, 84, 85, 86], a thorough understanding regarding the interaction of oxygen with graphene and relevant reactions are not available yet.

To understand the experimental data, various structural configurations of GOX have been proposed based on first principles calculations. Boukhalov and his co-workers[83] suggested that 100% coverage of GOX is energetically less favorable than 75% coverage. In a later study with similar methods, Yan and his co-workers[84] suggested that it is energetically favorable for the epoxy and hydroxy groups to aggregate together to form specific types of strips with sp^2 carbon regions in between. In contrast, Wang and his co-workers[85] argued that thermodynamically stable structures are fully covered without any sp^2 carbon. Very recent study[86] combining experimental results and first principles calculations shows that multilayer GOX is metastable at room temperature undergoing modifications and reduction with a relaxation time of approximately 35 days. At the quasi-equilibrium, the nearly stable oxygen coverage (i.e. the ratio of number of oxygen N_O to the number of carbon atoms N_C) was reported as Θ=0.38 and presence of C-H species is found to favor the reduction of epoxides and to a lesser extent hydroxyl groups with the formation and release of water molecules[86]. From our point of view, there exists still controversies between theory and experiment. For example, the distribution of hydroxy and epoxy groups on GOX surface is still unclear; yet the trends related with their clustering or uniform coverage are unknown. At least, a rigorous explanation for the reason of the differences in the interpretations of experimental data is required. In particular, despite the negative formation energy of oxygen adsorption the desorption

oxygen adatoms through O_2 formation does not occur so easily is not addressed yet. Unlike GOX, the hydrogenated graphene, i.e. graphane (CH)[10, 52] and fluorinated graphene, i.e. fluorographene (CF)[11, 54] are experimentally realized and their crystal structure are well defined.

Calculations are carried out within spin-polarized and spin-unpolarized density-functional theory (DFT) using projector augmented wave (PAW) potentials[61]. The numerical calculations have been performed by using VASP package[55, 56]. The exchange correlation potential is approximated by generalized gradient approximation functional of Perdew, Burke, and Ernzerhof (PBE)[64]. A plane-wave basis set with kinetic energy cutoff of 500 eV is used. All atomic positions and lattice constants are optimized by using the conjugate gradient method, where the total energy and atomic forces are minimized. The convergence for energy is chosen as 10^{-5} eV between two steps. Oxygen-adatom and graphene system breaks inversion symmetry and a net electric-dipole moment is generated perpendicular to the graphene surface. Dipole corrections[66] are applied in order to remove spurious dipole interactions between periodic images. Gamma point i.e. $\mathbf{k}$=0 is used for rectangular supercells containing 128 carbon atoms, while 18x18x1 $\mathbf{k}$-point sampling is used for primitive unit-cell.

4.1 Interaction of Oxygen (O) with Graphene

A thorough analysis of the interaction of single O atom with graphene is essential to understand the oxidation process. Here the adsorption of single (isolated) oxygen on graphene is represented using large supercells, where O-O interaction is minimized. Owing to its hexagonal crystal structure, there are three major sites for foreign atom adsorption on graphene as shown in Fig. 4.1 (a). The hollow (H) site is above the center of hexagonal rings formed by carbon atoms. The top (T) site lies on top of the carbon atoms and the bridge (B) site is above the middle of each bonds connecting two adjacent carbon atoms. The bridge site is most favorable adsorption site for an oxygen atom and variation of the total energy along $H \rightarrow T \rightarrow B$ sites is presented in Fig. 4.1 (b). There

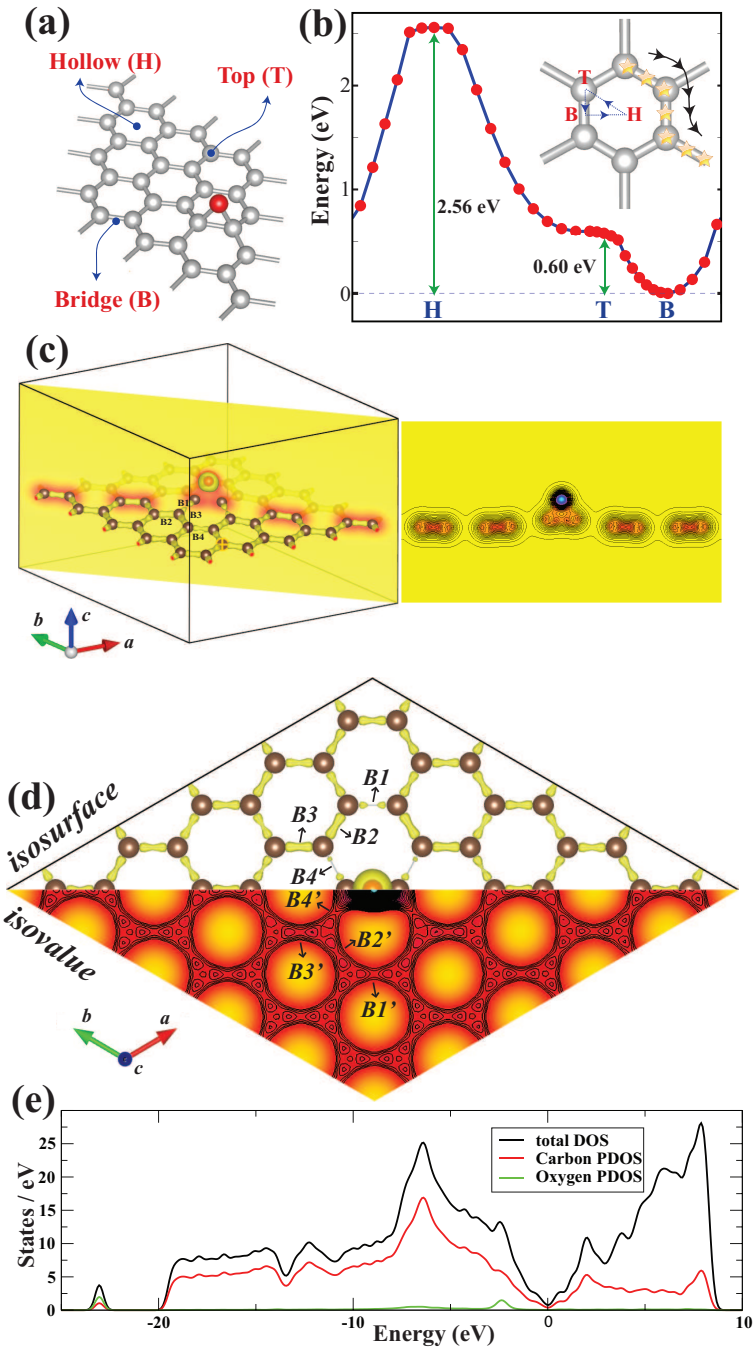

Figure 4.1: Various critical sites of adsorption on the 2D honeycomb structure of graphene and an oxygen atom adsorbed on the bridge site, which is found to be as the energetically most favorable site. Carbon and oxygen atoms are shown by gray and red balls, respectively. (b) Variation of energy of oxygen adatom adsorbed to graphene along $H \rightarrow T \rightarrow B$ directions of the hexagon. The diffusion path of a single oxygen adatom is shown by stars. (c) Charge density isosurfaces, isovalues and contour plots of oxygen adsorbed graphene in a plane passing through C-O-C atoms. (d) Same as (c) on the lateral plane of honeycomb structure. (e) Total and partial density of states projected to carbon and oxygen atoms. Calculations are carried out for supercell presented in (c) where O-O interaction is significantly small.

is an energy barrier of 0.6 eV for an O atom diffusing from bridge to top site and the energy difference between bridge and hollow site is as high as 2.56 eV. Therefore, the migration paths of oxygen adatom with minimum energy barrier follow the honeycomb structure over the C-C bonds by going from B- to T-sites as illustrated by inset in Fig. 4.1 (b). On the other hand, the energy barrier against the penetration of an oxygen adatom from one side of graphene to the other side is as high as 6 eV[88]. This high energy barrier suggests that graphene can be used an ideal coating preventing surfaces from oxidation. We note that the hollow site of graphene is more favorable for other atoms[89, 90] such as Li or Ti, while H and F atoms prefers the top site for adsorption[52, 54].

The binding energy of oxygen on graphene is defined as

$$E_b = E_T[Gr + O] - E_T[Gr] - E_T[O] \tag{4.1}$$

where $E_T[Gr+O], E_T[Gr], E_T[O]$ denote the optimized total energies of graphene with adsorbed oxygen, pristine graphene and free O atom, respectively. Our calculations show that $E_b = 2.35$ eV for the (2x2) graphene supercell containing 8 carbon and one oxygen atom, but it increases to 2.40 for (3x3) and to 2.43 for (4x4) supercells. For supercells larger than (4x4), which correspond to smaller oxygen coverage, the binding energy does not change. The calculated binding energy for full coverage Θ=0.5 (namely N_C/N_O, the ratio of the number of O adatoms N_O, to the number of carbon atoms N_C) is 2.80 (3.34) eV for one-sided (two-sided) adsorption. The binding energy of single oxygen adatom increasing from 2.43 eV to 2.80 eV at full coverage indicates a significant O-O coupling. We note that the formation energy $E_f = E_b - E_{b,O_2}/2$ (E_{b,O_2} is the binding energy of O_2 molecule) is negative for one-sided coverage indicates instability. However, this situation does not impose desorption of O through O_2 formation.

According to the Pauling scale, oxygen has an electronegativity of 3.44, which is the second largest in periodic table after fluorine (3.98) and hence the oxidation of graphene is expected to result in significant charge transfer between oxygen and carbon atoms. Our calculations using Bader analysis[91] estimates a charge transfer of 0.79 electrons from carbon atoms of graphene to oxygen. This charge is mainly transferred from the nearest two carbon atoms forming the bond above

which the oxygen adsorbed at bridge site, while some nearby oxygen atoms also contribute to the charge transfer. Figure 4.1 (c) shows isosurface and isovalue (contour) plots of total charge for a plane passing through carbon atoms and oxygen. The direction of electron density increasing from carbon atoms towards oxygen atom is a clear indication of charge transfer. In addition, two carbon atoms below oxygen are slightly distorted and raised from the plane of other carbon atoms.

In Fig. 4.1 (d) bird's-eye view of isosurface and isovalue of charge density profile of a (5x5) supercell oxygen adsorbed graphene system is presented. The structure is symmetric and the oxygen atom is at the center. We label some of the bonds corresponding to nearby bridge sites as B1,B2,B3,B4 and denote their equivalent sites by primes. While the isosurface plots of all C-C bonds of bare graphene are identical, the adsorption of single oxygen modifies the charge distribution at its close proximity. In fact, the isosurfaces plotted for 0.3 (electron/$Å^3$)[92] show that the electron population of specific bonds are higher. As clearly seen from the figure, B2 and B3 bonds contain more electrons than in B1 and B4 bonds. The reason for the electron depletion in these bonds is related with the donation of electrons from these bonds to adsorbed oxygen. Interestingly, the bonds B3, B4 and their four images contain more electron density compared to B1 and other bonds further away from the oxygen atom. For a better illustration of bond charge alternation, we also presented the isovalue plot of total charge density in the upper triangle of Fig. 4.1 (d). Again, the more isolines in the isovalue map corresponds to more charge at B2' and B3' compared to B1' and B4'. Finally we include a density of states (DOS) plot in Fig. 4.1 (e) for the system presented in Fig. 4.1 (a). The overall total DOS represents a profile similar to bare graphene DOS making a dip near the Fermi level corresponding to Dirac points and DOS projected to oxygen atom is represented by a peak around -2.5 eV. Later we show that the electronic density and band gap will change with oxygen coverage.

4.1.1 Interaction of Oxygen Molecule (O_2) with Graphene

In contrast to oxygen atom, an oxygen molecule has a weak binding with graphene. We calculated its binding energy to be 115 meV which consists of 57 meV Van der Waals interaction[63] and 58 meV chemical interaction. Its magnetic moment is 1.90 μ_B, slightly smaller than the magnetic moment of free O_2 due to weak chemical interaction. The O_2 molecule lies parallel, approximately 3 $\mathring{A}$ above the graphene plane, and do not induce any distortions to graphene honeycomb structure as in the case of single oxygen adsorption. Accordingly, the binding of O_2 to graphene is specified as physisorption.

4.2 Coverage of graphene surface with oxygen atoms

4.2.1 Coverage of oxygen on one side

Starting from single oxygen adatom, we next consider the adsorption of more oxygen atoms on graphene surface leading to higher coverage of oxygen. We exclude the hydroxyl groups in the present study to simplify the situation and hence to reveal essential aspects of oxygen adsorption. In order to reduce the effects of cell size, we construct a larger rectangular supercell containing 128 carbon atoms as shown in Fig. 4.2 (a). The isosurface charge density profile for rectangular supercell is similar to the charge density profiles in Fig. 4.1 (d) with B_{1-2} and B_{1-3} bonds having more charge compared to B_{1-1} and B_{1-4}. For the adsorption of second oxygen, we try all inequivalent bridge sites and calculate their total energies. It turns out that, the energetically most favorable site for the second oxygen adsorption is at B_{1-2} site in Fig. 4.2 (a). In addition, the calculated binding energy of second oxygen is around 2.9 eV and this is even higher than the binding energy of single oxygen on graphene. The binding energy is 154 meV lower for adsorption on B_{1-3}. The binding energy at B_{1-5} site is equal to the single oxygen binding energy. But interestingly, B_{1-1} and B_{1-4} sites are

energetically least favorable sites for second oxygen adsorption. The calculated E_b is 2.33 eV for B_{1-1} site. These binding energies and isosurface profiles given in Fig. 4.2 (a) imply a direct correlation. Apparently an oxygen atom prefers the bridge sites, where the electron density is highest compared to other available sites.

The charge density isosurface profile of graphene supercell containing two oxygen atoms is presented in Fig. 4.2 (b) and this profile can be used to predict the energetically favorable and unfavorable sites for the adsorption of third oxygen. Again, there are some bridge sites such as B_{2-1} and B_{2-2} containing more electronic charge compared to other bonds like B_{2-3} and B_{2-4}. Then the third oxygen is bound to B_{2-2} site with $E_b = 2.91$ eV which is slightly higher for the maximum binding energy of second oxygen. The binding energies at B_{2-3} and B_{2-4} are as approximately 0.57 eV smaller than the binding energy at B_{2-2} site. For the case of fourth oxygen, B_{3-1} site in Fig. 4.2 (c) having more bond charge compared to other sites is energetically most favorable. It's binding energy, $E_b = 3.16$ eV, is relatively stronger than the binding energy of previous oxygens.

The oxidation process of graphene for more than four oxygen is presented in Fig. 4.2 (e) up to twelve oxygens. The main trend is that each oxygen added to system prefers the bridge sites containing higher bond charge. Although the final structure is a domain of oxygen adatoms on graphene, it lacks the signatures of any uniform coverage which is present for the case of H and F adsorption on graphene. In the case of O, adatoms arrange themselves on graphene starting from a single adatoms. Subsequently, additional ones seek energetically most favorable sites clustering around the existing ones. This domain structure is energetically more favorable compared to any uniform coverage and this situation suggest that it is unnecessary to search for the uniform coverage of oxygen on graphene. The binding energies of the last adsorbed oxygen atom (or n^{th} adsorbed oxygen) is calculated from the expression $E_b[n] = (E_T[n-1] + E_T[O]) - E_T[n]$ in terms of the minimum total energies of $n-1$ and n oxygen atoms adsorbed on the same supercell of graphene. For any n, the lowest total energy with negative sign $E_T[n]$ and highest binding energy $E_b[n]$ is obtained by comparing the calculated total energy of n^{th} oxygen atom when adsorbed to sites remaining from the domain of

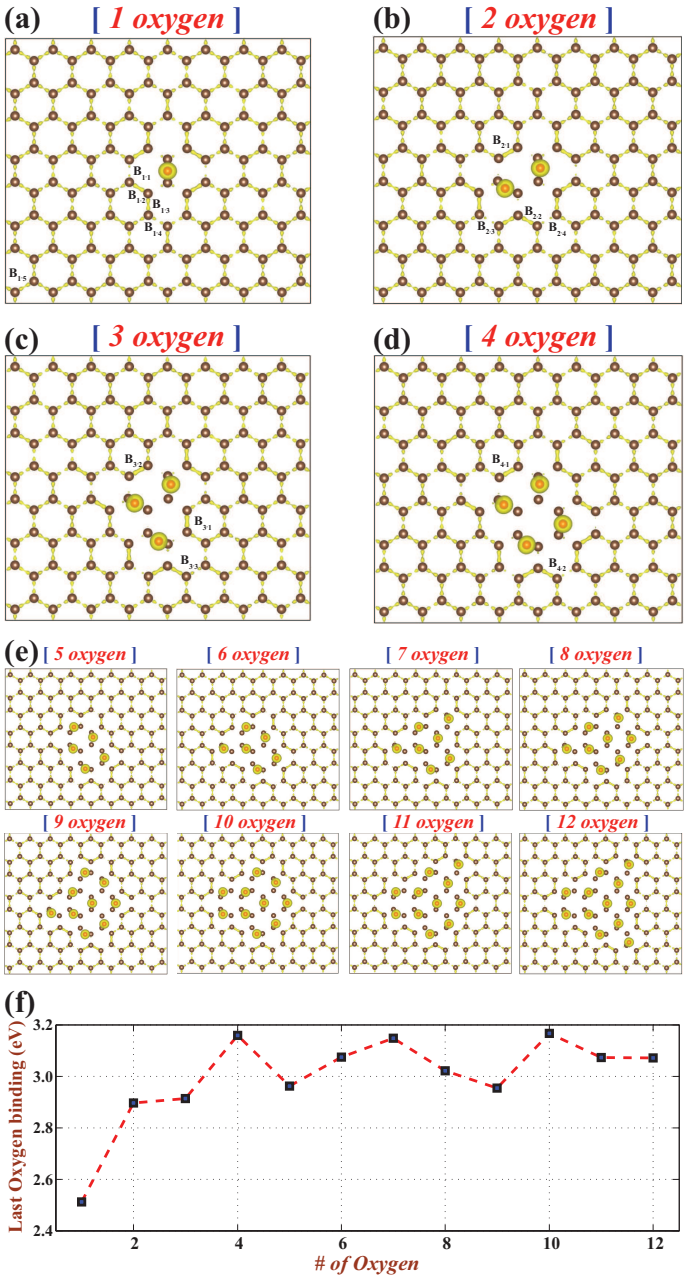

Figure 4.2: (a) Charge density isosurfaces in a rectangular supercell containing 128 carbon atoms and a single adsorbed O atom shown by a red dot. $B_{i,j}$ identifies a specific C-C bond, where i indicates the total number of oxygen atoms in the supercell and j labels some of the bond around adsorbed oxygen atom(s). (b)-(c) and (d) are same as (a), except that 2,3, and 4 oxygen atoms are adsorbed to the sites, which are most favorable energetically. For each new adatom implemented in the system the site which is energetically most favorable is determined by comparing the total energies corresponding to one of all the available sites. (e) Lowest energy configurations of 5 to 12 oxygen adsorbed on graphene. (f) Variation of the binding energy of the last oxygen adatom for the cases (a)-(e).

adsorbed $(n-1)$ oxygen atoms. In Fig. 4.2 (f), the calculated binding energy, $E_b[n]$ exhibits an oscillatory variation for $n > 2$; $E_b[n = 12]$=3.1 eV.

4.2.2 High temperature behavior

In order to test the stability of oxygen covered region in Fig. 4.2 (e), we also performed finite temperature, ab-initio molecular dynamics calculations. The Nose thermostat is used and the time steps are taken 2.5 femtoseconds. Atomic velocities are normalized at every 40 time steps and calculations lasted for 10 picoseconds at 1000 K for supercell containing 128 carbon atom and 10 oxygen adatoms. At the end, this structure remained stable and neither O_2 formation, nor dissociation of oxygen atoms from graphene surface did occurred. High binding energies of adsorbed oxygen atoms and absence of oxygen dissociation or any irreversible structural transition at 1000 K suggest that the oxygen covered domains shall remain intact for reasonable times.

4.2.3 Coverge of oxygen on both sides of graphene

The adsorption of oxygen atoms on one side of graphene and hence formation of domain structure induces structural deformations at the underlying graphene. Fig. 4.3 (a) shows the side-view of graphene structure with two oxygen atoms adsorbed on the same surface of graphene. The carbon atoms below the adsorbed oxygen atoms are distorted and raised towards oxygen atoms. The resulting buckling is as large as 0.88 $\mathring{A}$ above the plane of graphene. The amount of these distortions are further increased with the addition of more oxygen atoms. In contrast to this situation, the amount of distortion is reduced to 0.25 $\mathring{A}$, if the second oxygen atom were adsorbed to the other surface of graphene, as shown in Fig. 4.3 (b). Nonetheless, the latter configuration is 110 meV more energetic than the previous case. Hence, the two-sided adsorption shall be preferred instead of the single-sided adsorption. Despite that the favorable binding site of second oxygen atom at the other side follows our bond charge density analysis discussed in Sec. IV (B). For example, when an oxygen atom is adsorbed on one side as in Fig.

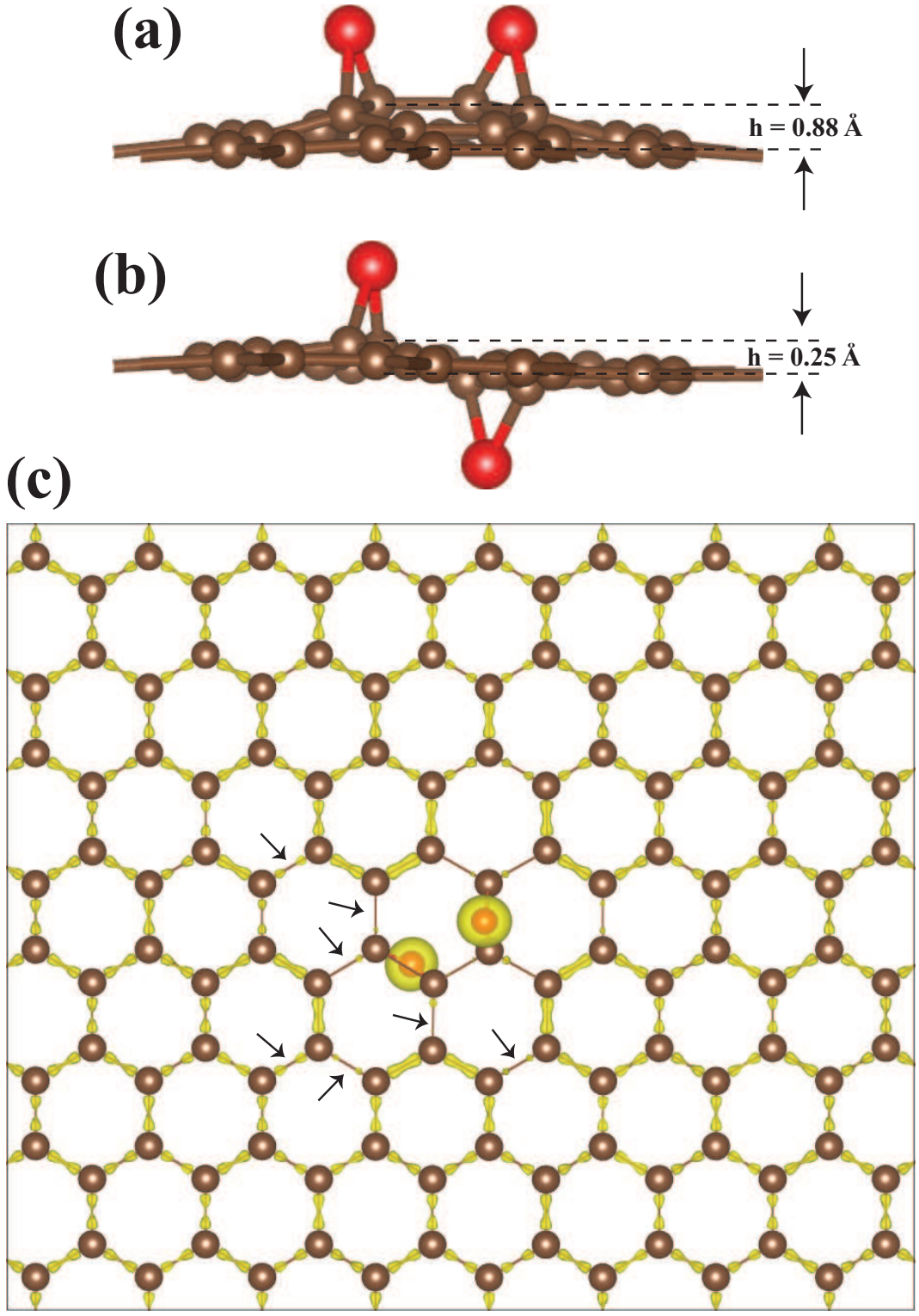

Figure 4.3: Adsorption of two oxygen atoms on one surface of graphene with buckling of 0.88 Å. (b) Adsorption of two oxygen atoms at both sides with a buckling of 0.25 Å. (c) Isosurfaces of bond charge densities after the adsorption of two oxygen atoms, each one adsorbed to different sides of graphene.

4.2 (a), the most favorable adsorption side for second oxygen is the same and is B_{1-2} site no matter the second oxygen adsorbs to the top surface (one-sided adsorption) or to the bottom surface (two-sided adsorption). Moreover, the isosurface charge density profiles shown in Fig. 4.3 (c) for the case of second oxygen adsorbed on other side are identical to the profile in Fig. 4.2 (b) when two of the oxygens are adsorbed on one side. The ordering of energetically favorable sites presented in Fig. 4.2 for higher oxygen coverage is independent of the adsorption side. Nonetheless, two sided adsorption is energetically more favorable.

4.2.4 Carbon (C) and Fluorine (F) adsorption on graphene

We now investigate the adsorption of carbon (C) and fluorine (F) atoms on graphene in the context of previous charge density analysis. Similar to oxygen atom, carbon atom is adsorbed at the bridge site. The atomic structure of carbon atom adsorbed on graphene presented in Fig. 4.4 (a) is reminiscent of the oxygen atom adsorption on graphene as presented in Fig. 4.1 (a). The distance between the adsorbed carbon atom and nearest-neighbor carbon atoms of graphene is 1.52 $\AA$, which is slightly larger than the distance of nearest carbon-oxygen atoms (1.46 $\AA$) in GOX. The angle formed between adsorbates and host graphene atoms which is 62.5 degree is almost equal for carbon and oxygen adsorption. On the other hand, the binding energy of carbon atom adsorbed on (5x5) supercell of graphene is 1.56 eV and significantly smaller than the binding of oxygen adatom on graphene. The Bader analysis calculates a charge transfer of 0.04 electrons from the adsorbed carbon atom at the bridge site to the host graphene atoms and this value is also significantly smaller and is in the reverse direction as compared charge transfer between carbon and oxygen atoms. Consequently, the chemical interaction between carbon atoms is covalent rather than ionic. Nonetheless, owing to formation of new covalent bonds between C adatom and graphene the isosurface charge density of C-C bonds presented in Fig. 4.4 (a) mimics the isosurface in the case of oxygen adsorbed on graphene as presented in Fig. 4.1 (d). The nearby bonds of B_{C1} and B_{C2} contain more

electronic charge compared to B_{C3} and other C-C bonds as shown in Fig. 4.4 (a). Moreover, it was argued that local disturbances on graphene are long ranged[93]. Interestingly, when a second carbon atom is adsorbed at the close proximity of a second carbon adatom, the bonds of the first one are broken and subsequently it is attached on top of the second adsorbed C atom to form C_2 molecule. This way ~ 5 eV energy is gained. The growth of C_n atomic chain continues whenever an adsorbed carbon atom approaches the existing C_{n-1} chain, whereby the chain is detached from graphene and attached to the top of adsorbed carbon atom. These results confirm the earlier study on the perpendicular growth of C_n chains on graphene[94]. While attractive interaction between adsorbed carbon atoms on graphene give rise to the growth of chains on graphene, the repulsive interaction between oxygen adatoms hinders the formation of O_2 molecules.

The atomic structure and isosurface charge density profile of fluorine atom adsorbed on graphene is presented in Fig. 4.4 (b). For the case of fluorine adsorption, the energetically favorable site is the top site as shown in Fig. 4.4 (b). The binding energy of single F atom adsorbed on a (4x4) graphene is calculated within LDA and was found to be 2.71 eV[54]. However, present calculations using PBE+vdW correction[63] yield a binding energy of 1.99 eV for adsorption of single F atom on a (5x5) graphene supercell. Upon fluorine adsorption, the bond charge of nearby atoms is modified as shown in isosurface profile. The Bader analysis yields a charge transfer of 0.57 electrons from carbon atoms to the adsorbed fluorine atom at the top site and this value is also significantly close to the value of charge transfer between carbon and oxygen atoms in the present study. Similar to C and O adsorption, the nearby bonds of B_{F1} and B_{F2} contain more electronic charge compared to B_{F3} and other C-C bonds. The nearest top site between B_{F1} and B_{F2} bonds and its other two analogues around F atoms contain more electronic charge and it turns out that these are energetically most favorable sites for adsorption of additional F atoms.

In Fig. 4.4 (c) we present how F atoms cover graphene. The second F atom is bonded to the top site formed by B_{F1} and B_{F2} bonds at the other side of graphene, which is most favorable site compared to to others. The third and fourth F atoms are also bound to other two analogues of this site. The energetics

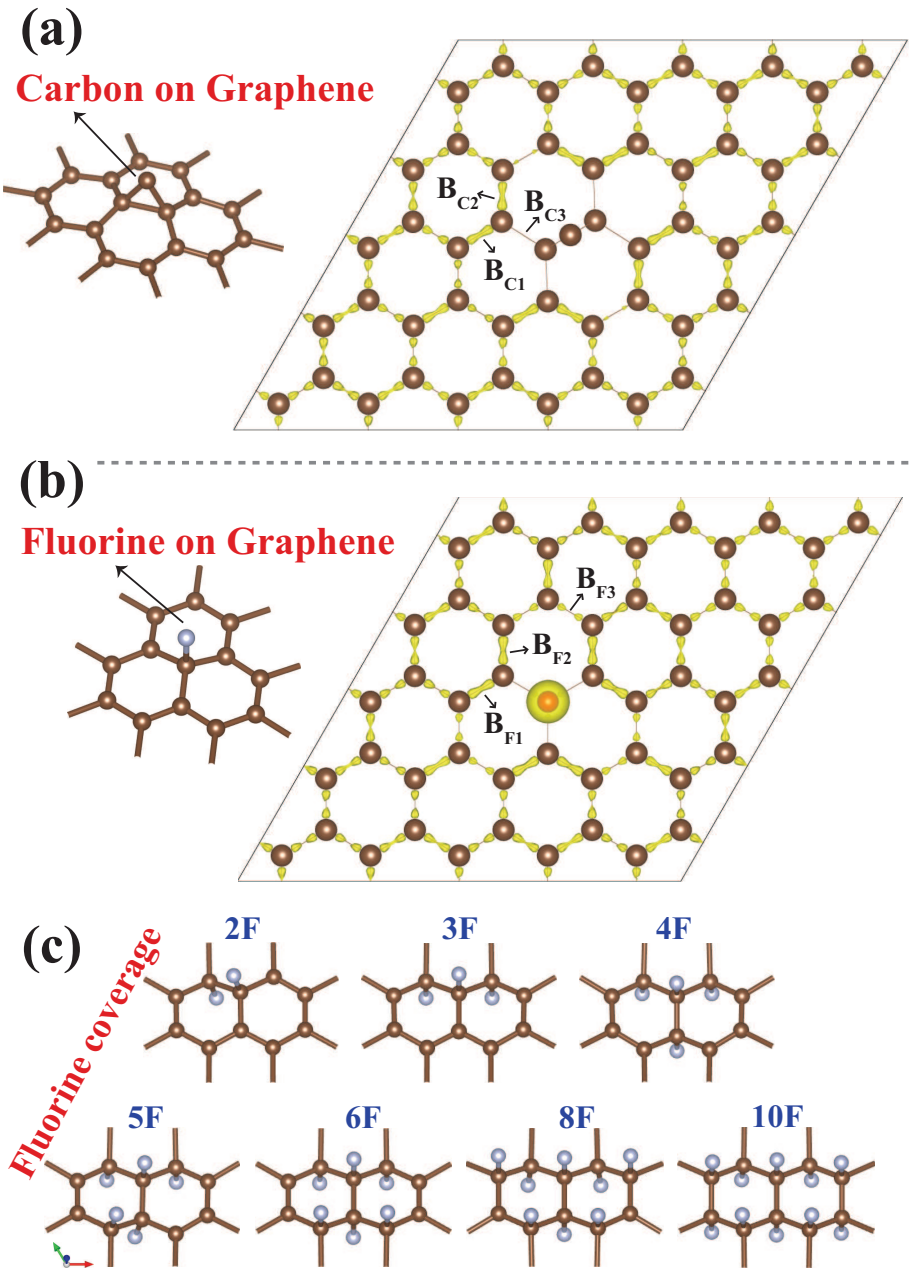

Figure 4.4: (a) The bonding configuration of a single carbon atom on graphene and the resulting redistribution of bond charges shown by isosurfaces. (b) The bonding configuration of a single fluorine adatom on graphene with energetically favorable top site. The resulting charges of C-C bonds at close proximity are shown by isosurfaces. (c) The growth pattern in the course of the fluorination of graphene.

of binding structure are in complete agreement with the amount of bond charges of nearby top sites. The final arrangement containing 10 F atoms show a well defined pattern and further fluorination will be continuation of this pattern.

4.3 Oxygen - Oxygen Interaction

The interaction between two free oxygen atoms in vacuum is attractive and the formation of an oxygen molecule is energetically more favorable. We set the total energy to zero when the distance d_{O-O} between them is 7 Å. Figure 4.5 (a) shows the variation of the energy with the distance, d_{O-O}, between two oxygen atoms. The energy does not vary until d_{O-O} is 3.5 $\mathring{A}$, but it starts to decrease as d_{O-O} decreases and passes through a minimum for d_{O-O} = 1.21 Å . This minimum corresponds to the equilibrium bond length of O_2 molecule with a binding energy of 6.67 eV. The process is exothermic and occurs without any energy barrier. However, the situation is rather different when one of the oxygen atom is adsorbed to the graphene surface and the other one is approaching from above towards it. We label some of the stages by letters, A-B-C-D-E, while the two oxygens are approaching each other as shown in Fig. 4.5 (b). The O-O coupling is initially negligible at large d_{O-O} at A, but it passes through a minimum by lowering 0.5 eV at point B corresponding to d_{O-O} = 2.63 Å. Further decrease of d_{O-O} increases the energy increases until the point C, which is $\sim$ 0.5 eV above the point B. Beyond C, oxygen atom flips sideways at D. If one prevents oxygen atom from flipping by fixing its x-y-position, but forces it towards the oxygen atom adsorbed on graphene, the adsorbed one is desorbed and two oxygen atoms form O_2 molecule at E. In this exothermic process, once the barrier is overcame, the energy decreases by $\sim$ 3.5 eV.

For the case of two oxygen adatoms, both adsorbed on graphene and approaching towards each other, the variation of interaction energy is given in Fig. 4.5 (c). Some of the positions of the approaching oxygen atom on the path of minimum energy barrier are labeled by numerals. For an oxygen starting from a bridge site at I and approaching towards the other oxygen, the energy shows an

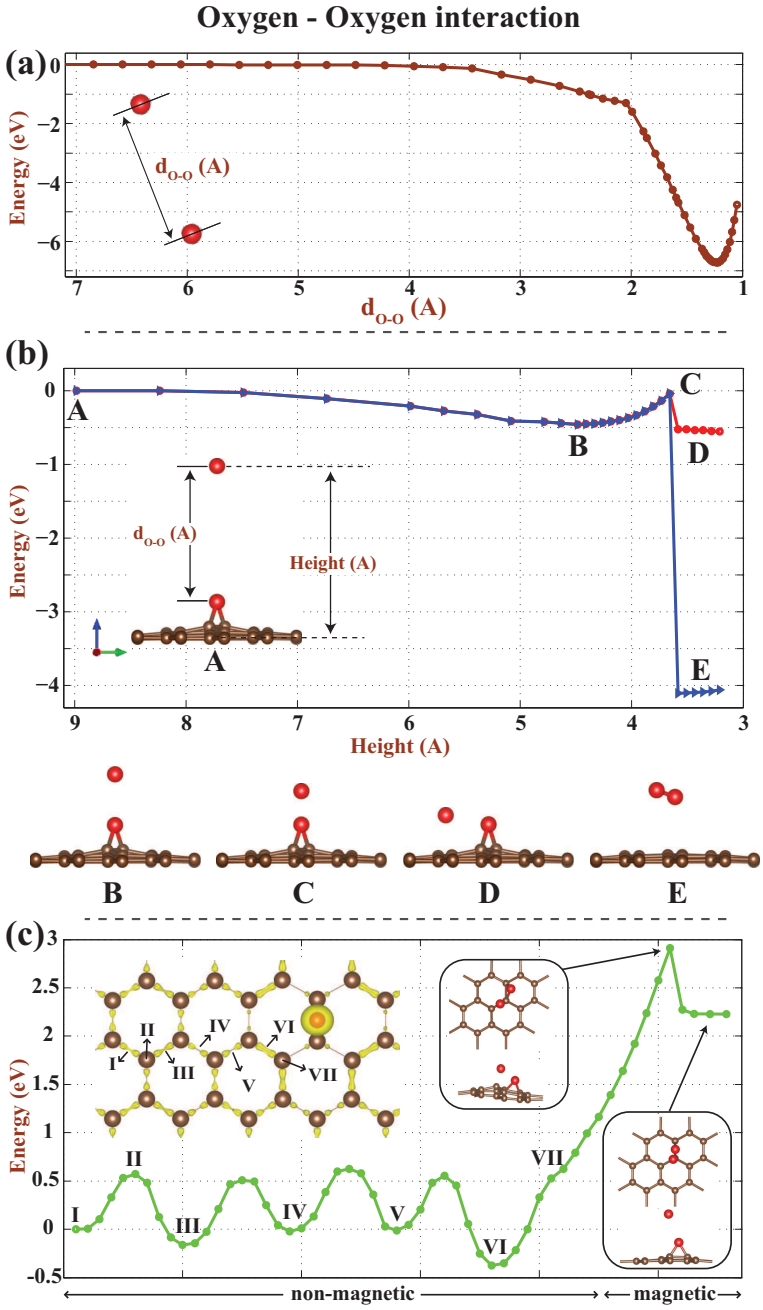

Figure 4.5: (a) The interaction energy between two free oxygen atoms approaching each other from a distance. The distance between them is d_{O-O}. (b) The interaction energy between a single oxygen atom adsorbed at the bridge site and a free oxygen atom approaching from the top. Different positions of approaching O atom are shown in the side views. (c) Variation of the energy between two oxygen adatoms on graphene. Some of the positions of the approaching oxygen atom on the path of minimum energy barrier are labeled by numerals (I-VII). Top and side views of the configuration of two oxygen atoms are shown by insets.

oscillatory behavior. The maxima, such as II, correspond to the positions where the approaching oxygen is at top site, while the minima, such as I, III, IV, V, VI correspond to positions at the bridge site. The charges of bond charge at the bridge site for reasons discussed before result in the changes in the energies at the bridge sites. For example, the bridge site VI contains more electronic charge and hence it marks the lowest energy position as one oxygen adatom is approaching the other oxygen adatom. Beyond the point VII, the non-magnetic oxygen/graphene system acquires finite magnetic moments of $\approx 0.3\ \mu_B$. Due to the repulsive interaction between two oxygen atoms adsorbed on graphene the energy increases by $\sim$3.2 eV as shown in the Fig. 4.5 (c). Eventually, the approaching oxygen atom is released from the graphene when the energy barrier is overcame. The final structure is shown by inset. These results indicate that the binding energy of each oxygen on graphene is quite strong and the formation of oxygen molecule as a result of two oxygen atom approaching each other requires significant energy barrier to overcome.

4.4 Electronic properties varying with oxygen coverage

The electronic energy structure of GOX strongly depends on oxygen coverage, as well as on the pattern of coverage. Here we consider the electronic properties corresponding to different number of oxygen atoms adsorbed at different bridge sites of the (4x4) supercell repeating periodically. Bare graphene has a semimetallic electronic structure with its characteristic density of states (DOS) making a dip at the Fermi level and linearly crossing valance and conduction bands at special K- and K'-points of Brillouin Zone as shown in Fig. 4.6 (a). It has a zero band gap and these special symmetry points are called Dirac points[95]. The energetically favorable configuration of four oxygen atoms adsorbed on a (4x4) hexagonal supercell is presented in Fig. 4.6 (b). The resulting DOS profile is different from the bare graphene, since a narrow energy gap of 70 meV is opened. The Dirac cones disappeared and the band gap occurs at the points different than

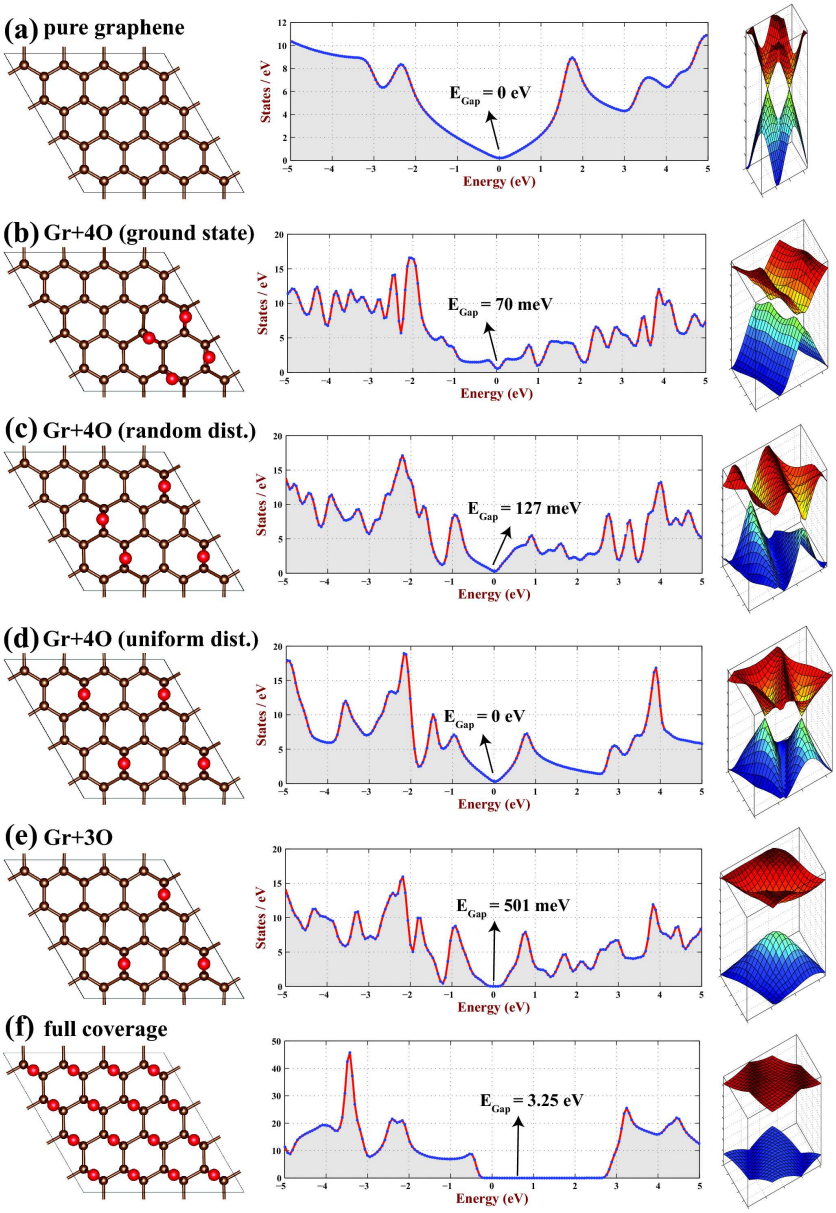

Figure 4.6: (a) Bare graphene and its typical density of states with zero state density at the Fermi level E_F. The constant energy surfaces of conduction and valence bands are shown on left-hand side. (b) A four-adatom domain corresponding to lowest total energy configuration and has a band gap of 70 meV. (c) Another adsorption configuration of four oxygen adatom resulting in a band gap of 127 meV. (d) A uniform and symmetric configuration of adsorbed oxygen atoms with zero density of states at E_F. (e) A sizable band gap is opened when the symmetry of oxygen decoration is broken by the removal of a single oxygen atom. (f) The wide band gap of 3.25 eV is opened at full coverage corresponding to $\Theta = N_O/N_C = 0.5$ (N_O and N_C are the numbers of oxygen and carbon atoms in the (4x4) supercell.

K- and K'-points. For a random and energetically less favorable distribution of oxygen atoms as in Fig. 4.6 (c), the energy band gap is further increased to 127 meV. The position of the minimum of conduction band and the maximum of the valence band has changed in BZ. Surprisingly, the semimetallic band structure of graphene is recovered when four oxygen atoms are uniformly disturbed on graphene surface as shown in Fig. 4.6 (d). Although the difference of the atomic positions from Fig. 4.6 (c) is minute, the band gap is closed and the density of states profile becomes similar to that of bare graphene making a dip at the Fermi level. The conduction and valance bands cross at K- and K'-special points similar to bare graphene.

Earlier, it was reported that the superstructures and nanomeshes having special point-group symmetry, which are generated by decoration of adatoms, adatom groups or holes repeating periodically in graphene matrix may give rise to the linearly crossing bands and hence to the recovery of massless Dirac Fermion behavior[96]. Our results in Fig. 4.6 (d) is a verification of this situation for oxygen adsorption on graphene. However, the perfect uniform coverage of oxygen on graphene is experimentally not achievable and we also present a situation where the periodicity of uniform coverage is broken by removal of an oxygen atom as in Fig. 4.6 (e). In contrast to electronic structure as in Fig. 4.6 (d), the Dirac behavior is completely removed and the resulting structure is semiconductor with relatively large energy band gap of 501 meV.

For the case of full coverage corresponding to $\Theta = 0.5$, the resulting system is a wide band gap material. Fig. 4.6 (f) shows the atomic structure and density of states profile. Unlike bare graphene and low oxygen coverage, the resulting structure has a band gap of 3.25 eV. The two sided coverage also yields similar DOS profile with a band gap wider than 3 eV. These results indicate that the regions of GOX where each carbon atom is bonded with an oxygen should be an insulator and hence should reflect light.

Chapter 5

Effects of charging on the reduction of oxidized graphene

For the neutral (uncharged) case, we studied the oxidation of graphene extensively in the previous chapter. Next we investigate the effects of charging on the oxidation properties of graphene. Our motivation comes from the experimental work by Ekiz and his co-workers[1] showing that the electrical charge has strong effects on the thermodynamics equilibrium of of graphene/graphene-oxide system. They claim that in ambient atmosphere, positive charge causes oxidation of graphene, and negative charge enhances the reduction of graphene oxide to graphene. Their results show that the electrical bias and charging effects are important in energetic analysis and design of graphene-based nanostructures. Our calculations show that the oxidation dynamics of graphene is directly related with charging and a great deal of caution should be taken when dealing with charged calculations due to deficiencies of using plane wave basis sets.

We start with a graphene 5x5 supercell containing an oxygen atom binded to it as shown in Fig. 5.1 (a). The graphene structure lies on x-y plane and the separation between graphene layers is defined by lattice constant c = 20 Å . Fig. 5.1 (b) shows the self-consistent potential energy profile planarly averaged along z direction calculated by VASP. The carbon and oxygen atoms are placed

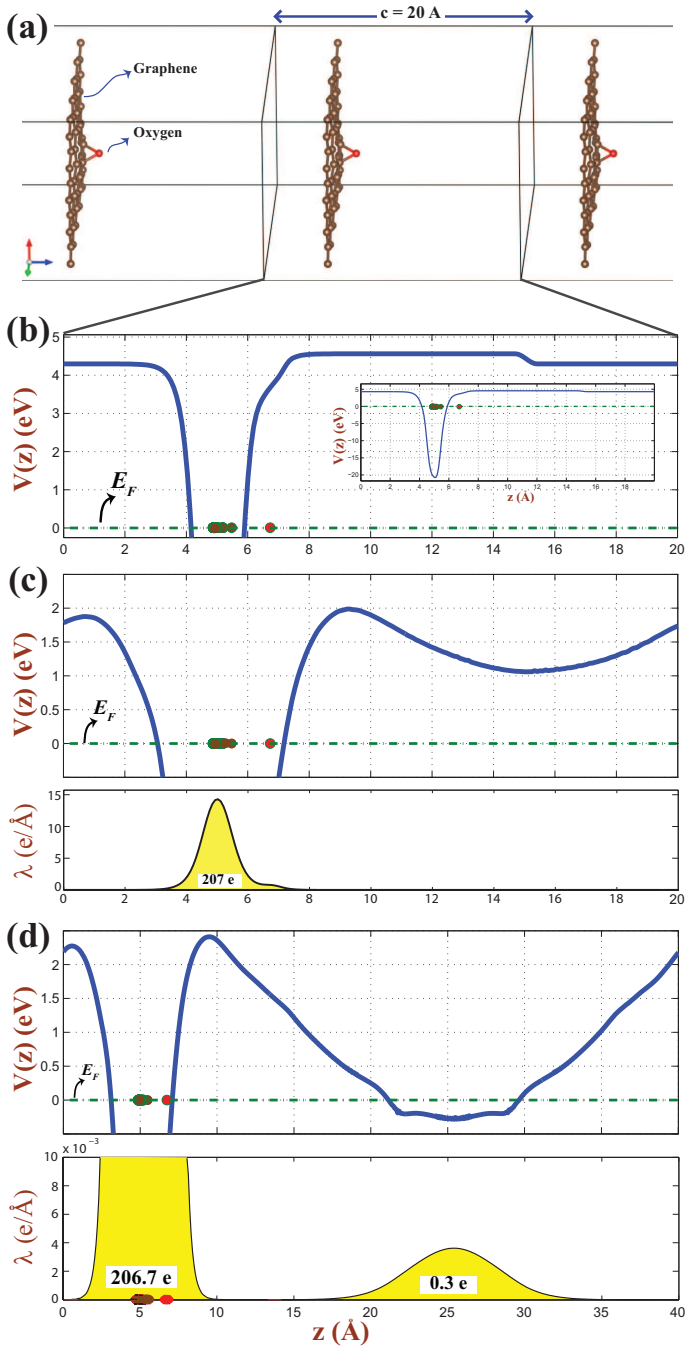

Figure 5.1: (a) Description of 5x5 graphene lattice containing an oxygen atom adsorbed on a bridge site. Periodic bondary conditions are applied. The length of supercell along z-direction is c = 20 Å . The carbon (oxygen) atoms are represented by brown (red) filled circles. (b) Planarly averaged total potential energy, V(z), profile for neutral case corresponding to structure in (a). (c) same as (b) when 1.0 electron is added to the unit cell and planarly averaged total charge density profile containing 207 electrons when integrated along z-direction. (d) same as (c) when the length of unit cell along z-direction is doubled.

around 6 Å of the unit cell and represented by filled circles as shown in the figure. Unlike pure graphene, the vacuum potential for above and below planes are different. For example, the height of potential energy at z = 1 Å is 4.30 eV and hence the work function under graphene plane not containing oxygen atom is 4.30 eV. On the other hand, the height of potential energy at z = 12 Å is 4.56 eV. Oxygen adatom and graphene system breaks inversion symmetry and a net electric-dipole moment is generated perpendicular to the graphene surface. Dipole corrections[66] are applied in order to remove spurious dipole interactions between periodic images. The drop of energy at around z = 15 Å is due to dipole corrections performed to match the potential energy tail for above and below of the system. The same profile for wider y-axis range containing the full potential energy well is also shown by inset.

In Fig. 5.1 (c), the self-consistent potential energy profile planarly averaged along z direction calculated by VASP is presented when 1 electron is added to the system. 5x5 graphene and oxygen atom contain 206 valance electron and charged system contains total number of 207 electrons. The tails of energy profile are bended but matched at around z = 15 Å as a result of additional charges as shown in the figure. The Fermi energy is below the potential energy for the regions in vacuum and all charge is confined on the layer containing graphene and oxygen atoms. The total charge density profile planarly averaged along z direction is also plotted.

By increasing the lattice constant, c, from 20 to 40 Å and keeping all other parameters unchanged, the calculated new potential energy profile is presented in Fig. 5.1 (d). Unlike the case for $c = 20$ Å in Fig. 5.1 (c), the tails of potential energy profile gets below the Fermi level for heights around $c = 25$ Å in the vacuum region. This situation is reflected by the occupation of electrons in this newly formed potential well which is absent for $c = 20$ Å . The total charge density profile planarly averaged along z-direction clearly shows the accumulation of electrons in this well. By integrating the charge density profile, it is calculated that the graphene plane contains 206.7 electrons while the rest of additional electrons (0.3 e) are accumulated in the vacuum region. This picture clearly illustrates the deficiencies of using plane wave calculations in charged calculations.

The results are highly dependent on the choice of unit cell dimensions. If one needs to use plane wave basis sets in charged calculations, the height of supercell should be arranged smaller enough prevent occupation of electrons in vacuum or atomic-orbital based methods should be used.

We next investigate the effects of charging on the diffusion barriers of oxygen on graphene. Nudged elastic band method [97] (NEB) is used for searching the diffusion barrier of oxygen atom adsorbed on a carbon bridge site to diffuse to a nearby bridge site as illustrated in Fig. 5.2 (a). Transition states were found using the VTST[97] implementation of the nudged elastic band (NEB) method with five images. According to NEB calculations the oxygen atom tries to pass over a top site and position at this site corresponds to maximum energy of the barrier as shown in Fig. 5.2 (b) for neutral system. The NEB barrier here is in accordance with our previous calculations in Sec. 4.1. The calculations are performed in a 5x5 graphene supercell and the height of unit cell is $c = 20$ Å .

The height of diffusion barrier for neutral system increases form ≈ 0.7 eV to ≈ 0.9 eV when 0.5 electron is removed from the unit cell. On the other hand, the diffusion barrier reduces to ≈ 0.4 eV upon addition of 0.5 electron to the unit cell. The addition of 1.0 electron further reduces the barrier to ≈ 0.14 as shown in Fig. 5.2 (b). These results are in good agreement with previous study by Alejandro and his co-workers[69] predicting that the decrease in diffusion barrier leads to increase of the diffusivity up to 10^9 times larger than that of the neutral cell.[69] We used the same simulation parameters as Alejandro and the height of unit cell is $c = 20$ Å in each calculation.

Alejandro and his co-workers claim that their results are robust with respect to cell size[69]. But it turns out to be wrong according to our calculations that we presented in Fig. 5.2 (c). The energy barrier gradually increases when the height, c, of the unit cell is increased from $c = 20$ Å to $c = 50$ Å . This can be interpreted as the accumulation of the electrons in the vacuum region of unit cell and reducing the effects of additional charges on the graphene plane. As we pointed out in in Fig. 5.1 (d) 0.3 electron is accumulated in vacuum region if the unit cell is charged by 1.0 electron for $c = 40$ Å .

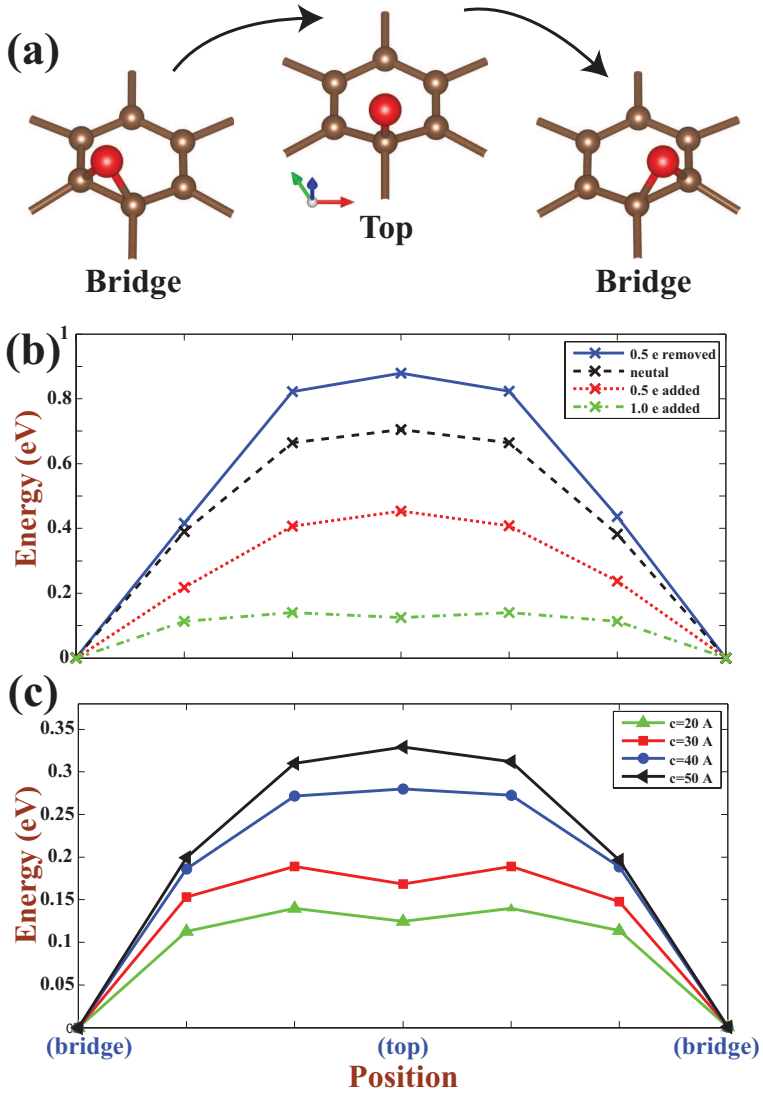

Figure 5.2: (a) Equilibrium (bridge) and transition (top) state geometries for an oxygen atom (red) is adsorbed on graphene (brown) (b) NEB energy barriers corresponding to different charging amounts. The first and last configuration corresponds to equilibrium state (bridge). The length of supercell along z-direction is 20 Å . (c) The variation of energy barrier upon increasing the unit cell length from c=20 to c=50 Å for 1.0 electron is added.

We next investigate the calculation of energy barriers of charged systems by atomic-orbital methods with SIESTA and DFTB+ in addition to VASP. Along the paths shown in Fig. 5.3 (a) the bridge site is labeled by B and top site is labeled by T in a 5x5 supercell. The neutral calculations performed by plane-wave VASP code and atomic-orbital SIESTA and DFTB+ codes yield very similar energy profiles especially along the B-T path as shown in Fig. 5.3 (b). Small discrepancies are noticed at hollow site where oxygen atom can be considered as released from the graphene.

In Fig. 5.3 (c) the energy profiles for 1 electron removed, neutral, 1 and 2 electron added calculations with DFTB+ is presented. In accordance with previous NEB calculations performed with VASP, the height of the energy barrier between B-T path is significantly reduced when 1 electron is added to the system compared to neutral case. Interestingly when two electron is added to the system the top site gets the energetically most favorable site for oxygen atom adsorption. Similar variation also occurs for calculations performed with VASP as shown in Fig. 5.3 (d) for unit cell height of $c = 20$ Å . We do not increase the amount of negative charging beyond 2 electron per unit cell since the experimentally achievable amount of charging is not so much. However, both methods of simulations performed with atomic-orbital basis set DFTB+ where the absence of free-electron like orbitals preventing the accumulation of charge at vacuum and plane-wave basis set calculations with VASP where the unit cell size is tuned carefully in order to prevent the charge accumulation at vacuum predict that the energy barrier between bridge and top site can be reduced.

We next investigate the oxygen-oxygen interaction for charged calculations as we performed for neutral case in Sec. 4.3. By bringing closer two oxygen atoms on graphene and calculating the total energy at each step, the energy profiles for positive charging (1 electron removed), neutral and negative charging (1 electron added) is obtained as in Fig. 5.4. The starting point (as labeled by A in the figure) energy is set to zero and one of the oxygen is traveled towards the other stationary oxygen along the path of bonds between carbon atoms. A, C and E points correspond to positions where moving oxygen is at bridge sites and B,D and F correspond to top sites where the energy increases. For charged and neutral

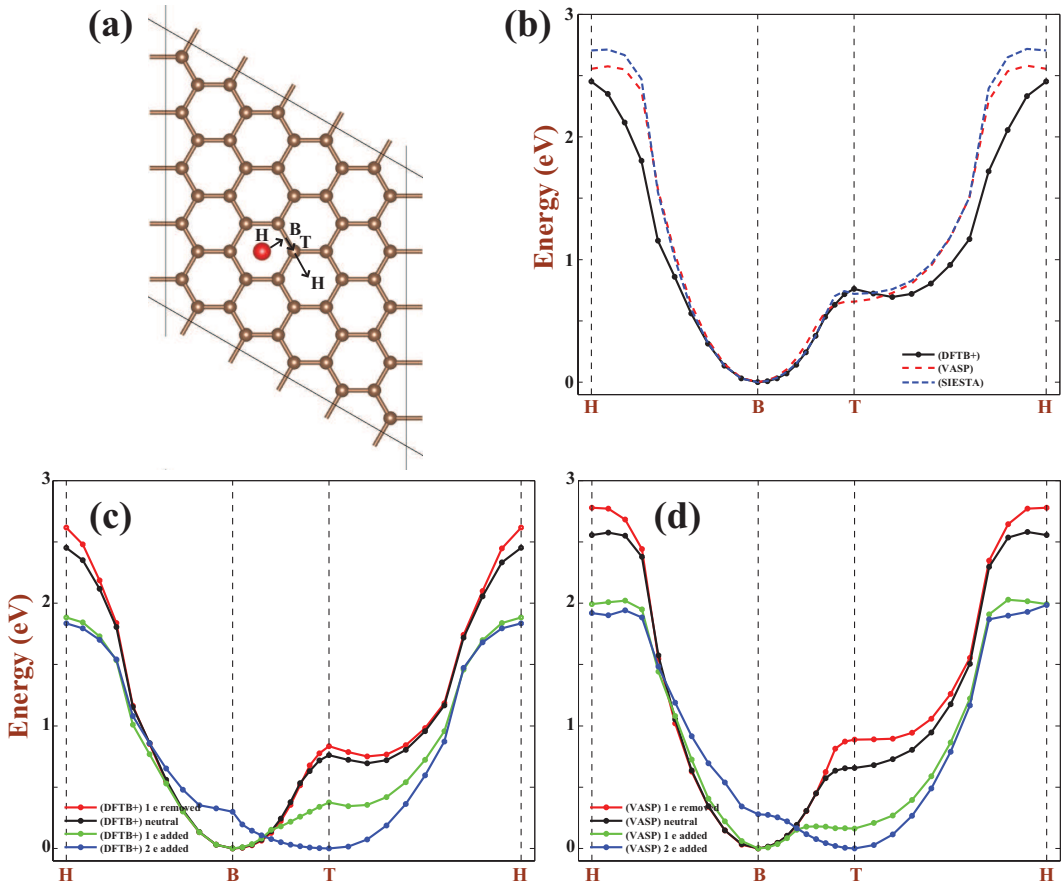

Figure 5.3: (a) The atomic structure and path of oxygen atom on graphene folloewd in an 5x5 supercell. (c) Comparision of energy profiles obtained by VASP, SIESTA and DFTB+ calculations for neutral case. The variation of energy of oxygen adatom adsorbed on graphene along H-B-T-H directions shown in part (a). (c) the variation of energy for negative and positive charging obtained by DFTB+ calculations. (d) same as (c) obtained by VASP calculations.

calculations, the point E is the minimum energy configuration. This indicates that the alternation of bond charge distributions of nearby bonds upon adsorption of an oxygen atom on graphene is not effected much for electron addition or removal. However, in accordance with our previous results in Fig. 5.3 the energy barriers of diffusion between bridge and top sites are significantly reduced upon electron addition.

The experimental evidence from Ekiz and his co-workers[1] showing the release of oxygen atoms from graphene structure upon negative charging can be hypothetically explained by approaching of two oxygen and forming an O_2 molecule. The lowering of energy barriers upon negative charging is first stage of supporting this hypothesis as clearly illustrated with the energy profiles from A to E in Fig. 5.4. But unfortunately there is a significant energy barrier, as high as 3.3 eV, and this barrier cannot be reduced with charging. The barrier energy decreases to 2.46 eV when 1 electron is added to unit cell and this is still quite too high for the formation of oxygen molecule. In addition, the final configurations do not result in O_2 molecule formation but instead the releasing of one of oxygen energy from the graphene as illustrated in G and H=I configurations or shifting of stationary oxygen to a nearest bridge site as illustrated in J.

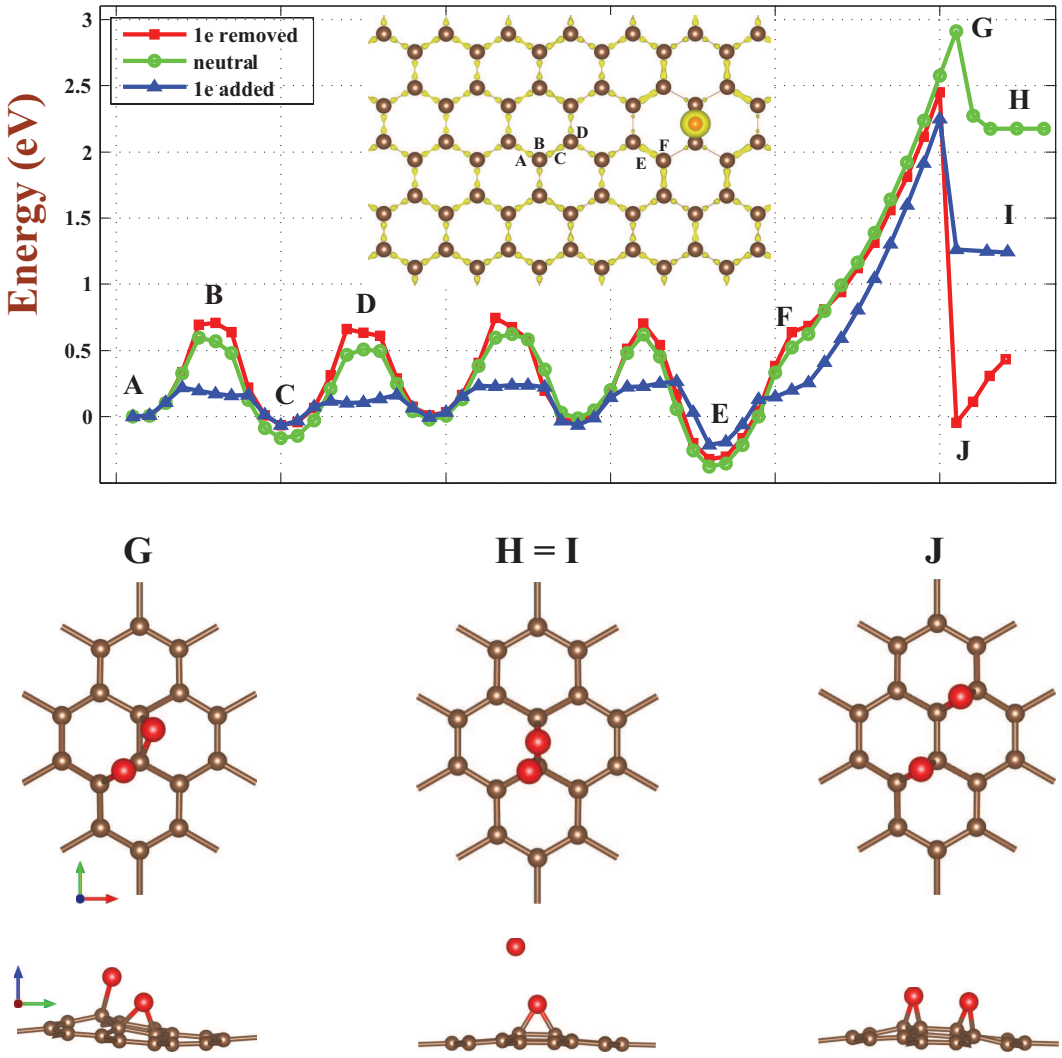

Figure 5.4: The energy profile for an oxygen moving towards another stationary oxygen on graphene for positive charging (1 electron removed, red squares), neutral (green circles) and negative charging (1 electron added, blue triangles). Some of the positions of the approaching oxygen atom are labeled by numbers (A-J). Starting point (A) energy is set to zero. The atomic configurations of G, H=I and J are given below.

Chapter 6

Conclusions

The main goal of this thesis was to investigate the effects of static charging on the electronic and structural properties of graphene and graphene-like free-standing nanostructures, such as graphane (CH), fluorographene (CF), boron nitride (BN), molybdenum disulfide (MoS_2) and oxidized graphene (GOX) with the comparison of the available experimental data and previous studies. To the best of our knowledge, we have presented the first extensive ab-initio investigation of these structures with charging.

First we have studied the charging of bare graphene and MoS_2. We have been able to understand how the size of the "vacuum" potential between layers affects the calculated properties of the negatively charged single-layer nanostructures when treated using periodic boundary conditions. We concluded that while caution has to be exercised in the studies involving negative charging using large vacuum spacing, positive charging can be treated safely using large vacuum spacing. We then investigated the effect of charging on the electronic energy band structure and atomic structure. We show that the bond lengths and hence 2D lattice constants increase as a result of electron removal from the single layer. Consequently, phonons soften and the frequencies of Raman active modes are lowered. The charging of graphene, BN and MoS_2 slabs consisting of three or more individual single layers were also studied. As a result of electron removal, three-layer, BN and MoS_2 sheets are metallized while these slabs are wide band

semiconductors, and excess positive charge is accumulated mainly at the outermost atomic layers. Consequently, excess charges are accumulated on the surfaces of slabs and induce repulsive force between outermost layers. With increasing positive charging the spacing between these layers increases, which eventually ends up with exfoliation when exceeded the weak van der Waals (vdW) attractions between layers. Electron removal from layered structures can be used for exfoliation. We also show that the binding energy and local magnetic moments of specific adatoms can be tuned by charging. Our calculations provide quantitative and qualitative insight into the effects of charging on 2D structures. In addition we have addressed the deficiencies that can occur as an artifact of using plane-wave basis sets in periodic boundary conditions and proposed advantages of using atomic-orbital based methods to overcome these deficiencies.

Next we have studied the adsorption of oxygen atoms on graphene. We pointed out that significant amount of electrons are transferred to oxygen atom from carbon atoms of graphene upon adsorption. The energetics and the patterns of oxygen coverage trends are directly related with the amount of bond charge at the bridge sites of graphene structure. The additional oxygen atoms bind to the positions having more bond charge and fully covered regions do not necessarily display a uniform and periodic patterns. On the other hand, we showed that it is essential that oxygen atoms should be arranged in arrays of periodic structures on graphene surface in order to display Dirac Fermion behavior like electronic structure with zero band gap. Disappearing of periodicity results in collapse of Dirac fermion behavior and opens a finite band gap. The bright and dark regions observed experimentally on GOX surfaces might be related to uniformity of oxygen coverage on the probed regions.

Recent experiments showed that the oxidation and reduction of graphene can take place reversibly with charging. We have investigated effects of charging on the oxidation properties of graphene. We showed that the diffusion barriers for an oxygen atom to migrate on graphene can be strongly modified with charging. While positive charging enhances the binding of oxygen atom on graphene and increases the diffusion barriers, the negative charging significantly reduces the

binding energy and diffusion barriers. These findings partially support the experimental work by Ekiz and his co-workers[1] claiming that the positive charge causes oxidation of graphene while negative charge enhances the reduction of graphene oxide to graphene. However we have not been able to fully explain this work since we didn't observe the releasing of oxygen atoms from the graphene surface upon negative charging. There might be other factors stimulating the release of oxygen such as temperature effects and some cataliytic effects. In summary, while the present results comply with the trends observed in the experimental studies under charging, we believe that there are other factors affecting the reversible oxidation-reduction processes. Using the methods and computation elucidated in this thesis, the effects of charging on periodic as well as finite systems and the related properties can now be treated with reasonable accuracy.

Bibliography

[1] O. O. Ekiz, M. Urel, H. Guner, A.K. Mizrak, and A. Dana, ACS Nano, **5** 2475 (2011).

[2] K. S. Novoselov, A. K. Geim, S. V. Morozov, D. Jiang, Y. Zhang, S. V. Dubonos, I. V. Grigorieva, and A. A. Firsov, Science **306**, 666 (2004).

[3] K. S. Novoselov, A. K. Geim, S. V. Morozov, D. Jiang, M. I. Katsnelson, I. V. Grigorieva, S. V. Dubonos, A. A. Firsov, Nature **438**, 197 (2005).

[4] Y. Zhang, Y.-W. Tan, H. L. Stormer, P. Kim, Nature **438**, 201 (2005).

[5] C. Berger, Z. Song, X. Li, X. Wu, N. Brown, C. Naud, D. Mayou, T. Li, J. Hass, A. N. Marchenkov, E. H. Conrad, P. N. First, W. A. de Heer, Science **312**, 1191 (2006).

[6] R. E. Peierls, Ann. I. H. Poincare 5, 177 (1935).

[7] M. I. Katsnelson, K. S. Novoselov, A. K. Geim, Nature Physics **2**, 620 (2006).

[8] A. K. Geim, K. S. Novoselov, Nature Materials, **6**, 183 (2007).

[9] K. S. Novoselov, D. Jiang, F. Schedin, T. Booth , V. V. Khotkevich, S. Morozov, A. K. Geim, Proc. Natl. Acad. Sci. U.S.A. **102**, 10451 (2005).

[10] D. C. Elias, R. R. Nair, T. M. G. Mohiuddin, S. V. Morozov, P. Blake, M. P. Halsall, A. C. Ferrari, D. W. Boukhvalov, M. I. Katsnelson, A. K. Geim, and K. S. Novoselov, Science **323**, 610 (2009).

[11] R. R. Nair, W. Ren, R. Jalil, I. Riaz, V. G. Kravets, L. Britnell, P. Blake, F. Schedin, A. S. Mayorov, S. Yuan, M. I. Katsnelson, H.-M. Cheng, W. Strupinski, L. G. Bulusheva, A. V. Okotrub, I. V. Grigorieva, A. N. Grigorenko, K. S. Novoselov, and A. K. Geim, Small **6**, 2877 (2010).

[12] P. Joensen, R. Frindt, S. Morrison, Mater. Res. Bull. 21, 457 (1986).

[13] M. C. Payne, M. P. Teter, D. C. Allan, T. A. Arias, and J. D. Joannopoulos, Rev. Mod. Phys. 64, 1045 (1992).

[14] L. H. Thomas, Proc. Cambridge. Philos. Soc.**23**, 542 (1927).

[15] E. Fermi, Z. Phys. **48**, 73 (1928).

[16] P. Hohenberg and W. Kohn, Phys. Rev.**136**, B864 (1964)

[17] W. Kohn and L. J. Sham, Phys. Rev.**140**, A1133 (1965).

[18] J.Perdew Intl. J. Quant. Chem **57**, 309 (1996)

[19] C. Lee, X. Wei, J. W. Kysar, J. Hone, Science **321** , 385 (2008).

[20] Y.-M. Lin, C. Dimitrakopoulos, K. A. Jenkins, D. B. Farmer, A. Grill and Ph. Avouris, Science **327**, 5966 (2010).

[21] M. D. Stoller, P. Sungjin, Z. Yanwu , A. Jinho, and R. S. Ruoff, Nano Lett **8**, 3498 (2008).

[22] M. Topsakal, H. Sevinçli, S. Ciraci, Appl. Phys. Lett. **92**, 173118 (2008).

[23] K. S. Kim, *et al.*, Nature **457**, 706 (2009).

[24] X. Li, L. Zhang, S. Lee, H. Dai, Science **319**, 1229 (2008).

[25] X. Wang, Y. Ouyang, X. Li, H. Wang, J. Guo, H. Dai, Phys. Rev. Lett. **100**, 206803 (2008).

[26] S. Tongay, M. Lemaitre, J. Fridmann, A. F. Hebard, B. P. Gila, and B. R. Appleton, Appl. Phys. Lett. 100, 073501 (2012).

[27] S. Gadipelli, I. Calizo, J. Ford, G. Cheng, A.R.H. Walker and T. Yildirim, J. Mater, Chem. **21**, 16057 (2011).

[28] D. A. Dikin, S. Stankovich, E. J. Zimney, R. D. Piner, G. H. B. Dommett, G. Evmenenko, S. T. Nguyen, and R. S. Ruoff, Nature (London) 448, 457 (2007).

[29] X. Wang, X. Li, L. Zhang, Y. Yoon, P. K. Weber, H. Wang, J. Guo, H. Dai, Science **324**, 768 (2009).

[30] T. O. Wehling, K. S. Novoselov, S. V. Morozov, E. E. Vdovin, M. I. Katsnelson, A. K. Geim, and A. I. Lichtenstein, Nano Lett. **8**, 173 (2008).

[31] H. Sevincli, M. Topsakal, E. Durgun and S. Ciraci, Phys. Rev. B, **77**, 195434 (2008).

[32] C. Ataca, E. Aktürk, S. Ciraci, and H. Ustunel, Appl. Phys. Lett. **93**, 043123 (2008).

[33] I. Gierz, C. Riedl, U. Starke, C. R. Ast, and K. Kern, Nano Lett. **8**, 4603 (2008).

[34] F. Carbone, P. Baum, P. Rudolf, and A. H. Zewail, Phys. Rev. Lett. **100**, 035501 (2008).

[35] Y. Miyamoto, H. Zhang, and D. Tomanek, Phys. Rev. Lett. **104**, 208302 (2010).

[36] R. K. Raman, Y. Murooka, C.-Y. Ruan, T. Yang, S. Berber, and D. Tomanek, Phys. Rev. Lett. **101**, 077401 (2008).

[37] D. Pacilé, J. C. Meyer, Ç. Ö. Girit, and A. Zettl, Appl. Phys. Lett. **92**, 133107 (2008).

[38] A. Nagashima, N. Tejima, Y. Gamou, T. Kawai, and C. Oshima, Phys. Rev. Lett. **75**, 3918 (1995).

[39] L. Bourgeois, Y. Bando, W. Q. Han, and T. Sato, Phys. Rev. B **61**, 7686 (2000)

[40] N. G. Chopra, R. J. Luyken, K. Cherrey, V. H. Crespi, M. L. Cohen, S. G. Louie, A. Zettl, Science **269**, 966 (1995).

[41] C. Zhi, Y. Bando, C. Tang, and D. Golberg, Appl. Phys. Lett. **87**, 063107 (2005).

[42] D. Golberg, A. Rode, Y. Bando, M. Mitome, E. Gamaly, and B. Luther-Davies, Diamond Relat. Mater. **12**, 1269 (2003).

[43] Y. J. Chen , H. Z. Zhang, Y. Chen, Nanotechnology **17**, 786 (2006).

[44] Z. Zhang and W. Guo, Phys. Rev. B **77**, 075403 (2008).

[45] Cheol-Hwan Park and Steven G. Louie, Nano Lett. **8**, 2200 (2008).

[46] V. Barone, J. E. Peralta, Nano Lett., **8**, 2210 (2008).

[47] M. Topsakal, E. Akturk and S. Ciraci, Phys. Rev. B, **79**, 115442 (2009).

[48] K. F. Mak, C. Lee, J. Hone, J. Shan, T. F. Heinz, Phys. Rev. Lett. **105**, 136805 (2010).

[49] S. Helveg, J. Lauritsen, E. Laegsgaard, I. Stensgaard, J. Norskov, B. Clausen, H. Topsoe, F. Besenbacher, Phys. Rev. Lett. **84**, 951 (2000).

[50] C. Ataca , M. Topsakal, E. Akturk and S. Ciraci, J. Phys. Chem. C **115**, 354 (2011).

[51] C. Ataca, H. Sahin, E. Akturk, and S. Ciraci, J. Phys. Chem. C **115**, 3934 (2011).

[52] J. O. Sofo, A. S. Chaudhari, and G. D. Barber, Phys. Rev. B **75**, 153401 (2007).

[53] M. Topsakal, S. Cahangirov, and S. Ciraci, App. Phys. Lett. **96**, 091912 (2010).

[54] H. Sahin, M. Topsakal, and S. Ciraci, Phys. Rev. B, **83**, 115432 (2011).

[55] G. Kresse, J. Hafner, Phys. Rev. B **47**, 558 (1993).

[56] G. Kresse, J. Furthmüller, Phys. Rev. B **54**, 11169 (1996).

[57] P. Ordejón, D. A. Drabold, M. P. Grumbach and R. M. Martin, Phys. Rev. B **48**, 14646 (1993).

[58] J. Junquera, O. Paz, D. Sánchez-Portal, and E. Artacho, Phys. Rev. B **64**, 235111, (2001).

[59] B. Aradi, B. Hourahine, and Th. Frauenheim. DFTB+, J. Phys. Chem. A, **111(26)** 5678 (2007).

[60] M. Elstner, D. Porezag, G. Jungnickel, J. Elsner, M. Haugk, T. Frauenheim, S. Suhai, and G. Seifert, Phys. Rev. B **58**, 7260 (1998).

[61] P. E. Blochl, Phys. Rev. B **50**, 17953 (1994).

[62] J.P. Perdew, J.A. Chevary, S.H. Vosko, K.A. Jackson, M.R. Pederson, D.J. Singh, and C. Fiolhais Phys. Rev. B **46**, 6671 (1992).

[63] S. Grimme, J. Comp. Chem. **27**, 1787 (2006).

[64] J. P. Perdew, K. Burke, and M. Ernzerhof, Phys. Rev. Lett. **77**, 3865 (1996).

[65] http://www.dftb.org/

[66] G. Makov and M. C. Payne, Phys. Rev. B **51**, 4014 (1995).

[67] K. T. Chan, H. Lee, and M. L. Cohen, Phys. Rev. B **83**, 035405 (2011).

[68] K. T. Chan, H. Lee, and M. L. Cohen, Phys. Rev. B **84**, 165419 (2011).

[69] A. M. Suarez, L. R. Radovic, E. Bar-Ziv, and J. O. Sofo, Phys. Rev. Lett. **106**, 146802 (2011).

[70] J. O. Sofo, A. M. Suarez, G. Usaj, P. S. Cornaglia, A. D. Hernandez-Nieves, and C. A. Balseiro, Phys. Rev. B **83**, 081411 (2011).

[71] M. leslie and N.J. Gilan, J. Phys. C **18**, 973 (1985).

[72] R Poloni, A San Miguel and M V Fernandez-Serra, J. Phys. Condens. Matter **24**, 095501 (2012).

[73] C. Attaccalite, L. Wirtz, M. Lazzeri, F. Mauri and A. Rubio, Nano Lett. **10**, 1172 (2010).

[74] A. S. Bernard, I. K. Snook, Carbon **48**, 981 (2010).

[75] Z. M. Ao, A. D. Hernandez-Nieves, F. M. Peeters and S. Lia, Phys. Chem. Chem. Phys. **14**, 1463 (2012).

[76] M. Posternak, A. Baldereschi, A.J. Freeman and E. Wimmer, Phys. Rev. Lett. **52**, 863 (1984).

[77] D.K. Efetov and P. Kim, Phys. Rev. Lett. **105**, 256805 (2010).

[78] M. Topsakal, S. Cahangirov and S. Ciraci, Appl. Phys. Lett. **96**, 091912 (2010)

[79] F. Carbone, P. Baum, P. Rudolf, and A. H. Zewail, Phys. Rev. Lett. **100**, 035501 (2008).

[80] Y. Miyamoto, H. Zhang, and D. Tomanek, Phys. Rev. Lett. **104**, 208302 (2010).

[81] Z. Wei, D. Wang, S. Kim, S.-Y. Kim, Y. Hu, M. K. Yakes, A. R. Laracuente, Z. Dai, S. R. Marder, C. Berger, W. P. King, W. A. de Heer, P. E. Sheehan, and E. Riedo, Science **328**, 1373 (2010).

[82] B. Brodie, Philos. Trans. R. Soc. London **149**, 249 (1859).

[83] D. W. Boukhvalov and M. I. Katsnelson, J. Am. Chem. Soc., **130**, 10697 (2008).

[84] J.-A. Yan, L. Xian, and M. Y. Chou, Phys. Rev. Lett. **103**, 086802 (2009).

[85] Lu Wang, Y. Y. Sun, Kyuho Lee, D. West, Z. F. Chen, J. J. Zhao, and S. B. Zhang, Phys. Rev. B **82**, 161406(R) (2010)

[86] S. Kim, S. Zhou, Y. Hu, M. Acik, Y. J. Chabal, C. Berger, W. de Heer, A. Bongiorno, E. Riedo, Nature Materials **11**, 544 (2012).

[87] H. Sahin, C. Ataca and S. Ciraci, Appl. Phys. Lett. **95**, 222510 (2009).

[88] M. Topsakal, H. Sahin, and S. Ciraci, Phys. Rev. B **85**, 155445 (2012).

[89] C. Ataca, E. Aktürk, S. Ciraci, and H. Ustunel, Appl. Phys. Lett. **93**, 043123 (2008).

[90] H. Sevincli, M. Topsakal, E. Durgun and S. Ciraci, Phys. Rev. B, **77**, 195434 (2008).

[91] G. Henkelman, A. Arnaldsson, and H. Jónsson, Comput. Mater. Sci. **36**, 254 (2006).

[92] K. Momma and F. Izumi, J. Appl. Crystallogr. **44**, 1272 (2011).

[93] C. Ataca, E. Aktürk, H. Sahin and S. Ciraci, J. Appl. Phys., **106**, 013704 (2011).

[94] C. Ataca, and S. Ciraci, Phys. Rev. B **83**, 235417 (2011).

[95] K.S. Novoselov, A.K. Geim, S.V. Morozov, D.Jiang, M.I. Katsnelson, I.V. Grigorieva, S.V. Dubonos, and A.A. Firsov, Nature (London) **438**, 197 (2005).

[96] H. Sahin and S. Ciraci, Phys. Rev. B **84**, 035452 (2011).

[97] D. Sheppard, R. Terrell, and G. Henkelman, J. Chem. Phys. **128**, 134106 (2008).